Detector Development for High Precision Measurements of $(p, 2p)$ Reactions in Inverse Kinematics using the Missing Mass Spectroscopy

Sebastian Benedikt Reichert

PhD Thesis

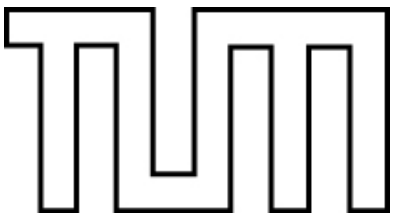

Munich 2018

TECHNISCHE UNIVERSITÄT MÜNCHEN

Fakultät für Physik

Lehrstuhl E12-Nukleare Astrophysik

Detector Development for High Precision Measurements of $(p, 2p)$ Reactions in Inverse Kinematics using the Missing Mass Spectroscopy

Sebastian Benedikt Reichert

Vollständiger Abdruck der von der Fakultät für Physik der Technischen Universität München zur Erlangung des akademischen Grades eines Doktors der Naturwissenschaften genehmigten Dissertation.

Vorsitzender: apl. Prof. Dr. Norbert Kaiser

Prüfende der Dissertation:
1. Prof. Dr. Shawn Bishop
2. Prof. Dr. Lothar Oberauer
3.

Die Dissertation wurde am 04.06.2018 bei der Technischen Universität München eingereicht und durch die promotionsführende Einrichtung Fakultät für Physik am 25.07.2018 angenommen.

Detector Development for High Precision Measurements of $(p, 2p)$ Reactions in Inverse Kinematics using the Missing Mass Spectroscopy

Detektor Entwicklung zu Hochpräzisen Messungen der $(p, 2p)$ Reaktionen in Inverser Kinematik mittels der Missing Mass Spektroskopie

Sebastian Benedikt Reichert

Zusammenfassung

Die am 17. August 2017 beobachtete Kollision zweier Neutronensterne zeigt eindeutige Hinweise auf Produktion und Ausstoß schwerer Elemente als klares Indiz für den r-Prozess in solchen Systemen. Dies erlaubt einen völlig neuen Zugang die theoretischen Vorhersagen zu testen und rückt die Forschung an exotischen, neutronen-reichen Systemen verstärkt in den Fokus. Methodische Entwicklungen für einen experimentellen Zugang zur Messung der Spaltbarriere von Kernen weitab der Stabilität, die gerade im r-Prozess eine entscheidende Rolle spielen, ist das Ziel der Kampagne NP1306-SAMURAI19. Dabei soll mit einer Missing-Mass Spektroskopie in quasi freien $(p, 2p)$ Streuprozessen die Anregungsenergien mit einer Auflösung von 1.0 MeV (stat.) und 0.5 MeV (syst.) bestimmt werden. Bei einer Strahlenergie von einigen 100 MeV/u wird der quasi-frei gestreute Anteil in den Reaktionen, d.h. 1-Step Knock-Out Reaktionen, begünstigt. Durch die besondere Kinematik ist es ausreichend, die Impulse der beiden auslaufenden Protonen zu messen um daraus auf das Anregungsspektrum des Restkerns zu schließen.

Die Herausforderung besteht in der erforderlichen Detektorauflösung. Aus diesem Grund entwickelte eine Kollaboration des Physik Departments der TUM und dem RIKEN Nishina Center in Japan einen neuen Aufbau bestehend aus einem zwei-armigen Silizium Spurdetektor und Plastik Szintillatoren. Die zwei Messgrößen zur Impulsbestimmung sind die präzisen Flugrichtungen und Energien der auslaufenden Protonen. Ersteres wird mit 100 µm dünnen hochsegmentierten Silizium Detektoren mit einem Pitch von 100 µm gemessen, zweiteres über die Flugzeit.

Zur experimentellen Demonstration der Leistungsfähigkeit des Konzepts wurde die wohlbekannte Reaktion $^{16}\mathrm{O}(p, 2p)^{15}\mathrm{N}$ in inverser Kinematik mit einer Strahlenergie von 290 MeV/u gewählt. Hier zeigte der neue Detektoraufbau seine Fähigkeit, Protonen mit Energieverlusten von nur 50 keV in den Silizium Wafern mit einem Signal-zu-Untergrund Verhältnis von 10:1 zu detektieren. Limitiert nur durch die Streuungen im Target und im Detektor wurde der Reaktionsort mit einer Genauigkeit von $\sigma^{x,z}$=195 µm genau rekonstruiert. Damit ließ sich das Anregungsspektrum von ^{15}N mit einer Auflösung von σ_{Exc}=1.2 (stat.)$\pm$ 0.3 (syst.) MeV wiedergeben. Die Kinematik der Protonen und eine Identifikation der schweren Restkerne erlauben es dabei den Untergrund durch andere Reaktionen stark zu reduzieren. Die im Rahmen dieser Arbeit gebaute Datenaufnahme für über 4000 Kanäle erlaubt höchste Auflösung und Ereignisraten von bis zu 10^5Hz und wurde bereits für ein weiteres Experiment erfolgreich übernommen.

Abstract

On August 17, 2017 the merger of two neutron stars shows clear hints on the production and emission of heavy elements as indication for the occurrence of the r-process in such systems. This allows a completely new approach to test theoretical predictions and raises the focus for the research on exotic, neutron-rich systems. Methodological developments for an experimental approach to the measurement of the fission barrier heights of nuclei far from stability is the aim of the NP1306-SAMURAI19 campaign. A missing-mass spectroscopy using quasi-free $(p, 2p)$ scattering processes is performed to determine the excitation energies with a resolution of 1.0 MeV (stat.) and 0.5 MeV (syst.). At a beam energy of some 100 MeV/u, the quasi-free scattered part of the reactions, i.e., 1-step knock-out reactions, is favored. Due to the special kinematics, it is sufficient to measure the momenta of the two emitted protons to determine the excitation energy spectrum of the residual nucleus.

The challenge is the required detector resolution. For this reason, a collaboration between the Physics Department of TUM and the RIKEN Nishina Center in Japan has developed a new setup consisting of a two-armed silicon tracker and plastic scintillators. The two measurement variables for momentum determination are the precise flight directions and energies of the protons. The first is measured with 100 µm thick highly segmented silicon detectors with a pitch of 100 µm, the second with the time-of-flight.

The well-known reaction $^{16}\mathrm{O}(p, 2p)^{15}\mathrm{N}$ in inverse kinematics with a beam energy of 290 MeV/u was chosen for a demonstrator experiment. Here, the new detector design demonstrated its ability to detect protons with energy losses of 50 keV only in the silicon wafers with a signal-to-background ratio of 10:1. Limited only by the scattering in the target and in the detectors the vertex was accurately reconstructed down to $\sigma^{x,z}$=195 µm. This allowed the excitation energy spectrum of ^{15}N to be reproduced with a resolution of σ_{Exc}=1.2 (stat.)$\pm$ 0.3 (syst.) MeV. The kinematics of the protons and the identification of the heavy residual nuclei make it possible to strongly reduce the background by other reactions. The data recording of more than 4000 channels, built within the scope of this thesis, allows highest resolutions and event rates up to 10^5 Hz and was already successfully adopted for another experiment.

Contents

Chapter 1

Physics Foundations

1.1 *R*-Process

Neutron-rich environments in the Universe form an important seed for the genesis of the heavy and heaviest nuclei. In the so-called rapid process (r-process), they grow through neutron captures and consecutive β-decay in thermal equilibrium. The path follows the right side of the nuclide chart (see figure 1.1). Its proportion on the production of elements heavier than iron is calculated to over 50 % [1].

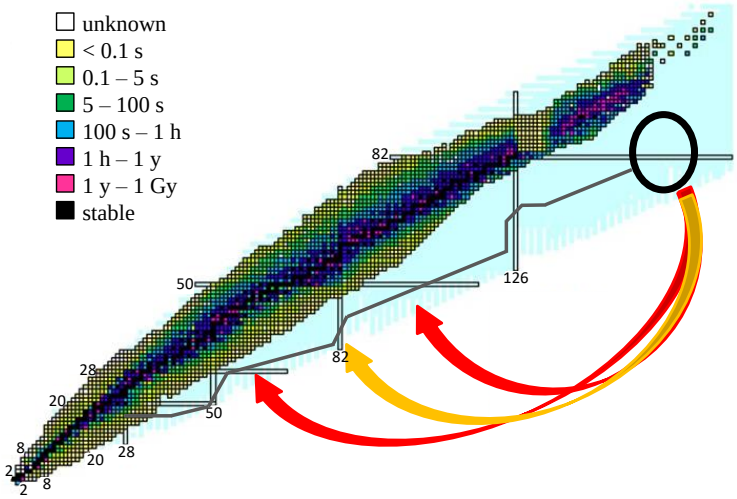

Figure 1.1: Nuclide chart with the r-process path, the (black circled) termination point of the heaviest nuclei and the subsequent symmetric or asymmetric fission, *from* [2] (Modifications from the origin figure: Enlargement of the label, drawing of the r-process path, the circle indicating the termination point and the fission fragment arrows).

Under various outer circumstances like the temperature, entropy and neutron density, the processes take place in neutrino-driven winds and magneto-hydrodynamical jets (weak and main component) of core-collapsing supernovae and in mergings of neutron stars (fission quota) [3]. The three sources are in-

corporated in figure 1.2 and show the enrichment and distribution of the created isobars, together with the observed abundances (black dots).

The weak, green-labeled r-process is one of the initial processes that redistributes the matter from light to heavy elements and is characterized by several reactions in neutrino-driven winds after core-collapsing supernovae [4]. On the surface of hot proto-neutron stars a spherical symmetric outflow of neutrinos and nuclei above the neutrinosphere lead to high entropy with sufficiently large neutron excess [5]. Because of the strong gravitational force the star falls apart and the free inner binding energy is transferred to the outer surface but also limits the explosion energy. This phase is characterized by close to stability produced isotopes with relative slow β- decays compared to the expansion of the wind environment. As soon as the nuclear statistical equilibrium has passed the temperature region above 4.5 GK, the (p, n) reaction channel dominates and surpasses the β- decay rates. Below this temperature (α, n) reactions respond the important impact to the abundances. After dropping down below 1.9 GK, the β- decay and neutron capture leads to heavier and more neutron-rich nuclei up to mass number $A \sim$125.

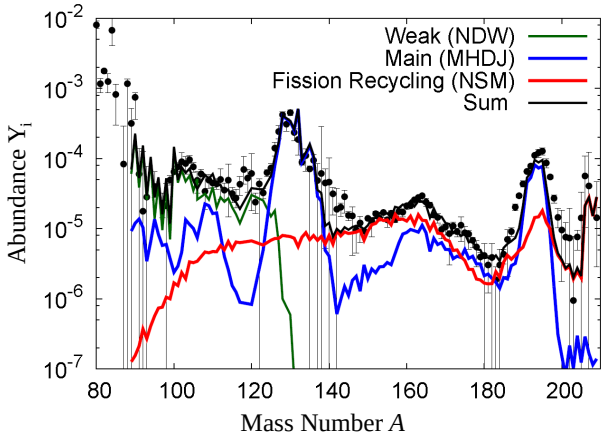

Figure 1.2: Contribution of the three sources for the r-process according to [3] (Modifications from the origin figure: Enlargement of the label). The measured abundances from $A \geq$130 onwards could be explained by the hitherto rarely studied fission recycling process.

Much stronger explosions arise in the rapidly spinning proto-neutron star by tapping the energy reservoir of the differential rotation in the form of electromagnetic energy [5]. The prominent peak structure around $A = 130$ and $A = 190$ in the main component (blue line) is a macroscopic effect where the binding energy for additional neutrons above the closed neutron shells decreases and hence an abundance for nuclei with the magic neutron numbers of N=82 and N=126 is observed. Isotopes with non-closed neutron shells left to it evolve towards the peaks by β-decay while heavier isotopes keep aggregating mass to the next magic shell nucleus. As a result, gaps occur next to the closed neutron shell region.

Parts of the isobars in the regions between the peaks and especially the very heavy atoms stem supposing from the fission recycling process (compare the red line). It needs extremely high neutrons to seed ratios which could be reached in neutron star mergers. In such an environment, the collection of neutrons in nuclei is extremely fast and the propagation path on the nuclei chart goes far to the right. Here the formation goes up to the heaviest nuclei until the fission barrier height drops below the neutron separation energy [6] which defines the termination of the element synthesis.

Broad dispersion of the fission fragments together with the very fast neutron capture processes overlay the shell effects and hinder corresponding structures. When this process ends abruptly, the present isotope distribution freezes out and therefore, fission products of these nuclei give a rather flat distribution.

The relevance of the results leads back to the figure 1.1. Depending on the height of the fission barriers, thus the termination point of the heaviest nuclei, and the nature of the fission, the fission quota causes completely different mass distributions and abundances of nuclei in the Universe. The two red arrows indicate the area for asymmetrically fissioning nuclei and the yellow arrow indicates the cycle formed by symmetrical fission.

1.2 History of Fission

Fission is one of the oldest experimentally observed reactions and was first detected by Hahn and Straßmann [7]. Meitner and Frisch gave a first theoretical explanation assuming a potential stemming from the liquid drop model [8]. Based on the concept of Bohr [9], the statistical model describes the evolution of a circular shape with radius R_0 in terms of an expansion in Legendre polynomials P_n,

$$\mathrm{R}(\theta)=(\mathrm{R}_0/\lambda)\ [\ 1 + \textstyle\sum_{n=1} \alpha_n P_n(cos\theta)]. \tag{1.1}$$

Following the history of theoretical models, compiled by [6] (see figure 1.3), the next important step was the adding of a correction energy $(M_{exp} - M_{LD})$ by Swiatecki [10] (left bottom diagram). He used the available experimental observed ground-state masses to vary the theoretical calculated masses from the liquid drop model which led to improved spontaneous-fission half-lives.

Much progress was made in the last decades to answer the key questions on the optimum trajectories in the fission process, the shapes and energies along them, finally the maximum energy at the saddle point, i.e., the barrier height and the local symmetries of the nuclei.

More detailed studies by Strutinsky [11][12] and later Möller and Nix [13] revealed a two (or sometimes even three) humped fission barrier by introducing a microscopic ansatz from the single-particle model where the protons and neutrons

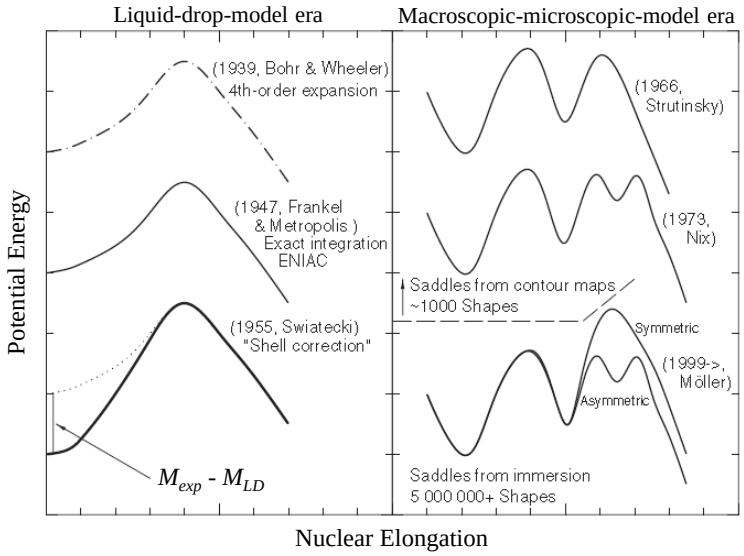

Figure 1.3: Development of the models to describe the potential energy in terms of nuclear elongation, *from* [6] (Modifications from the origin figure: Enlargement of the label). From an initial rather qualitative description, accurate predictions were made based on millions of shapes.

oscillate with the deformation caused by variations of the single particle level density in the vicinity of the Fermi energy [14]. The added shell-effects modify the potential energy with respect to the nuclear elongation. The right column in figure 1.3 shows the high impact when the maximum potential energy in the liquid drop model coincides with a minimum in the shell model [9]. Depending on the odd or even number of protons and neutrons, the nucleus passes through one or two minima for larger deformations.

In this potential, fission can take place by tunneling through the barrier from the first or second minimum where the nuclei are already deformed (also called as isomeric fission). If the energies are above the fission barrier, the probability of prompt fission, decay back into the first minimum or trapping in the region of the second minimum is 0.9, 0.1 and 10^{-4} [14]. The multiple fission barriers make it difficult to define exactly one value[1]. Another reason is that the process itself is also likely to take place below its actual barrier height. For example, in the case of the direct (d, p) reaction at ^{239}Pu the channel opens between the excitation energies $E_{Exc} = 4\,\mathrm{MeV}$ and $6\,\mathrm{MeV}$, increases and then reaches a constant value (see figure 1.4).

The decay channels with one emitted proton and the fission channel are plotted separately. Until the end of the measurement series at E_{Exc}=8 MeV the fission channel does not occur exclusively but is in competition with other processes. An excitation of the nucleus occurs, for example, via the emission of neutrons

[1] we will come back to this issue later in the definition of the fission barrier heights in figure 1.6

instead of which binding energies at B_n=6.4 MeV (see the marker in the x-axis of figure 1.4) approximately coincide with the attainment of the maximum level for fission. A very similar behavior of the fission probability P_f and its increase within

$$\Delta E_{Exc} = 2\,\mathrm{MeV} \tag{1.2}$$

is also found in the adjacent long-lived nuclei of U, Np, Pu, Am [15].

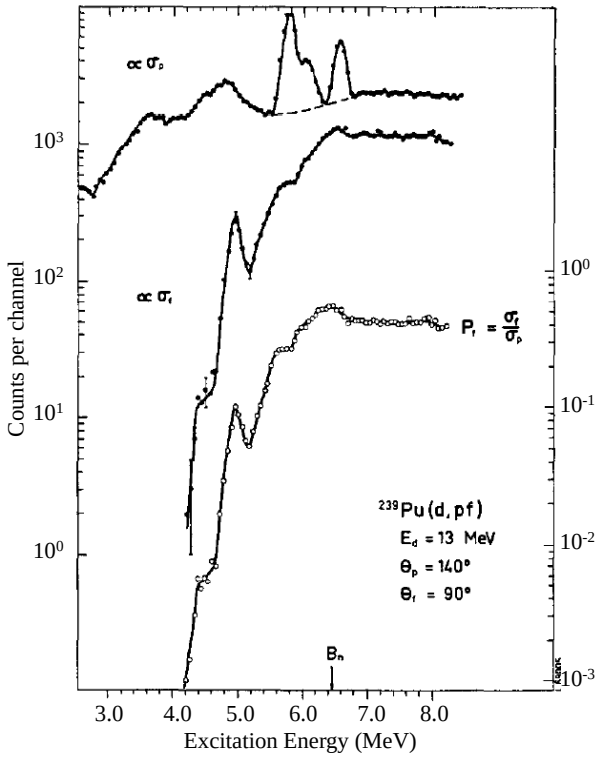

Figure 1.4: Shape of the exit channels (single proton spectrum $\propto \sigma_p$ and fission $\propto \sigma_f$) in dependence on the excitation energy in the example of the $^{239}\mathrm{Pu}(d,pf)$ reaction. The peaks in the σ_p spectrum correspond to carbon and oxygen. For the fission probability spectrum P_f (y-scale on the right) they are subtracted and path in the dashed line is used. B_n marks the neutron binding energy. *From* [15] (Modifications from the origin figure: Enlargement of the label).

Three models peel out to give the most accurate parametrizations in different regions during the fission process [6]. The Nillson perturbed-spheroid (ϵ) parametrization [16] considers the potential energy in a three dimensional deformation space with the attitude to elongate in order to define the neck strength under the premise of axial symmetry. This model has its limit beyond the fission isomeric state. The multipole (β) expansion prolongs the radius vector in axially symmetric spherical harmonics Y_l,

$$r(\theta,\phi) = R_0\left(1 + \sum_{l=1}^{\infty} \beta_l Y_l\right) \tag{1.3}$$

under the constrain of volume conservation such as the fission-barrier curve follows a certain distance between the two nascent fission fragments and the quadrupole deformation β_2. In contrary to the last model, here larger deformations are allowed but still no fission occurs.

The last transfer from the fission-isomeric minimum to the scission describes the Swiatecki-Nix three quadratic surface (3QS) parametrization. It includes the nascent-fragment deformations as two independent shape degrees of freedom. Since all three models are independent, this kind of study is an excellent way to cross-check the results in the overlapping regions.

One spectacular example of the composition is the reconstruction of the potential route of ^{180}Hg (see figure 1.5) which was formerly expected to split into two ^{90}Zn nuclei with closed neutron shells at N=50 and semi-magic proton number Z=40. Due to the experimental results by Andreyev et al. ([17] and the discussion there) with an asymmetric fission fragment mass distribution behavior we focus on that isotope to explain the path.

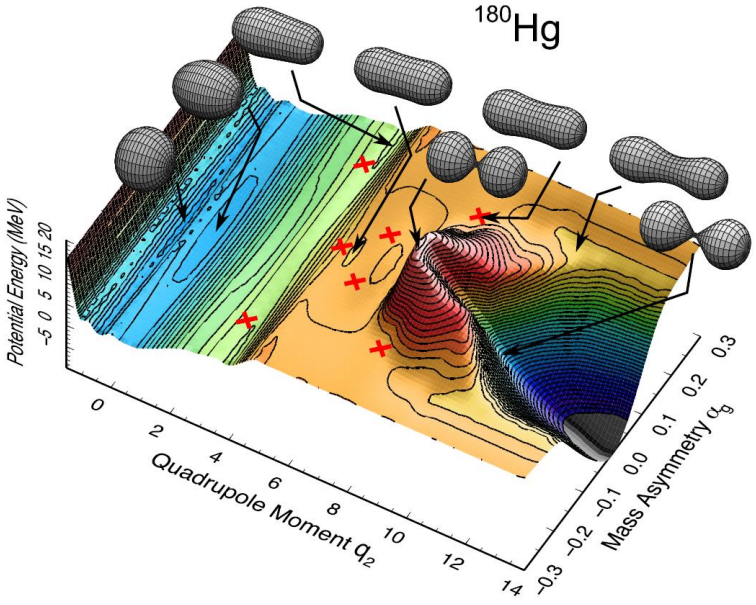

Figure 1.5: Calculated deformation of ^{180}Hg depending on the three parameters quadrupole moment q_2, mass asymmetry α_g and the potential energy, *from* [18]. The symmetrical decay is blocked by a high ridge that drops into a deep valley when the nucleus is already fragmented.

The degree of symmetry is introduced by using a method based on the Brownian shape-motion on the potential-energy surfaces. With growing elongation (here expressed as correlated quadrupole moment q_2) the path along the symmetry axis (two mass-equal fragments) is blocked by a high ridge. The route clings on it and follows a more asymmetric division. Before the nucleus falls into the valley of symmetric decay at the end of the ridge, ^{180}Hg is already such deformed that scission takes place.

Two conclusive figures shall close this section. Figure 1.6 a) presents the calculated (first) fission barrier heights of the nuclei of interest, i.e., it restricts to the highest potential difference between the ground state and scission [6]. The nuclei inside the black outline have complete closed neutron shells (vertical bar) or Z magic number (horizontal bar). The plot reveals a dependence of the fission height on the structure of the neutron shells. The closer one approaches the magic number from both sides, the fission barrier increases at constant proton number. This dependence cannot be confirmed for the magic number of the protons [19]. However, along the y-axis the fission barrier tends to sink.

The trend of increasing (until the turning point at $N = 126$) and decreasing fission barrier height is exemplary shown for Pb (see figure 1.6 b)). The average slope corresponds to a change of the necessary excitation of

$$\Delta E_{Exc}^{isotop} \sim 0.8\,\mathrm{MeV} \tag{1.4}$$

per added neutron.

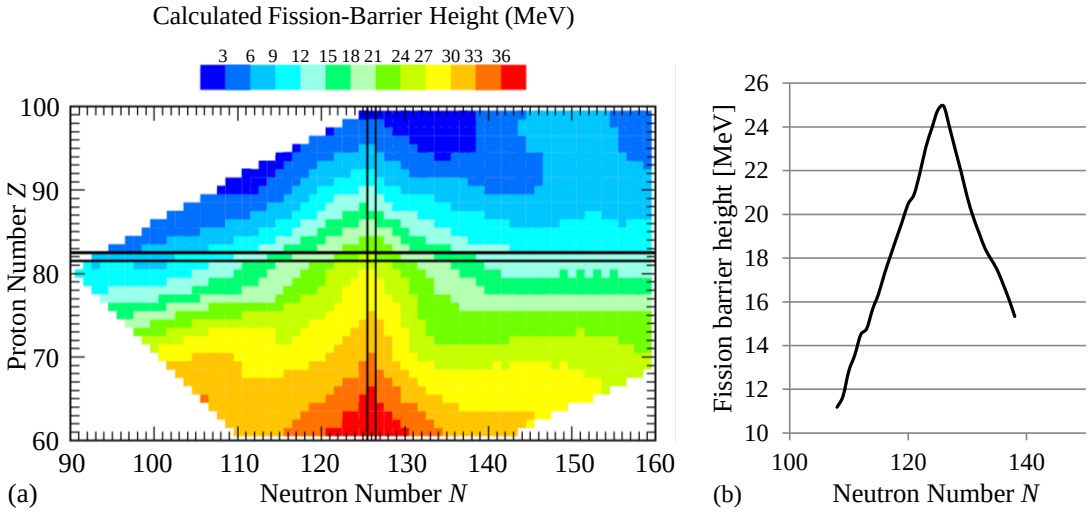

Figure 1.6: (a) Calculated fission barrier height in our region of interest, *from* [20] (Modifications from the origin figure: Enlargement of the label). For small Z, higher fission barriers height tends to be observed. In neutron dependence, the closed shell at N=126 determines the behavior and is exemplary shown for the element Pb in (b) (*Data taken from* [20]).

The associated fission fragment distribution (see figure 1.7) is divided into a blue sea with two red islands on the sides. The areas marked in blue predict a symmetrical break of the nuclei. As the red concentration increases, the division into asymmetric nuclei is indicated. The shell structure seems less important and microscopic effects determine the path [18]. The present experimental results are marked with a white cross. Some have quite poor statistics and a direct comparison is sometimes difficult. However, where the statistics is high and the

error bars are small, the theoretical fission fragment distributions are close to the measured ones [20].

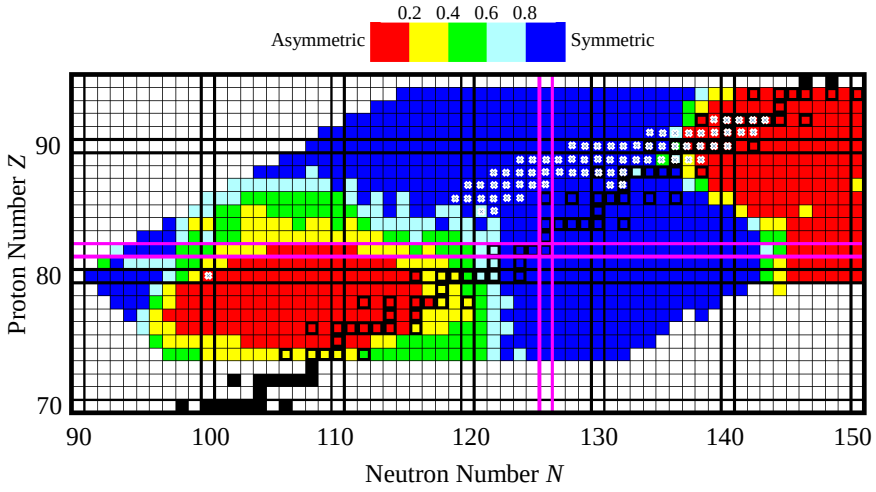

Figure 1.7: Calculated distribution of fission fragments, *from* [20], (Modifications from the origin figure: Enlargement of the label, Drawing of the present experimental analyzed nuclei (white crosses)). The color marks the regions of symmetric (blue) to asymmetric (red) fission. Especially at the junctions and on neutron-rich side there are few measured data so far.

The two plots are interdependent: As we have shown in the example of ^{180}Hg in figure 1.5, the path towards fission depends largely on the deformation at which the nucleus breaks. If the core had a higher fission barrier, i.e., if it had been possible to expand further, it could have reached the symmetrical valley and had broken apart there. On the other hand, the asymmetric degree of break-up can be used to determine the existing deformation and thus conclusions are drawn about the fission barrier height.

1.3 Realization: Quasi Free Scattering

From the last section we realized the importance of experimental results to gauge the values for the theoretical models. This experiment must be designed that the intended parameters are preferably available without unknown side effects or theoretical assumptions.

We have demonstrated by the example ^{240}Pu that the height of the fission barrier is not a fixed value but that the fission is a statistical process caused by tunneling effects (see figure 1.4). With the double-humped barriers, it will be even harder to designate the one point of fission. Therefore, in order to be able to make a description of the path of the cross section, the measurement accuracy must be smaller than the energy window of $\Delta E_{Exc} = 2\,\mathrm{MeV}$ (compare equation (1.2)).

Furthermore, the absolute values of the fission barrier height (defined, e.g., by [6] and plotted in figure 1.6) along the isotopes of heavy elements give insight to the nuclear forces of the fission process. In order to be able to separate the necessary fission barrier heights between neighboring isotopes systematic uncertainties of the setup must not exceed the value in equation (1.4).

Hence, physically relevant data points can be provided if the experimental resolution is below

$$\sigma(E_{Exc}) < 1.0\,(\text{stat.}) \pm 0.5\,(\text{syst.})\,\text{MeV} \tag{1.5}$$

with the classifications between resolution (stat.) and systematic uncertainty (syst.).

Missing mass spectroscopy may be an appropriate tool to determine the excitation energy spectrum. The two emitted protons in the quasi-elastic $(p, 2p)$ knock-out reaction contain the full kinematic information on the nuclear excitation of the heavy residue. The exclusive kinematic attitudes of this scattering process makes it unique compared to any other reactions. Since very exotic beam nuclei are to be investigated in the future only inverse kinematics is possible nowadays. Accelerated nuclei impinge a hydrogen target where one proton of the beam nucleus is quasi-free-scattered (QFS) off the projectile and both collision partners disperse. In later experiments, the fission barrier heights can be found by measuring the final state of the residual nucleus (split or not) in addition by a set of detectors downstream.

The theoretical background of the suitable missing mass spectroscopy in the context of QFS reactions will be expatiated in the following. It is a well-known tool to extract spectroscopic information of the proton-hole states [21]. In particular, we show the relevance of this scattering process in terms of determining the excitation energy (see section 1.3.1), the momentum distribution (see section 1.3.2) and the cross sections (see section 1.3.3).

1.3.1 Excitation Energy

After hadrons are knocked out of a core nucleus, the remaining nucleons are redistributed in order to achieve the lowest energy state (ground state). The leftover energy is emitted in the form of particles and photons. Depending on the type of reactions and the beam energy it is possible to look deep into the nuclear structure by generating different excitation modes, especially collective ones, and measure the inner part of the projectile wave function [22]. Knock-out reactions with proton targets as scattering partners are ideally suited for this.

In the overall aspect the $(p, 2p)$ scattering is a deep-inelastic collision between the target proton and the beam nucleus where the projectile excites. In a more microscopic view the reaction corresponds to an elastic scattering between two

protons, providing high sensitivity to the intrinsic nucleon momentum distribution [23][24].

In a non-relativistic frame the laboratory opening angle after collisions of two equal-mass particles is always θ_{op}=90Â° and the momentum vector lays in a plane, i.e., $\phi = 180$Â°. The total momentum distributes along the two protons 1 and 2, $\vec{p}_1$ respectively $\vec{p}_2$, and is proportional to their polar angles $\theta_{1(2)}$,

$$|\vec{p}_{1(2)}| \propto \frac{1}{cos\theta_{1(2)} + \frac{sin\theta_{1(2)}}{cos\theta_{2(1)}}}. \tag{1.6}$$

This statement stays true if the scattering process becomes relativistic and the Lorentz-boost shrinks the opening angle and thus the measurement of the angles contain all information to deduce the momenta.

However, the bound proton finds itself in a potential S_N consisting of the sum of the separation energies caused by the neighboring particles in the initial nucleus A and the excited state E^* in which the proton is located. So it is no longer a two-body problem but we deal with a three-body system containing two accelerated protons 1 and 2 and the excited heavy particle A-1. Figure 1.8 shows the connections: In the sudden approximation the two protons collide directly with each other and the rest of the nucleus remains in spectator status [25]. If the energy transfer exceeds the separation energy, the bound proton detaches. Since it was involved in the internal impulse distribution, the reaction can only be regarded as quasi-free. In a second step, a further interaction with the recoil nucleus A-1 can take place during the exit action which in the best case, though, changes the kinematics only slightly (eikonal ansatz).

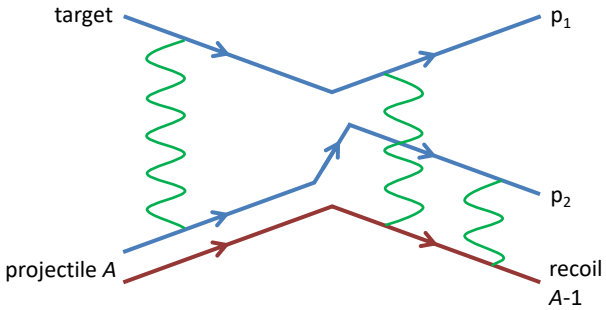

Figure 1.8: Schematic drawing of the QFS $(p, 2p)$ reaction. The hydrogen target interacts with the beam and both collision partners release one proton.

From the conservation of energy follows the new relation between the binding energy $B_N = S_N + E^*$ and the observables T [26]:

$$B_N = S_N + E^* = T_1 - (T_1' + T_2' + T_{A-1}') \tag{1.7}$$

with T as the kinetic energies before the reaction and T' afterwards. Since the four-momentum is conserved, there is a direct insight into the localization of the released proton in terms of its separation energy S_N and the excitation

energy E^*. This binding energy B_N leads to a reduced rest mass of the proton, the sharp momentum-angle correlation in (1.6) smears out and the conserved quantity breaks.

Mathematically the reduced mass of the proton in the nucleus can be transferred into an equivalent of the Lorentz invariant mass Q of the recoil nucleus, derived from the four-momentum conservation equation by

$$\begin{pmatrix} E_A \\ 0 \\ 0 \\ p_{Az}c \end{pmatrix} + \begin{pmatrix} m_{p1}c^2 \\ 0 \\ 0 \\ 0 \end{pmatrix} = \begin{pmatrix} E_{p1} \\ p_{p1x}c \\ p_{p1y}c \\ p_{p1z}c \end{pmatrix} + \begin{pmatrix} E_{p2} \\ p_{p2x}c \\ p_{p2y}c \\ p_{p2z}c \end{pmatrix} + \begin{pmatrix} E_{A-1} \\ p_{A-1x}c \\ p_{A-1y}c \\ p_{A-1z}c \end{pmatrix} \tag{1.8}$$

assuming that the beam projectile A is directed in z-direction and the target proton p_1 is at rest. The Lorentz formalism expresses the masses of the particles by their energies E and the absolute values of the momenta $|\vec{p}|$,

$$mc^2 = \sqrt{E^2 - |\vec{p}c|^2}. \tag{1.9}$$

Here the invariant mass Q is included in the total energy E_{A-1} and the momentum vector $\vec{p}_{A-1}$. Using the four-momentum conservation in (1.8) and the last defined equation (1.9), we finally deduce an expression for the total energy of the residue

$$Q = \sqrt{(E_A + m_p c^2 - (E_{p1} + E_{p2}))^2 - ((p_{p1x}c + p_{p2x}c)^2 + (p_{p1y}c + p_{p2y}c)^2} \\ \overline{+(\sqrt{E_A^2 - m_A^2 c^4} - (p_{p1z}c + p_{p2z}c))^2}. \tag{1.10}$$

Q is composed of the rest mass m_{A-1} and an excitation energy E^* (i.e., the missing mass) and we can write

$$E^* = Q - m_{A-1}c^2 \tag{1.11}$$

where E^* is to be equated with the energy in equation (1.7), since although the total binding energy is distributed among the two protons but in the repulsion the momentum transfer to the residual nucleus reflects the internal momentum of the radiated proton.

Taking into account normal distributed Fermi momentum of $\sigma_{Fermi}^{p1/2}$=95 MeV/c for the bound ground state $p_{1/2}$ [27][2] and the initial nucleus ^{16}O at beam energy of E_{beam}=290 MeV/u, the spectra in figure 1.9 illustrate the kinematic characteristics of the $(p, 2p)$ reaction in the laboratory frame, calculated from the event generator of L. Chulkow and V. Panin [26].

[2]Theoretical calculations were carried out for the ^{16}O$(p, 2p)^{15}$N experiment at E_{beam}=451 MeV/u in [28].

The polar angles $\theta_{1/2}$ are related to each other and lie on a diagonal with a fading symmetric shower to smaller angles (see figure 1.9 a)). Due to the forward Lorentz-Boost the distribution of the two protons does not spread evenly over the polar angle but it passes through an arc-shaped form with a maximum at $\theta_{1/2}$=41Â° and start and end points at $\theta_{1/2}$=0Â° and $\theta_{1/2}$=77Â° (see figure 1.9 b)). The opening angle has a Landau-like shape with the peak position at θ_{op}=82.5Â° in the case of the direct transition into the ground state at E_{beam}=290 MeV/u (see c)). It drops precipitous after the maximum value and the tail to small values ends at θ_{op}=0Â°. The azimuth angles between the two protons form isotropic distributed planes which are normal distributed around ψ=180Â° with a width of σ_{ψ}=20Â°. The width comes from the continuous distribution of the Fermi momentum between the two protons and the residue.

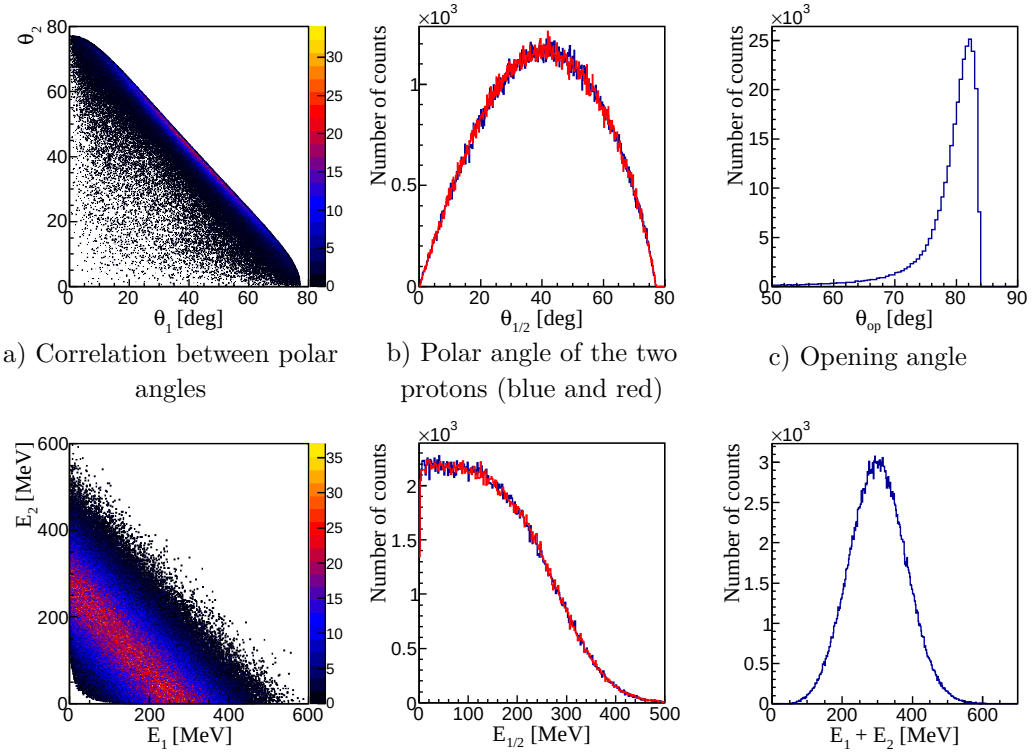

a) Correlation between polar angles

b) Polar angle of the two protons (blue and red)

c) Opening angle

d) Correlation between kinetic energies

e) Kinetic energies of the two protons (blue and red)

f) Added kinetic energies

Figure 1.9: Characteristic angle and energy distributions of the two protons from QFS $^{16}\mathrm{O}(p,2p)^{15}\mathrm{N}^{g.s.}$ reactions. The blue spectra in b) and e) correspond to proton 1 and the red one to the second proton.

Depending on the beam energy the peak positions of the opening angle of higher excitation energies decrease with different slopes (see figure 1.10). Higher beam energies can hold the shape of the opening angle almost constant over a few dozens MeV (compare the highest expected fission barrier heights of ∼30 MeV in figure 1.6 b)). The difference between the peaks of the ground state and, e.g., of the first excited state of $^{15}\mathrm{N}^{*}$ at E_{exc}=6.3 MeV is θ_{op} = 1.2Â° at E_{beam}=290 MeV/u.

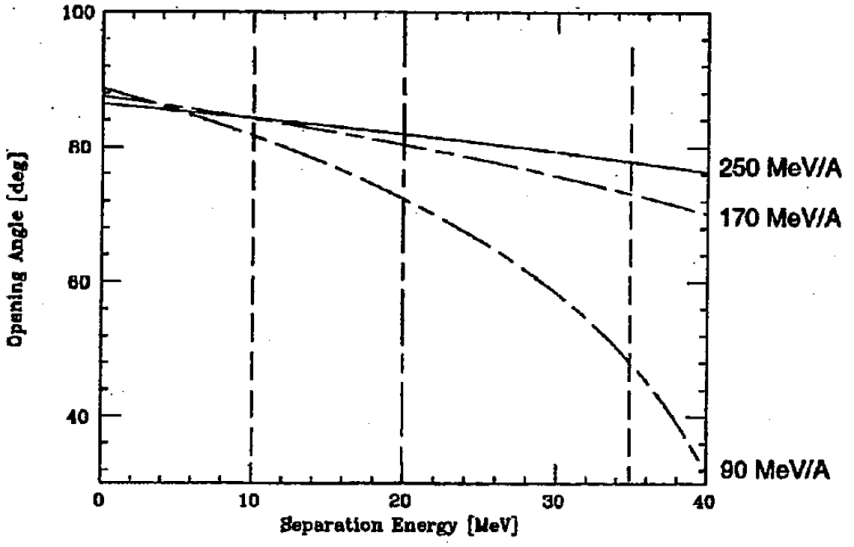

Figure 1.10: Dependence of the opening angle on the beam energy at increasing separation energies; *from* [29]. Here, we can equate the separation energy with the excitation energy.

While in the case of a totally elastic collision between free protons, the input energy is distributed evenly to the two impact partners, the additional Fermi impulse of the struck proton smears the sharp energy correlation whose events are evenly distributed along the diagonal (see figure 1.9 d)). Figure 1.9 e) shows the distribution of the individual proton energies which is constant for energies of less than $E_{1/2}$=100 MeV and then decreases until $E_{1/2}$=500 MeV. In the most right figure 1.9 f) the two kinetic energies added together yields in a Gaussian-like shape with the peak at the beam energy of 290 MeV and the width of σ_{E1+E2}=80 MeV.

This quick derivation shows the elegance of the missing mass spectroscopy. With the measurement of the momenta, i.e., the energy and flight direction of the incoming nucleus A and of the two emitting protons, we can determine the excitation spectrum of the outgoing heavy particle A-1. That means, this method is independent on measurements of all momenta and γ-energies which is required, e.g., in the competitive invariant mass spectroscopy.

1.3.2 Momentum Distribution

One of the major asset of QFS $(p, 2p)$ reactions is its powerful capability to probe the single particle properties. In the missing mass spectroscopy we take advantage of the reflection of the internal momentum $\vec{p}_3$ onto the initial momentum $\vec{p}_1$ of the incident proton and the momenta p'_1 and p'_2 of the two emitted protons by

$$\vec{p}_{A-1} = \vec{p}_1 - (\vec{p'}_1 + \vec{p'}_2) = -\vec{p}_3. \tag{1.12}$$

Due to the momentum conservation the angular momentum is in opposite direction to the recoil momentum $\vec{p}_{A-1}$ of the residue and in previous experiments in inverse kinematics that recoil momentum was measured [28][26].

From the shape of the orbital angular momenta $\vec{p}_3$ the associated sub-shells l of the struck protons can be derived. The momentum widths depend mainly on the two competitive effects of the magnitude of the centrifugal barrier (broader momentum distribution for larger l) and the separation energies S_N of the states (increased momentum width for larger S_N) [30][31]. Using the Fourier transform the wave function of the formerly bound nucleon is determinable [21][31].

The interplay between the different potentials were calculated for the missing momenta in the first two s- and p-sub-shells of ^{11}B based on the eikonal theory using the fragmentation reaction $^{12}\mathrm{C}(p,2p)^{11}\mathrm{B}$ at E_{beam}=500 MeV/u in reference [32] (see figure 1.11). There the momentum $\vec{p}_3$ was divided into the longitudinal, $\vec{p}_z$, and the transverse part, $\vec{p}_t$,

$$\vec{p}_3 = \vec{p}_z + \vec{p}_t. \tag{1.13}$$

While the higher separation energy S_N of the protons in the s-orbit and the larger angular momentum of the p-wave function result in the same shapes of the longitudinal momentum distributions (see figure 1.11 a)) the influence of the scattering matrices enters into the transverse and total momenta such that the different shells separate more clearly (see figures 1.11 b) and c)) [32].

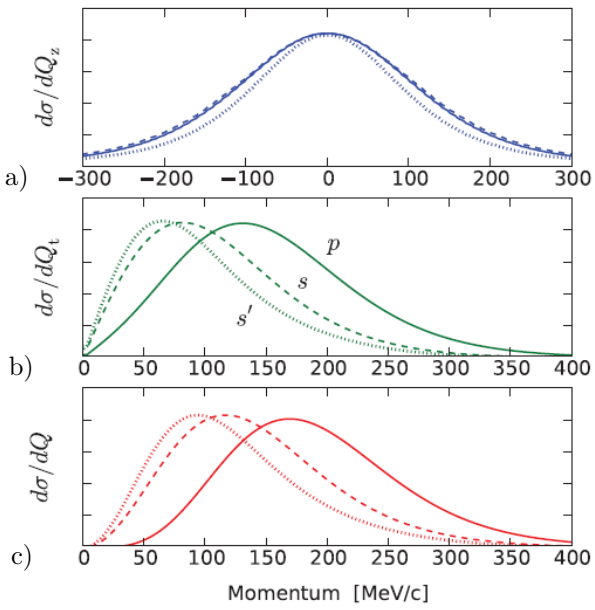

Figure 1.11: Longitudinal (see a)), transverse (see b)) and total momentum distribution (see c)) for the missing momentum in the reaction $^{12}\mathrm{C}(p,2p)^{11}\mathrm{B}$ in inverse kinematics at E_{beam}=500 MeV/u; *from* [32]. The solid line represents the Fermi momentum in the p-shell and the dashed line shows the momentum in the s-orbit. The dotted line simulates the shape of the s-orbit with the assumption of the same separation energy as for the p-shell.

1.3.3 Cross Section

The absolute value of the cross section is meaningful as input for large-scale calculations of the shell model [33]. Deviations between the theoretical and experimental cross sections were observed with changing proton and neutron number due to additional forces like the tensor force [34] up to a point where the classical shell model breaks down and exotic modes of excitations define the nuclear structure. Short-range and long-range correlations mix the configurations of different states at the Fermi surface or couple to collective resonances [33]. Coming back to the begin of this chapter, the measured cross sections are a necessary input parameter to simulate the nuclear structure and the underlying forces which might help to predict the path of the *r*-process near the driplines [35] and the fissuring mechanisms at the termination point.

The following discussion is focused on the energy range selected later in the work. To classify the total cross section a distinction is made between the three components stripping, diffractive breakup and Coulomb dissociation,

$$\sigma_{tot} = \sigma_{str} + \sigma_{dif} + \sigma_C. \tag{1.14}$$

The first term corresponds to an inelastic breakup in which interactions take place between the proton and the residual nucleus, resulting in an excitation where also protons can be emitted from the nucleus additionally. The second component is used to determine the proportion of elastic impacts, i.e., the two-body interaction without further direct collisions. A minor role here plays the cross-section σ_C for Coulomb interactions (which could also lead to an excitation and consecutive particle emission) [36].

In the subsequent steps, the fundamentals of the calculation are provided in order to maximize the cross-sectional area σ_{dif} while simultaneously minimizing the total cross-section σ_{tot}. In the QFS formalism the differential cross section is described by the square of the transition amplitude T, i.e.,

$$\frac{d^3\sigma}{dE'_{p1}d\Omega'_{p1}d\Omega_{p2}} \propto \sum_{\gamma} |T_{p,p1p2}(\gamma)|^2 \tag{1.15}$$

where γ is the summation over the spin components in the initial and final states [32].

$T_{p,p1p2}$ is defined as the product of the spectroscopic factor *S(lj)* for the bound nucleon with quantum numbers *lj* with the transition τ from the initial states of the proton $\chi^{(+)}_{\vec{k}_{p1}}$ and the bound state wave function ψ_{jlm} to the final states $\chi^{(-)}_{\vec{k}'_{p1}}$ and $\chi^{(-)}_{\vec{k}'_{p2}}$ without respect to the recoil nucleus. Formally, it is written by [32][37]

$$T_{p,p1p2} = \sqrt{S(lj)} \left\langle \chi^{(-)}_{\vec{p}'_{p1}} \chi^{(-)}_{\vec{p}'_{p2}} | \tau_{p1p2} | \chi^{(+)}_{\vec{p}_{p1}} \psi_{jlm} \right\rangle. \tag{1.16}$$

This expression is valid for protons with kinetic energies in the range of 75 MeV and below. In the case of non-perturbed, elastic scattering, the wave functions

of the protons are that for plane waves and we can make use of the plane wave impulse approximation (PWIA) ansatz, i.e., neglecting scattering wave distortion, in combination with the independent particle model. One obtains

$$T_{p,p1p2} = \sqrt{S(lj)}\tau(\vec{p}'_{p1p2}, \vec{p}_{p1p2}; E) \int d^3\vec{r} e^{-i\vec{\tilde{Q}}\cdot\vec{r}} \psi_{jlm}(\vec{r}) \tag{1.17}$$

where $\vec{\tilde{Q}}$ is the missing momentum in center of mass motion

$$\vec{\tilde{Q}} = \vec{p}'_{p1} + \vec{p}'_{p2} - \frac{A-1}{A}\vec{p}_{p1}. \tag{1.18}$$

Inserting formula (1.17) into the cross section in equation (1.15) let us interpret the strength of the cross section proportional to the momentum distribution of the nucleons inside the beam-nucleus.

For any non-elastic reactions by (weak) initial- and final-state interactions, this approximation is too simplistic and the distortion of the remained residue A-1 nucleus must be included [38]. The equivalence between the total and the elastic cross section breaks. An appropriate way is the distorted wave impulse approximation (DWIA) in the eikonal approach of the Glauber theory [38] where an additional factor is introduced, the scattering matrix $S(b, \theta)$. It contains the scatterings inside the nucleus. Taking it into account in the transition amplitude we obtain

$$T_{p,p1p2} = \sqrt{S(lj)}\tau(\vec{p}'_{p1p2}, \vec{p}_{p1p2}; E) \int d^3 e^{-i\vec{\tilde{Q}}\cdot\vec{r}} S(b, \theta)\psi_{jlm}(\vec{r}). \tag{1.19}$$

In contrast to the previous case, now the total cross section is multiplied with the probability to find a nucleon at the position $\vec{r}$ to be scattered. The form of the elastic and total nucleon-nucleon cross sections for the p-p and p-n reaction channels in the case of ^{12}C is presented in figure 1.12. The dashed lines correspond to the most likely single-step direct processes where the transparency of the nucleon-nucleon system reaches its maximum. In physical terms, the de-Broglie wavelength is small and the mean-free path of a nucleon in the nuclear medium is equal to its size. This means that the core emitting proton is with high probability quasi-free scattered.

For the $(p, 2p)$ case, the total cross section (black line) is minimal at low beam-energy and arises significantly from $\sim 500\,\mathrm{MeV/u}$ on, since the fraction of low-energetic released protons with high binary collision probabilities in the residue decreases [32]. Since the blue dashed marked elastic cross section mainly depends on the (beam-energy independent) momentum distribution inside the nucleus, it is constant over a large region up to $E_{beam} = 1\,\mathrm{GeV/u}$ and decreases then slightly. However, the elastic part covers almost the total amount of the cross section in the low-beam-energy region[3]. From an experimental point of view, no arbitrarily

[3]The curiosity of a larger elastic cross section than the total cross section is due to medium corrections which weight the elastic part more in that energy range, for details see [32].

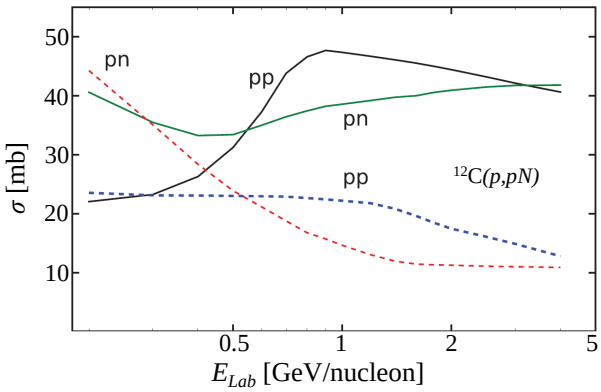

Figure 1.12: The solid curves show the free p-p and p-n total cross sections in comparison to the angle-averaged elastic p-p and p-n cross sections, drawn in dashed curves for the ^{12}C fragmentation, *from* [32] (Modifications from the origin figure: Enlargement of the label). At an energy up to 300 MeV/u the p-p total cross section consists mainly of its elastic scattered contribution.

small beam energy can be selected. If the energy of the released protons drops below 100 MeV, the proportion of nucleon-nucleon reactions increases significantly and the core becomes opaque for elastic scattering. We can therefore conclude that beam energies in the range of 200 - 300 MeV/u are suitable for elastic QFS reactions.

Chapter 2

Experimental Apparatus

This experiment is part of a bigger project to determine the fission barrier heights of heavy neutron-rich isotopes at the RIKEN Nishina Center[1] based on the new methodology of extracting the excitation energy in quasi-free $(p, 2p)$ reactions. Measuring the momentum vectors of both emitted protons with high resolution, the missing mass in a quasi-free scattering kinematic is defined. In this thesis we developed an experimental setup which determines the observables with the necessary precision (see section 2.1 for the requirements on the resolutions and section 2.2 for the overall design).

In addition such an experiment performed in inverse kinematics provides information on the residues like the momentum transfers and excited states with subsequent decays by gamma emission or fragmentation. In the occurrence of fission the mass distribution of the fragments at fixed excitation gives insight into the fission path (compare figure 1.5) [39].

2.1 Goals for the Setup

Resolution

The resolution of the setup depends on the uncertainties of the kinetic energies of both protons and their scattering angles. For a typical primary beam energy of E_{beam}=290 MeV/u available in the accelerator facility we have computed the contributions of the measured uncertainties to the overall resolution. In figure 2.1 the color displays the resulting numbers as a function of the resolutions of the individual measured quantities. Both, relative momentum resolution $\delta P/P$ and the precision of polar angles $\delta\theta$ of both protons strongly influence the resulting performance. The green lines show the permissible tolerances for the two protons at a negligible resolution of the other quantity to achieve an excitation energy resolution of σ_{Exc}=1 MeV (see equation (1.5)).

[1] RIKEN Nishina Center, 2-1 Hirosawa, Wako Saitama, 351-0198, Japan

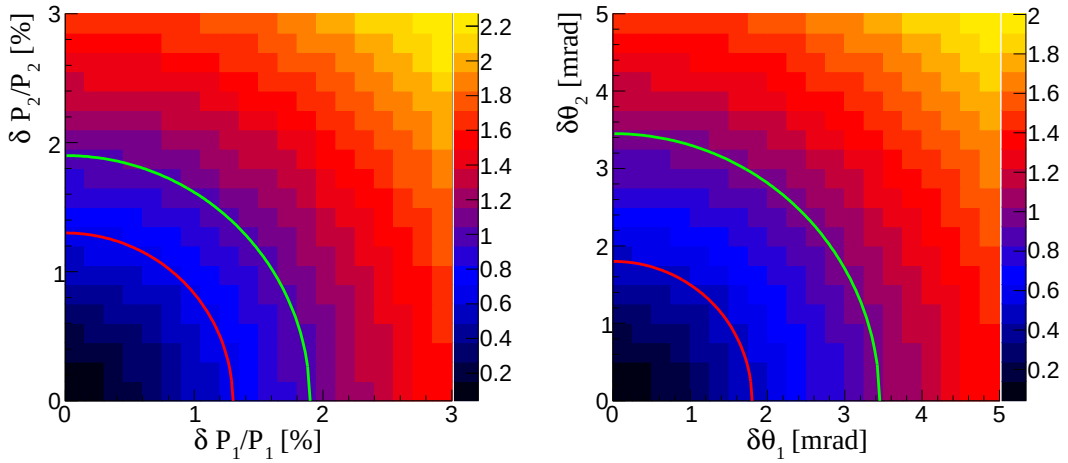

a) Momentum spread b) Angular scattering

Figure 2.1: Acceptable parameter tolerances for the excitation energy goal of 1 MeV (σ_{Exc} is drawn in the z-axis). The green lines are the maximum values assuming perfect resolution of the second quantity. In red lines are shown the picked target values.

Since both measured variables will be subject to limitations, we are looking for compensation on the basis of plausible, feasible resolutions. The goals are marked with the red lines. The average resolution for both proton energies E_p has to be better than

$$\sigma(\frac{\sigma^{E_p}}{E_p}) < 2.4\,\%. \tag{2.1}$$

The value for the average angular resolution is restricted to $\Delta\theta_p < 1.8\,\text{mrad}$ for each polar angle θ_p individually. The second requirement on the setup corresponds to an opening angular resolution of

$$\sigma(\Delta\theta_{op}) < 2.5\,\text{mrad}. \tag{2.2}$$

Systematic Uncertainties

Especially critical are systematic uncertainties which may directly lead to a modified experimental result (see equation (1.4) and the set goal in equation (1.5)). Since the true excitation energies of the residue in this first demonstrator experiment will be well-known the systematic offset is defined by the difference between the measured peak positions and the values from literature.

2.2 The Detector Setup Overview

The newly developed $(p, 2p)$ setup is aimed at the goals of equations (2.1) and (2.2). From the special kinematics of the reaction follows an optimized geometry

which can measure the momenta of the two emitted protons. The solid angle coverage is oriented towards the distribution of the emitted protons from the QFS $(p, 2p)$ reaction. Most events occur within a small range of the polar angles around the maximum at $\theta = 41\hat{A}^\circ$ (see figure 1.9 a)). Furthermore, the protons are approximately emitted in perpendicular directions[2].

The design is based on a two-armed tracker positioned at an angle of $42\hat{A}^\circ$ shifted from the beam line in the same plane[3]. It consists of layers of 100 µm thick silicon wafers with a pitch-size of 100 µm (silicon tracker) to determine the opening angle by reconstructing the vertex and, in line with the silicon detectors, 1 cm thick plastic scintillators (hodoscope arms) to measure the time-of-flights from which the energies of the particles are calculated (see the schematic drawing in figure 2.2).

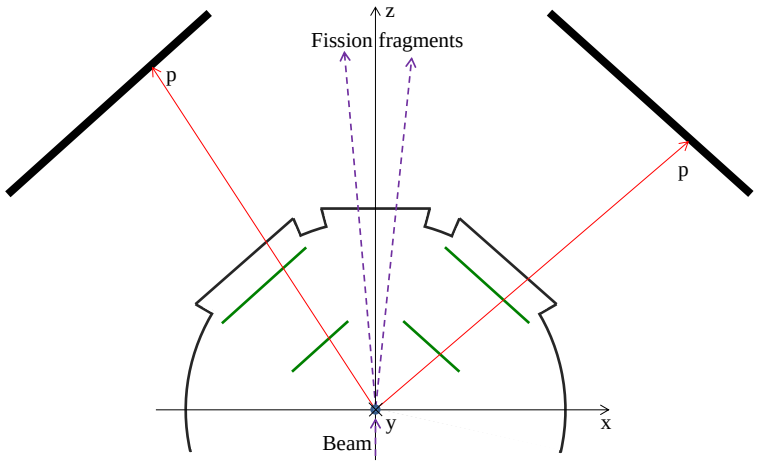

Figure 2.2: Schematic drawing of the $(p, 2p)$ setup. It consists of a silicon tracker and TOF detectors in two arms rotated $42\hat{A}^\circ$ around the beam-direction. The target is placed at the center of the vacuum chamber.

On the intersection line of the two arms the target is positioned in the center of the setup. The intended usage of liquid hydrogen targets makes a vacuum chamber necessary. Any material between the target and the position sensitive detectors would deteriorate the measurement of the opening angle and hence the chamber encloses the silicon tracker. For further measurements the angular straggling is irrelevant and the remaining detectors are outside the vacuum chamber. In order to avoid energy losses the sizes of the circular windows are chosen such that the beam projectiles, the residues respective fission fragments and the protons (in direction to the hodoscope arms) punch through thin Kapton® foils.

[2]The bound proton carries Fermi momentum away and hence the azimuth angle between the protons is washed out.

[3]In later experiments the beam energy will be lower (E_{beam}=250 MeV/u instead of the current E_{beam}=290 MeV/u) which increases the average polar angle to $\theta = 42\hat{A}^\circ$.

While the beam entrance with a diameter of 50 mm was made from a 50 µm foil, the large windows are closed with 160 µm thick Kapton® foils. For the proton windows the diameter corresponds to a polar angle of $\theta = 20\hat{A}^\circ$. In order to measure the fission fragments in detectors downstream the beam exit window is extended to $\pm 15\hat{A}^\circ$ such that fragments with typical mean velocities of 1 cm/ns (at E_{beam}=1 AGeV) perpendicular to the beam direction in the center-of-mass system [40] can pass.

The full setup is shown in figure 2.3 where the relevant distances are specified in the top view. The silicon tracker and the target are inside the vacuum chamber. In line with the silicon detectors, each nine rods of vertical plastic scintillators at a distance of 2 m form the hodoscope arms and complement the $(p, 2p)$ part. In addition to the two arm proton detection system, ancillary detectors are installed to characterize the full event. A thin plastic scintillator array (SBT) 1.3 m in front of the target monitors the beam rate and provides the time-of-flight reference. A beam drift chamber (BDC) with its exit window 60 cm in front of the target controls the beam position and focusing and provides high resolution tracking of the beam particles on the target. 1.5 m behind the reaction chamber an additional scintillator array (PID) is used to identify the heavy residues in mass and charge.

The angle coverage in the vertical axis is $\pm 9\hat{A}^\circ$ and in the horizontal axis the $(p, 2p)$ setup covers angles from 31° to 53°. This corresponds to a solid angle coverage of

$$\epsilon_{ST} = 1.8\,\% \tag{2.3}$$

of the 4π-sphere. The setup was optimized to the phase space of QFS $(p, 2p)$ kinematics such that

$$\epsilon_{kin} = 51.6\,\% \tag{2.4}$$

of the events are located within the bounds of the covered horizontal angles. Since the reaction is isotropic in the azimuth direction the main constraint is therefore the vertical angle coverage. The fraction of detected QFS $(p, 2p)$ reactions is the actual coverage of the effective two-proton emission area, i.e., the proportion of quasi-free scattered protons within the detector coverage,

$$\epsilon_{Cov} = \frac{\epsilon_{ST}}{\epsilon_{kin}} = 3.7\,\%. \tag{2.5}$$

Hence, the design dedicated to the kinematics of the $(p, 2p)$ reactions gathers over twice times more events as a percentage than the setup covers in the solid angles. The following sections describe the details of the individual detector elements and the associated electronics. It starts with the new $(p, 2p)$ setup consisting of the silicon tracker as the key apparatus, followed by the hodoscope arms.

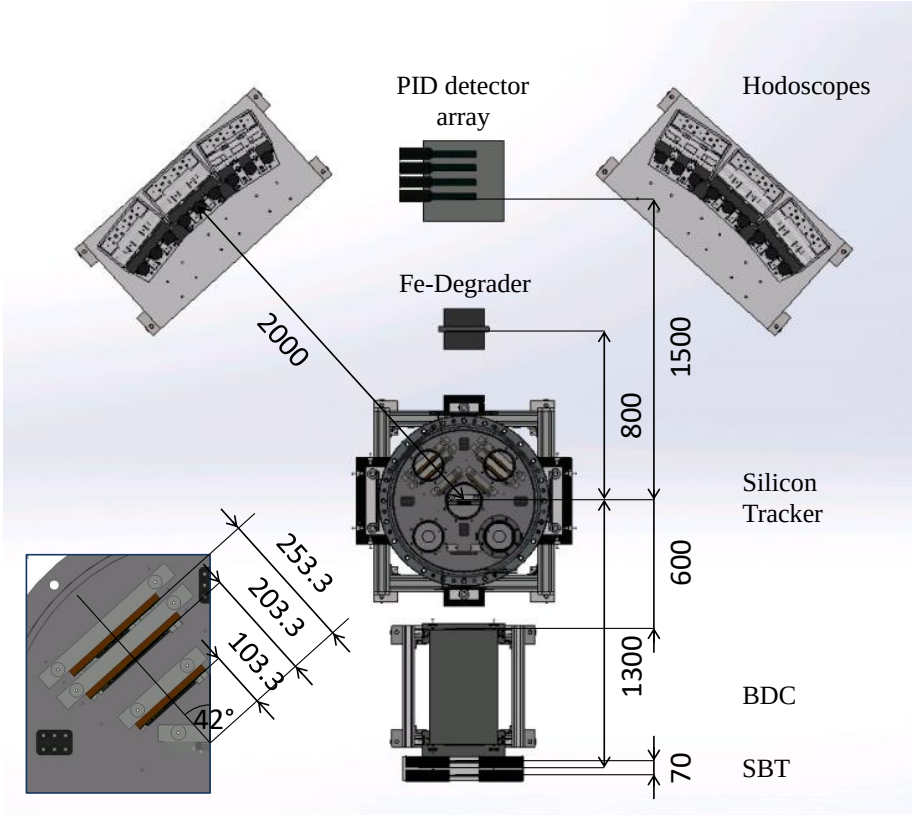

Figure 2.3: View of the full setup from above, with the detector names and their distances with respect to the target position (in mm). After the incoming beam passes the thin layers of the SBTs and the BDC, it passes the target at the center of the scattering chamber. The angular direction $\vec{v}/|v|$ of the scattered particles is measured with three layers of silicon detectors (silicon tracker, see also the small drawing, bottom left). Their velocities $|v|$ are measured with 9 plastic scintillators (hodoscope arms) on the left and right arm each. The identification of the residue nuclei is carried out with four plastic scintillators downstream in the PID array. *With courtesy of N. Chiga [41]*

2.2.1 Silicon Tracker

The new approach by exploiting the missing mass spectroscopy requires an extremely precise tracking of the two protons from the QFS process. To fulfill the very challenging requirements a new silicon detector setup optimized for beam energies around E_{beam}=300 MeV/u was designed, implemented and extensively tested.

Table 2.1 summarizes the requirements on the vertex reconstruction, i.e., the resolution of the reaction point. Most critical are the positions in the x- and z-direction whereas the precise knowledge of the y-direction is less important. Also the absolute position of the origin of reaction is crucial for the determination of the correct opening angle. Already small shifts δ^T_{syst} have high impact to the systematic uncertainty of the excitation energies.

The photo of the silicon tracker (see figure 2.4) illustrates the detector arrangement with the target position and figure 2.5 provides a schematic view of

Table 2.1: Requirements on the vertex reconstruction. The resolutions of the vertex reconstruction of the reaction point are characterized by the resolution of the coordinates (defined in figure 2.5)). The tolerable systematic shift from the true reaction point is defined by δ^T_{syst}.

Component	Required res. σ
x_T- and z_T-direction [µm]	190
y_T-direction [µm]	750
δ^T_{syst} [µm]	130

the concept. Since the protons are tracked by the silicon detectors they are chosen as thin as possible under the consideration of decreasing signal heights of the very fast protons ($E_{kin} > 200\,\mathrm{MeV}$) and the increasing angular straggling for the slow protons ($E_{kin} < 100\,\mathrm{MeV}$). The full charge needs to be collected in one strip to be above the noise thresholds. The spatial closeness to the target is limited by a required minimum distance to liquid hydrogen targets and by the passage between the two arms for the beam and fission fragments of 5 cm.

As a result three layers of 100 µm thick silicon detectors are placed in each arm of the silicon tracker. The first two layers have their strips in vertical direction while the strips of the third layer are aligned horizontally. They are placed perpendicular to the target direction to lower the probability for fast protons with sharp polar angles and small energy losses to distribute the deposit energy to neighboring strips. The distances from the center of the evacuated target chamber to the layers are 103.3 mm, 203.3 mm and 253.3 mm, respectively.

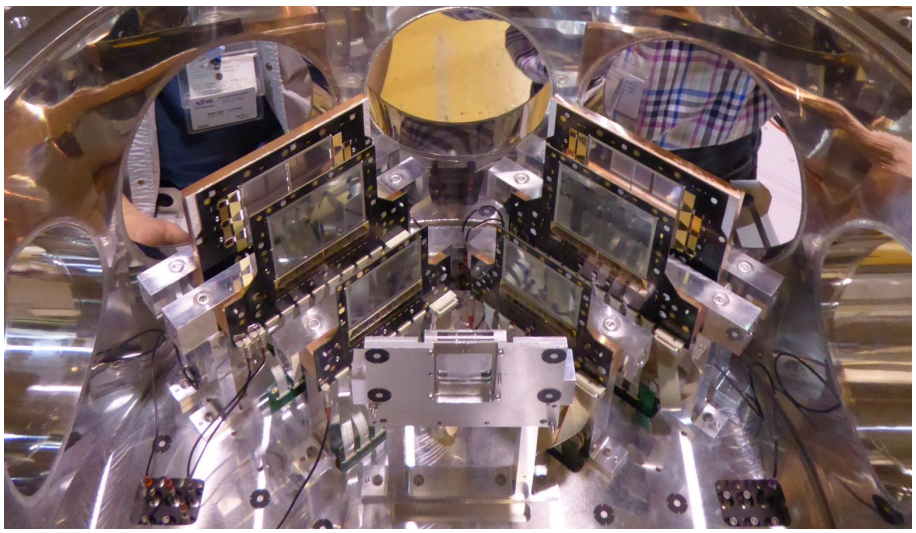

Figure 2.4: Photo of the silicon tracker with segmented target mounted in the vacuum chamber. The devices are mounted to the bottom of the chamber. The holding structure includes water pipes inside the legs to cool the detector part with the ASIC chips.

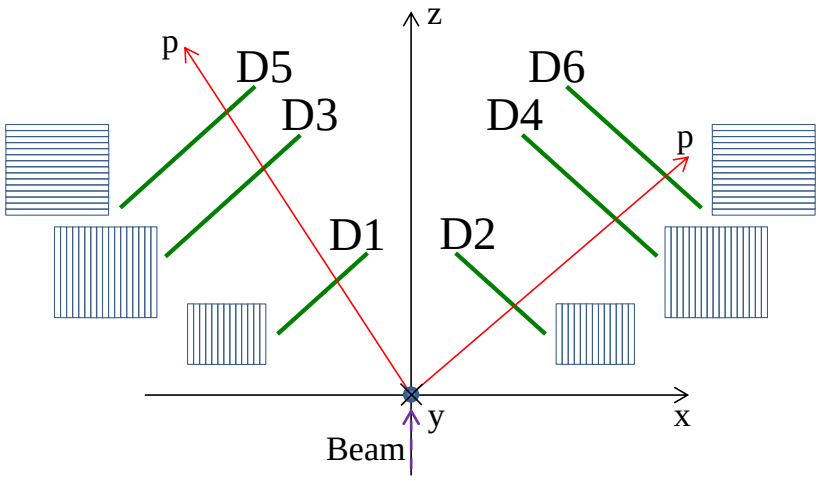

Figure 2.5: The schematic top view of the silicon tracker is drawn with the beam (dashed purple arrow) and two protons (red arrows). It consists of two arrays of silicon detectors rotated 42Â° around the beam-direction. The first two layers have their strips in vertical direction and the third ones are oriented horizontally. Both arms cover an acceptance of 31°<ϑ<53° and -9°<φ<9° determined by the size of the third layer. The detectors in the left arm are labeled with odd numbers D1, D3, D5 and the right armed detectors with even numbers D2, D4, D6.

In the subsequent subsections details of the silicon detectors are described starting with information of the silicon wafers. The silicon detector units process the collected charge and forward the amplified and shaped signals. Furthermore, the boards include markers and measuring devices to fulfill the high level of required position accuracy in the vertex reconstruction.

Design of the Silicon Wafer

The silicon wafers are specially fabricated highly segmented diode structures connected to IC technologies. The pn-junction of the p-type doped implants (p^+ strips) on the front face with their freely movable holes and the n-type silicon bulk (n-bulk) forms a depletion zone where the free charge carriers recombine and disappear. The formerly neutral n-bulk becomes charged and an E-field occurs [42]. The highest efficiency and best energy resolution is reached at a complete depletion of the n-bulk volume that is achieved by applying reverse biasing of -45 V between the p^+ strips and the n^+ layer at the backside of the wafer.

If a particle (see figure 2.6, red arrow) passes through the wafer, the charge is deposited in form of electron-hole pairs which drift separately in the E-field to the respective pole where they are absorbed. The holes, here illustrated with orange spheres, diffuse to the n^+ layer and the electrons (white spheres) reach the p^+ strips which transport the charge to the aluminum readout electrode carrying the AC-charge to the ASIC chips[4] whereas the dark current DC-component is suppressed by the integration of capacitors (coupled capacitance) realized by

[4]Amplification Specific Integrated Circuit

few µm thin insulating films [43]. Additional noise reduction is carried out by decoupling the diodes from the reverse bias voltage with resistors.

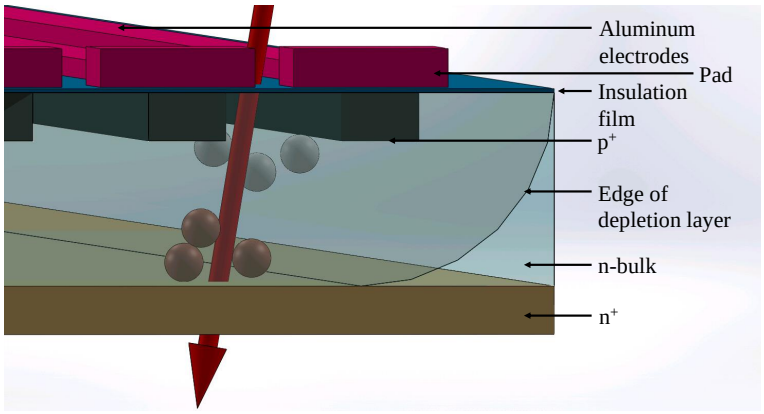

Figure 2.6: Schematic 3D view of the silicon wafer. The pn-junction forms an uniform electric field in the silicon substrate. Passing through particles, symbolized by the red arrow, lose energy by exciting electrons into the conduction band. The freely movable electrons and holes were collected by n- and p-strips.

Two types of the 100 µm thick rectangular single-sided silicon wafers (Type A and B from Hamamatsu) were used. They have the same size and structure but differ in the direction of the strips. In Type A, the strips are parallel to the shorter side whereas Type B has the strips along the longer side. The active surface for each wafer was $49.1 \times 76.8\,\mathrm{mm}$.

In table 2.2 we already anticipate the silicon tracker design and distinguish between the silicon detector units in the three layers. The first unit *L1* has a single wafer Type A, the second layer *L2* has two parallel arranged Type B wafer and in the case of the third layer *L3*, the neighboring strips and each second strips of two Type A wafers were connected (see figures A.2 a)-c)). The combination of two wafers to a single detector unit minimized the dead area between the wafer and also reduced the number of read-out channels and corresponding heat load to the vacuum part of the system. As a slight disadvantage the combination increases the capacitance per channel by a factor of 4 compared to the first unit.

Measurements of small signal heights ($E_{loss} \sim 50\,\mathrm{keV}$) in the silicon detectors are required to detect the path of protons with high kinetic energies. Therefore the signal-to-noise ratio must be sufficient high to unambiguously select the correct signals. The two main contributions to noise are the ASIC chips (electronics noise σ_{APV}) and the silicon wafers σ_{WAF}.

The electronics noise of the APV25 chips was measured to (see section A.4.2 for details)

$$\sigma_{APV} = 1.3\,\mathrm{keV}. \tag{2.6}$$

Table 2.2: Specifications of the silicon detectors. Three different types of silicon detectors were designed for the three layers of the silicon tracker. The noise levels are measured and are divided into the electronics noise σ_{APV} and the noise from the silicon wafer σ_{WAF}. The sum is presented in the last row σ_L

	Layer 1	Layer 2	Layer 3
Wafer	Type A	Type B	Type A
Size (h × l × t) [mm]	49.1×76.8×0.1	76.8×98.2×0.1	76.8×98.2×0.1
Pitchsize [µm]	100	100	200
Strip direction	vertical	vertical	horizontal
Terminal Capac (-45V) [pF]	242	177	242
Coup. Capac C_{CC} [pF/strip]	250	400	1000
Load resistance R_l [Ω/strip]	20	30	20
Resistor R [MΩ]	1.5	1.5	1.5
Noise $1\sigma_{APV}$ [keV]	1.3	1.3	1.3
Noise $1\sigma_{WAF}$ [keV]	1.5	2.0	4.0
Noise $1\sigma_L$ [keV]	2.0	2.4	4.2

It corresponds to the equivalent noise charge (ENC) of

$$ENC_{APV} = \frac{\sigma_{APV}}{3.6\,\mathrm{eV}} = 361\,e^- \tag{2.7}$$

which is higher compared to the value from literature [44],

$$ENC_{APV}^{theor.} = 246\,e^-. \tag{2.8}$$

The difference might come from the further processing of the signal in the subsequent electronics. The magnitude is the same in each detector design whereas the noise from the silicon wafer is specific and depends on the capacities, resistors and the integration time [45] (see table 2.2, row "σ_{WAF}"). Their contributions are higher than the electronics noise and increase with larger capacitance and resistance.

The total noise levels σ_L are the geometric mean of the two components (see table 2.2, row "σ_L"). All three detector units exhibit a signal-to-noise ratio better than 10:1 (in sigma) with respect to the smallest energy losses of $\sim 50\,\mathrm{keV}$. The ratios are sufficient to highly suppress noise without cutting physical relevant signals. Therefore, it was possible to discard all signals $< 3\sigma_L$ in an intermediate step in front of the event-building (see the operating principle in the below subsection *Read-Out Electronics on Detector Side*). This reduced the data traffic drastically from 17 kByte to 120 Byte assuming 30 signals still to be transferred to the data acquisition [46]. Remaining small signal heights were cut by the additional insertion of thresholds in the software analysis. The multiplicity of clusters in each detector could therefore be lowered close to 1 for the first two

layers whereas the averaged multiplicity is higher in the detectors of the third layers (see section A.4.3).

Design of the Silicon Detector Units

A long list of very specific conditions led to the detector design presented here. To meet strict requirements on mechanical precision the detector concept provides capabilities to measure the deviations from the fabrication process by printed markers, reflectors and holes for alignment pins. Figure 2.7 presents the component parts of the silicon detector L1 in the first layer.

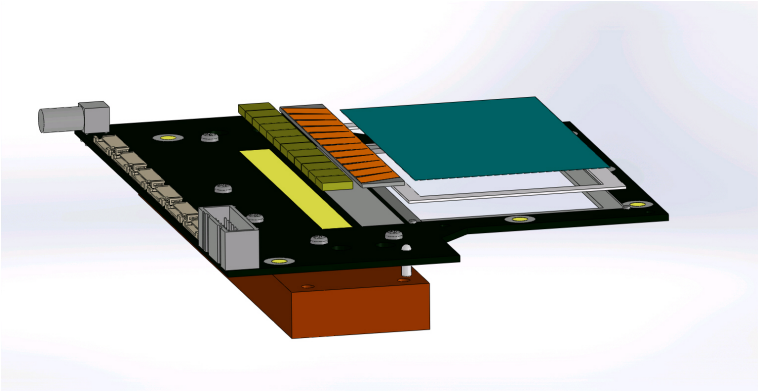

Figure 2.7: Schematic 3D view of the silicon detector Type L1. The composition is separated into layers to illustrate the structure. The PCB is fixed to a copper frame which provides cooling and the mechanical interface. The highest level shows the 12 ASIC-chips, the pitchadapter and the silicon wafer itself. Pictures of the three units are shown in the appendix, figure A.2.

The strips on the wafer are bonded to a pitchadapter with 18 µm thick aluminum wires which transmit the signals to 12 ASIC-chips APV25-S1 [47] with 128 channels each. To achieve the best performance of the read-out system only every second channel is connected to the pitchadapter aiming a compensation of the charge-depended baseline for the APV25 channels by using the unbonded neighboring channels as restorement parameters (see section A.4.2). The low-voltage differential signals (LVDS) trigger, clock input and the output are routed for each chip separately and are transferred to FFC-cables via FPC-sockets. Supply voltages for the APV25-chips, the slow control and thermometer device are supplied by a flat ribbon cable. A LEMO socket connects the high voltage to the board where the wires are spatially separated from the signal wires to avoid any noise transfer to the data stream. For the same reason of noise reduction, two low-pass filters with capacitances of C_1=10 nF and C_2=1 nF and resistors with R_1=50 kΩ and R_2=2 MΩ are located next to the LEMO socket and close to the wafer.

A cooling system for the detectors was necessary due to the high heat emission of the APV25-chips (0.3 W nominal per chip) which needed to be carried away. The heat transport from the APV25-chips to the copper frame is performed

straight through the PCB with electrically connected large area pads and many hole vias. An electric isolated thermal paste ensured the thermal transfer in vacuum environment to the copper frame. The opposite side of the copper frame was screwed with the detector holder that acted also as cooling device where inside 20Â°C tempered water circulates, regulated by a cooling machine. The thermometer at the PCB showed only a slightly higher temperature.

In order to protect the fragile silicon wafer from thermal stress, safety devices in the form of special glue techniques and materials were used. The silicon wafers were glued with two-component epoxy adhesive[5] at room temperature to a 0.64 mm thin and 4 mm wide AlN-ceramic frame which fits to a mold machined into the base PCB with a precision of 50 µm. The much more robust ceramic frame acts as intermediate layer with a coefficient of thermal expansion (α=4.5·10^{-6}K^{-1} [48]) similar to the silicon wafer. To avoid any mechanical stress it is connected with the PCB on three areas with elastic silicone glue: Along the side to the pads and on the opposing two corners. Hence the different heat expansion is balanced by the silicone glue. Both the silicon wafer and the ceramic frame expand almost the same if the temperature changes and the silicon wafer is protected from thermal stress.

Read-Out Electronics on Detector Side

The strips of the wafer were read-out by the APV25-chips which are analogue pipeline ASICs with 128 channels each of preamplifier and shaper with a maximum range of up to 8 MIP for the incoming signal height [47].

All measured charges per channel are continuously stored in a 192 column analogue memory ring buffer with a sample frequency of 40 MHz. The external trigger provides the read-out command for a specific delayed memory location and packs the signal height in the form of a 25 ns pulse shape into an analogue 128-channel multiplexer with a digital header and ender [47].

The multiplexed and shaped analogue signals from the APV25-chips are transmitted via 30 cm long FFC-cables and feedthroughs outside the vacuum chamber to ADCM-modules[6] with 8-channel 16-bit ADCs below the chamber. Each silicon detector has its own ADC-module. The FPGA serves as an interface to the event-builder and undertakes steps for reducing the amount of data. It eliminates the influence of the voltage drop down mentioned earlier as the reason to connect only every second channel on the ASIC-chips to the silicon wafer strips. Using pedestal-runs with random trigger, the FPGA applies zero-suppression. The data transfer of each ADCM module consists of 32-bit words for each channel with a fixed structure consisting of an error bit, the 6-bit ID number of the ADCM module, the 4-bit numbering of the APV25-chips on the silicon detector, followed by

[5] UHU Plus Endfest 300

[6] Analogue To Digital Converter Multi

a 7-bit number to distinguish the 128 channels with the final 14-bit information of the ADC value of the respective channel. The network traffic via optical fiber cables becomes minimized by sending events in packages to the event-builder [49].

2.2.2 Hodoscopes

Two hodoscope arms measure the time-of-flight (TOF). It is the second crucial dimension which needs a high resolution in this experiment. The energy resolution (see equation (2.1)) can be transformed to a required TOF resolution of

$$\sigma(\frac{\sigma^{TOF}}{TOF}) < 1.0\,\%. \tag{2.9}$$

Due to the additional Fermi momentum distribution of the struck proton high energetic protons up to E_{kin}=500 MeV can occur (see figure 1.9 e)). Since the probability of such high protons is low we limit the measurements to protons at kinetic energies E_{kin} <300 MeV. With a typical detector resolution of σ^{TOF} ∼100 ps [50] the TOF of the emitted protons of the QFS $(p, 2p)$ reactions need to be larger than 10 ns. This corresponds to a travel time of 2 m from the target position for the fastest protons and in average the TOF resolution should be σ^{TOF}=120 ps.

One hodoscope arm consists of three bundles, arranged in a circle, which contain three panels forming a flat surface, each. 18 plastic scintillators EJ-200 with the sizes $100 \times 10 \times 1$ cm are mounted vertically (see figure 2.8). The plastic scintillators are numbered from left to right. The left hodoscope consists of the detectors 0 to 8 and the right one of the detectors 9-17. The two hodoscope arms cover larger areas than the silicon tracker, ±13° in horizontal direction around ±42° and the coverage in the vertical direction is from -14° to 14°.

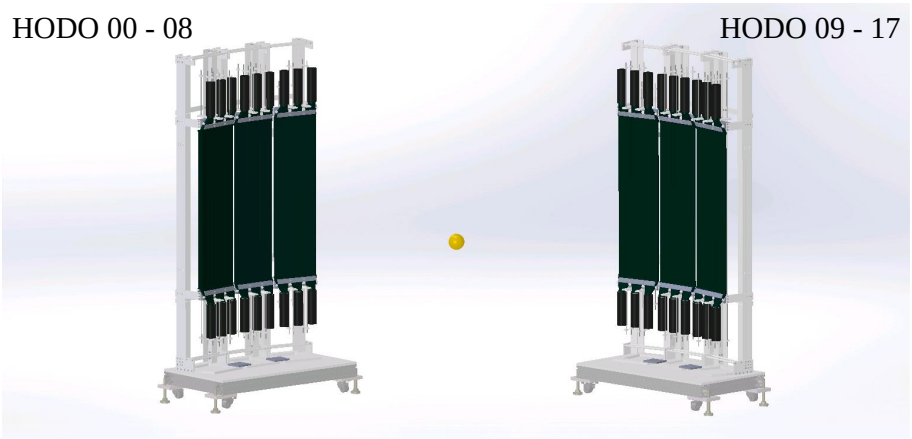

Figure 2.8: 3D model of the two-arm hodoscopes at a distance of 2 m from the target point (yellow sphere). Each arm consists of three units of three plastic scintillators. *With courtesy of N. Chiga [41]*

The signals were processed and digitized by standard NIM[7] and VME[8] based electronics modules. The circuit scheme in figure 2.9 shows the exemplary signal processing for one plastic scintillator with two PMTs. The output-signal is divided into two branches. One branch transmits the signals to the charge-to-digital converter (QDC) module CAEN V775 where the charge value is recorded. The signals in the second and third branch are discriminated and one signal line is directly processed by the time-to-digital converter (TDC) module CAEN V792 to give the timing information.

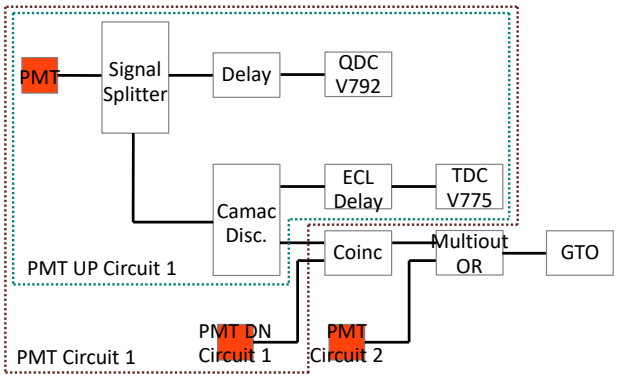

Figure 2.9: Circuit scheme of the hodoscope arms. The up (UP) and down (DN) PMT signals are divided into the QDC and TDC branch. Coincidence conditions cause the start of the trigger logic and forward the read-out request to the QDC and TDC modules.

Coincident responses of the two PMTs of the same plastic scintillator are required in the parallel coincidence module 2Fold-module N-RS 413. The coincidence between the two hodoscopes (PMT Circuit 1 & 2) is verified by the 4Fold-module LeCroy 365Al (Multiout OR). The trigger request to read-out the QDC and TDC values is made inside the general trigger operator GTO module B111 [51] which is also used for the SBT trigger logic (see section 2.2.3).

The residual sections explain additional detectors and electronic circuits used in this experiment. They can be replaced or modified depending on the individual requirement profiles.

2.2.3 Plastic Scintillators SBT

The SBT1 and SBT2 were used to provide the logic signal for the beam timing information as well as to serve as a part of the trigger logic. Therefore, all beam particles transported into the experimental room passed through these 2 mm thick plastic scintillators (EJ-200) read out by photo-multiplier tubes (PMTs) attached at the left and right ends of each slab. With an area of 25 cm^2 these detectors cover the full area of the beam pipe. Since its time is used as start time of other

[7]Nuclear Instrumentation Module
[8]Versa Module Europa bus

detectors (BDC and TOF detectors), its time resolution is included there and depends on their requirements. In particular the resolution of the TOFs of the protons (see equation (2.9)) requires a time resolution of the SBT of

$$\sigma^{SBT} < 75\,\text{ps}. \tag{2.10}$$

Figure 2.10 illustrates the circuit to process the SBT signals. The anode signals of each PMT was split into three branches. One was digitized by using QDC modules CAEN V792 to record the charge information of the signal. The two remaining branches were sent to a discriminator Phillips 0711 generating two independent logic signals to provide the timing information of SBT signals with a high precision. The discretized signals were processed in the CAEN multi-hit TDC V775 to record the timing information.

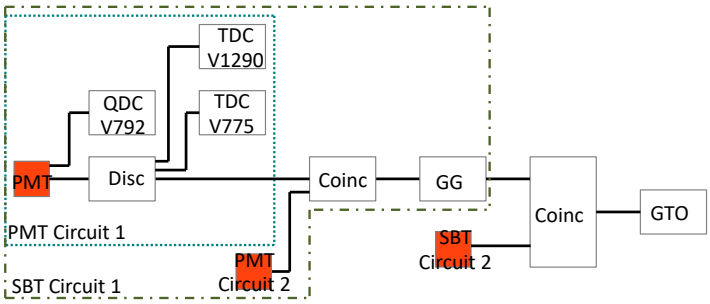

Figure 2.10: Circuit scheme of the SBT. The charge and time are recorded for each PMT individually. Coincident signals in all four PMTs provide the basis to start the data acquisition.

The logic signals were sent to the trigger circuit where the coincidence quad two-fold logic unit module Phillips Model 752 guarantees the forwarding of simultaneously measured signals which then joined the trigger logic in the GTO module driving the whole data acquisition system. The timing delays for the trigger logic were adjusted in a way that signals originating from the right PMT of the SBT2 defines the reference time for all measurements.

2.2.4 Beam Drift Chamber

The position of the incoming beam was determined by a beam drift chamber (BDC) with which the trajectory to the target position can also be extrapolated. It was placed just after the SBTs. A drift chamber is a gas-filled volumina with well-placed wires which act as anodes for gas amplification. In our case, we had five planes of seven and eight, respectively, wires for each x- and y-axis placed at a distance of 18 mm (see the summarized specifications in table 2.3).

The wires span an almost constant electric field between cathode wires. To avoid interactions between the planes and keep the field inside the box constant, shielding potentials with negative voltage were adjusted between each plane.

Table 2.3: Specifications of the BDC [52]. The table is subdivided into the plane and cell structure, the specifications of the used wires in the cells and effective size and readout electronics. The planes have vertical (x, x') and horizontal (y, y') wires with shielding (s) potentials between.

Plane structure	sxsysx'sy'sxsysx'sy'sxsys
Cell structure	
Drift length	9 mm
Half gap	6 mm
Gas mixture	Ar+C_2H_6(50%)
Wires	
Anode	30 µφ Au-W/Re
Field, shield, potential	80 µφ Au-Al
HV	2.0 kV
Effective area	126 mm × 126 mm
Readout	ASD (16ch × 6)

To reduce the effect of noise, amp-shaper-discriminators (ASDs) were directly mounted on the chamber casing. They receive the recorded charge from the anode wires and generate LVDS which are transmitted to two AMT-TDCs where they provide the start signal. The 1 µsec delayed master trigger signal then stops the TDCs. The time spent between start and stop is thus anti-proportional to the drift-time in the BDC.

2.2.5 PID Detector Array

The identification of the outgoing heavy fragments is important to select different reaction channels in the $(p, 2p)$ reaction. In the first stage of a demonstrator experiment with the light beam projectile ^{16}O (see section 3.2) it is sufficient to identify the residue element nitrogen. This is performed by the installation of a stack of plastic scintillators, the PID detector array setting, downstream in beam direction at a distance of 1.5 m from target position. Figure 2.11 shows this part of the setup. It consists of a 22 mm thick Fe-degrader that stops the primary beam and four 3 cm thick plastic scintillators, covering the polar angle of 0.05Â° around the beam direction. Each scintillator is read out single-sided by one PMT Hamamatsu H2431-50. The signal amplitudes were read-out by the QDC module CAEN V792.

The thicknesses were chosen in such a way that only one certain element is stopped in one of the scintillators. In table 2.4, the separation of nitrogen, carbon and boron due to the different energy losses and remaining kinetic energies is presented. The calculations were carried out with LISE++ [53].

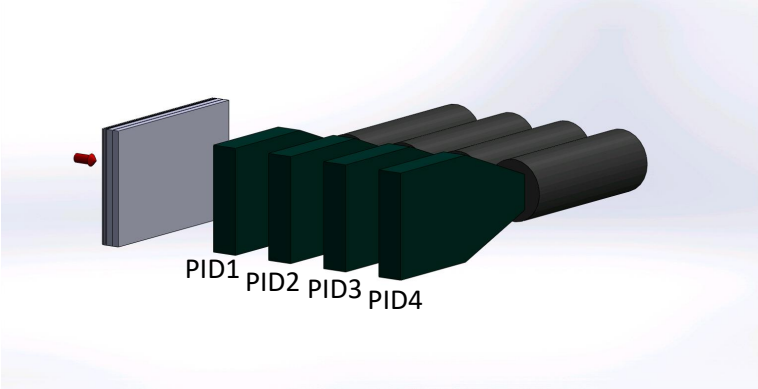

Figure 2.11: Drawing of the PID detector array setup with beam dump and four 3 cm thick plastic scintillators. The Fe-degrader stops the ^{16}O beam whereas the reaction products pass it and release characteristic energies in the PID detectors (see table 2.4).

Table 2.4: The energy losses ΔE in the PID detectors (first column) of the possible decay products of ^{16}O, calculated with LISE++. The first row lists possible occurring elements. The energy losses are calculated with respect to the kinetic energies of the residues taking into account the energy losses during the flight path. Momentum transfers in reaction processes are not considered.

ΔE [MeV]	^{15}N	^{14}N	^{13}N	^{14}C	^{13}C	^{12}C	^{11}B	^{10}B
PID 1	1420	992	572	691	782	1015	420	461
PID 2	0	0	0	1393	973	394	540	736
PID 3	0	0	0	0	0	0	892	342
PID 4	0	0	0	0	0	0	0	0

2.3 Trigger Logic

In order to reserve the DAQ for physical relevant events, the accepted trigger is selective for complete $(p, 2p)$ events which include the signal from the beam (beam trigger) and simultaneous signals in both arms of the hodoscopes (HODO trigger). The four PMTs of the SBT detectors establish the logical product for the beam trigger. The HODO trigger is defined by the product of the logical sum of the nine plastic scintillators in the two hodoscope arms. The BDC, silicon tracker and the PID detector array are slave devices and do not provide trigger requests.

A simplified circuit schematics is summarized in figure 2.12. Each plastic scintillator with its two PMTs is connected to 2-fold coincidence modules. The single trigger requests are forwarded to the trigger operator GTO (see the scheme in figure 2.13) where an internal coincidence check of 100 ns width between the two requested triggers and the readiness of all DAQ subsystems is mandatory in order to accept the composite trigger and distribute it to all DAQ subsystems to record and send the event to the event-builder. At the same time the next accepted trig-

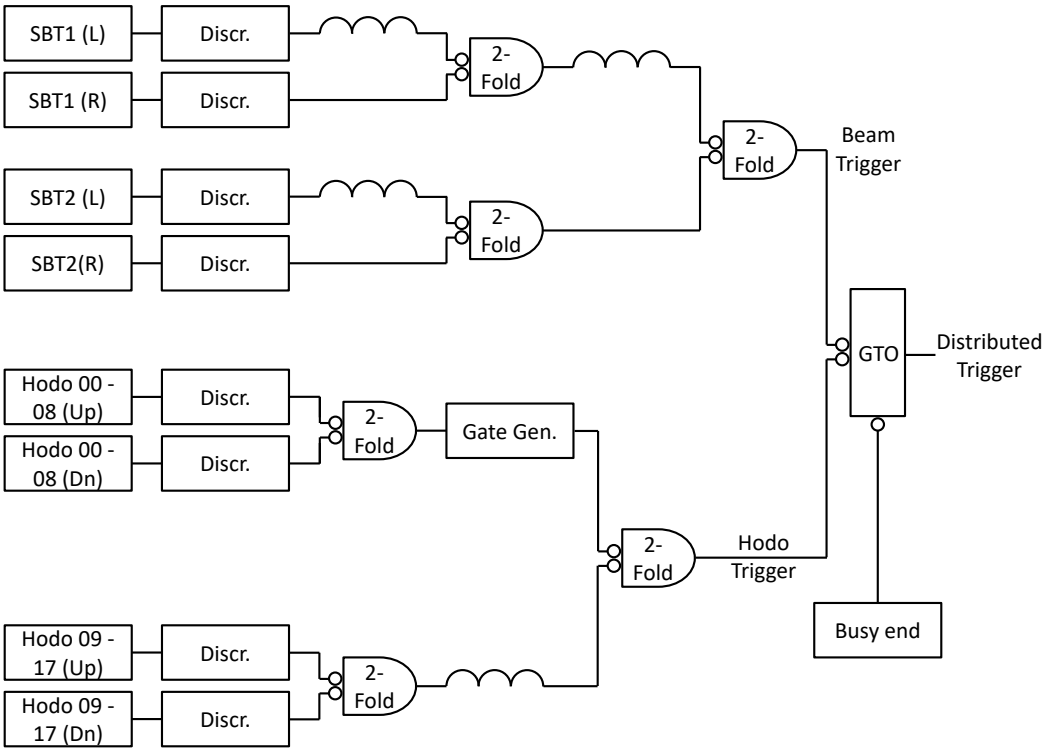

Figure 2.12: Simplified circuit scheme of the beam trigger (*up*) and the hodoscope trigger (*below*). Coinicident signals in the four PMTs of the SBT detectors and coincident fired TOF detectors in both arms of the hodoscopes are required to accept the trigger by the GTO module.

gers are suppressed by locked latches which open the VETO gate until the latches are cleared by the DAQ subsystems by providing their end-of-busy signals.

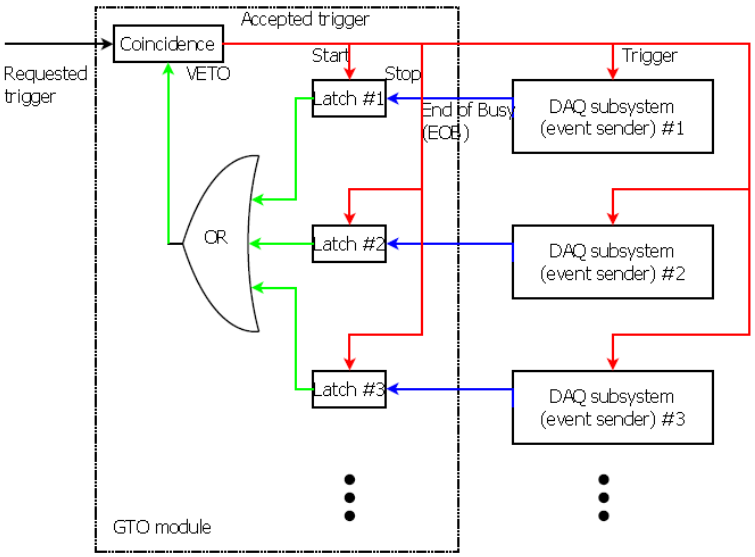

Figure 2.13: Circuit diagram of the trigger logic. The GTO module is the heart of the trigger handling. The triggers are accepted (Coincidence) and distributed to the DAQ subsystems. Simultaneously the latches are activated and prevent the next requested triggers. The VETO is revoked if all DAQ subsystems sent their busy-end-signals. *From* [54].

2.4 Data Acquisition

The data acquisition takes place via the RIBF standard DAQ *BABIRL-DAQ* [55], where a DAQ-PC as master event-builder reconstructs the subevents of the individual detectors as one event written in the RIBF data recording format RIDF [56] event-by-event likewise. The front-end machines serve as DAQ subsystems in the slave mode and communicate with the DAQ-PC (see table 2.5). They record the detector responses and transfer the digitized data via the VME[9] buses to the local network.

The silicon tracker readout is based on its own framework and therefore had to be integrated into the existing system. This was done in two essentially different ways. The subevents are connected through the common trigger configuration (event-by-event) and synchronized by a time stamping system. The dedicated readout system of the silicon tracker is based on the TRB3-platform [57][58] which has the tasks of handling the trigger, executing the event-building and sending the event in 32-bit words to the DAQ-PC. A newly implemented program converts the words into the 8-bit RIDF format and integrates them in the same event of the remaining detectors.

The second, independent method to couple the DAQ-subsystems was the separate measurements of time-stamps generated by an external 25 MHz frequency clock. In order to compare the values and ensure to probe the consistency of the single datastreams the time-stamp was recorded as an own subevent using the

[9] Versa Module Europa

Table 2.5: Components of the DAQ system. The SBT, hodoscopes and PID are read-out by the BABIRL-DAQ. The BDC and the silicon tracker have independent DAQs. All three datastreams are merged together in the event builder.

Component	Bus	Frontend	Detector
DAQ-PC	-	PC	Event builder
DAQ-a	VME	VMIVME 7768	SBT
DAQ-b	VME	TDC AMS-AMT-VME-3A	BDC
DAQ-c	VME	VMIVME 7807	SBT, HODO, PID
DAQ-d	*dedicated*	TRB3	Silicon Tracker

time-stamp module LUPO [59]. In the case of the silicon tracker a TRB3 specific, new developed scaler software scans the external clock with an internal 100 MHz clock and writes the time-stamp explicitly into the own subevent datastream of the silicon tracker. A manual reset at the beginning of each new run sets both scalers to zero.

Chapter 3

$^{16}\mathbf{O}(p,2p)^{15}\mathbf{N}$ Experiment at HIMAC

The experimental method and the full detector setup described in chapter 2 were commissioned in a full scale demonstrator experiment at the HIMAC[1] facility in the NIRS[2]. Using a well known system and a stable beam the various parameters were evaluated in an inverse kinematics $^{16}\mathrm{O}(p,2p)^{15}\mathrm{N}$ reaction. This system is ideal for such a test as light nuclei like oxygen have a limited number of reaction channels and the residual ^{15}N exhibits a level scheme with particularly well separated low lying states.

In addition to the physical schedule, the beam time was also used to test the performance of the silicon tracker under different conditions. For that a special target design was developed with which the limits of the vertex reconstruction were tested. The performance of the $(p,2p)$ setup using heavy projectiles was another goal and will be described in the outlook (see section 7.2).

3.1 Beam Accelerator Facility HIMAC

The experiment was carried out at the heavy ion synchrotron complex HIMAC. The injector Alvarez linac accelerates the ion beam to the two identical 800 MeV/u synchrotron rings [60] (see figure 3.1). During daytime the beam is delivered to the clinical therapy rooms. At night, biological, medical and physical experiments are conducted. Our experiment occupied the physics hall 2. The setup follows the drawing in figure 2.2 and consists of the $(p,2p)$ setup, the SBT detectors, the BDC and the PID detector array.

It went under the label H342 and took place from February 22 to 26, 2016 during the night shifts from 9 pm to 7 am. The beam for the first four days was ^{16}O and the last day was reserved for ^{132}Xe, with the primary beam energies

[1] Heavy Ion Medical Accelerator in Chiba

[2] National Institute of Radiological Sciences, 4-9-1 Anagawa, Inage-ku, Chiba 263-8555, Japan

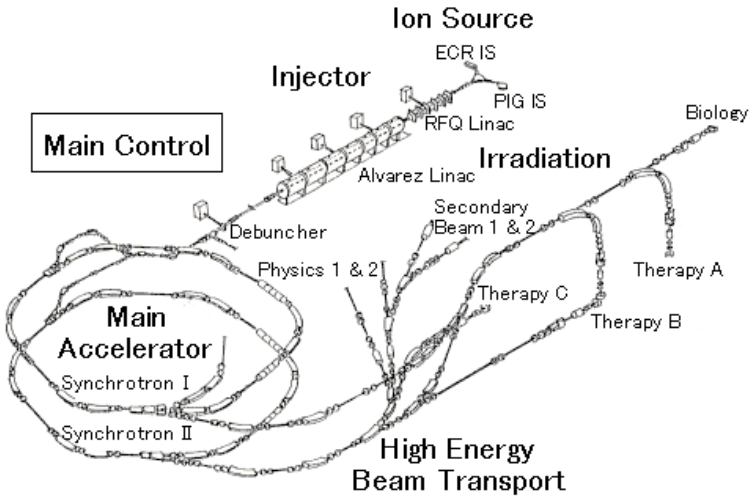

Figure 3.1: Bird's-eye view of the HIMAC accelerator facility. In the Physics hall 2 our experiment H342 was installed, *from* [61].

of 290 MeV/u each. The intensity was $4 \cdot 10^5$ particles per spill (pps) with a repetition of 3.3 seconds where the particle flow was accumulated in 1 second (see figure 3.2).

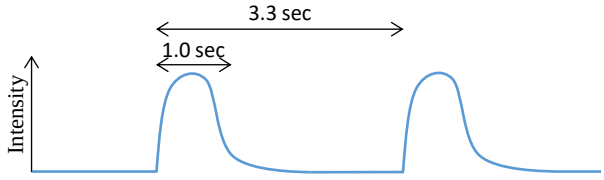

Figure 3.2: Shape of the beam particle spill at HIMAC facility. The synchrotron provides a pulsed beam every 3.3 seconds where most of the beam is delivered within 1 second.

3.2 Excitation Spectrum of ^{15}N

Excited states close to the Fermi surface of nuclei with closed shells show a clear single-particle behavior, i.e., from the shell model a simplified description can be deduced by means of the independent-particle model in which the nucleons move freely in a mean field potential. The ground state configuration of the beam nucleus ^{16}O, $(1s_{1/2})^2(1p_{3/2})^4(1p_{1/2})^2$ has occupied, completely filled shells up to the $1p_{1/2}$ shell both for protons and neutrons (see figure 3.3 a)[3]). The target proton will knock out one proton from the l=1 orbit, either from the $1p_{1/2}$ shell (see figure 3.3 b)) or from the lower $1p_{3/2}$ shell (see figure 3.3 c)).

The level scheme of ^{15}N in figure 3.4 a) is abridged to the relevant transitions below the separation energies S_n and S_p. A population of the low-lying positive

[3]The neutron part is not shown.

parity states $1d_{5/2}$ and outer $2s_{1/2}$ is not possible in the direct one-step process since the necessary spin for the spin flip has to be carried away by the struck proton. The reaction with the innermost unbound s-hole state leads to broad, more continuously distributed excitations higher than the neutron and proton separation energies S_n and S_p of ^{15}N (see figure 3.4 b)) and the emission of an additional nucleon becomes likely [62].

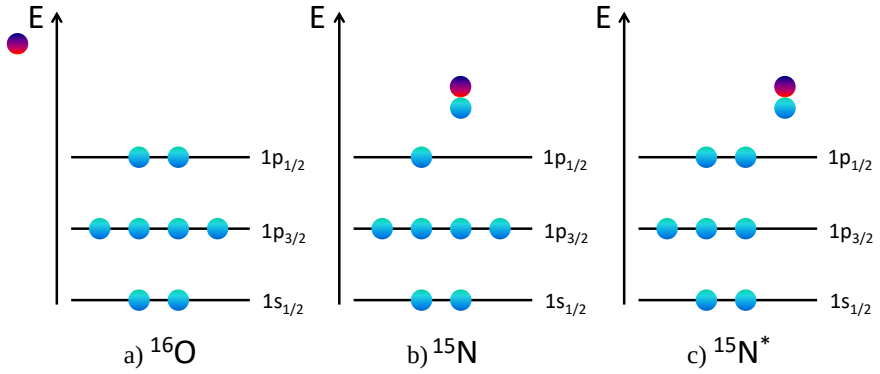

Figure 3.3: Shell occupation of ^{16}O and ^{15}N for the protons. In the direct one-step proton scattering, either one proton from the $p_{3/2}$ or $p_{1/2}$ is removed by the purple-red target proton (at rest) and the residue nucleus ^{15}N remains in its ground state (see b)) or first excited state (see c)).

The new-formed ^{15}N nucleus is hence in the ground state $1p^-_{1/2}$ or in the first excited state $1p^-_{3/2}$ both with negative parity. The latter excitation is fragmented into a strong state at 6.32 MeV and weakly populated states at 9.93 MeV and 10.70 MeV stemming from couplings of the particle-hole configurations with the continuum states at the Fermi surface and occupy therefore also states above the Fermi energy [63]. The total $(p, 2p)$ cross section is calculated to $\sigma_{gs} = 13.2$ mbarn and $\sigma_{es} = 25.1$ mbarn for the ground state and first excited state transitions [28].

The two peaks at E_{Exc}=0 and 6.3 MeV are well distinguishable and serve to test the linearity and consistency of the calibrations for the excitation energies over a comparatively large range. The resolution of the $(p, 2p)$ setup corresponds to the width of the two peaks. Systematic shifts in the peak structure as a function of the emission angles of the two protons are also investigated and corrected if necessary. In conclusion the requirements of high statistics and large separation of the peaks in our demonstrator experiment are fully accomplished with the choice of this beam.

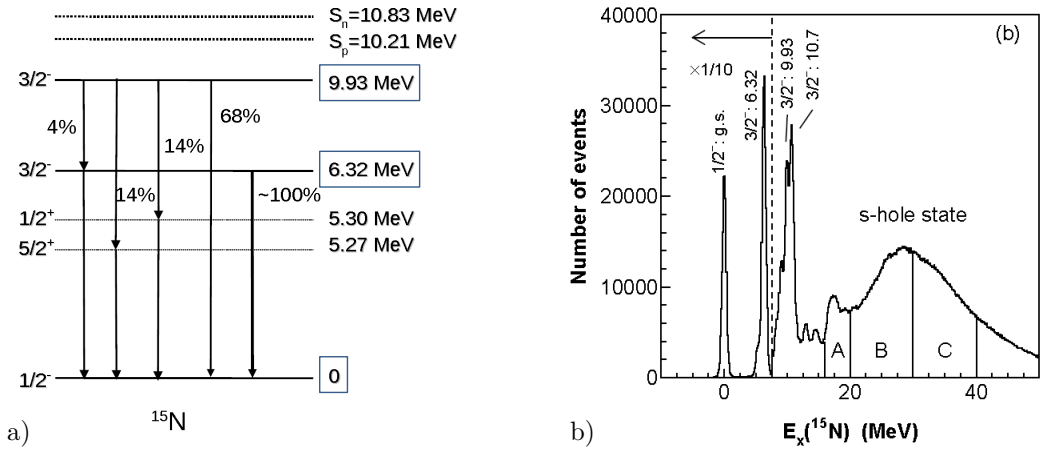

Figure 3.4: Reduced level scheme of ^{15}N (see a)) *from* [64] [65] (Modifications: The three possible states are outlined in blue). States with positive spin parity are ruled out in this this type of reaction. The excitation energy spectrum of ^{15}N in b) (*taken from* [62]) was measured after the $^{16}O(p, 2p)^{15}N$ reaction in normal kinematics. The excited states in the ground state and first excited state are sharp, while the knock-out of a proton from the unbound s-hole state leads to a broad energy distribution. The spectrum is scaled by 1/10 left of the vertical dashed line.

3.3 Optical Detector Measurement

The positions of the individual silicon detectors have high impact on the resolution of the opening angle and must be known with an accuracy of few hundred µm. To determine the energy of the protons using TOF measurements, the flight distance is the second quantity to be known. Measuring accuracies of a few millimeters are sufficient for this. Hence, the mapping of the detectors is important in the experiment.

The detector positions are surveyed by the photogrammetry system of *Geodetic Systems Inc.* [66]. Reflecting markers were attached to each device (see figure A.7 with circular grey reflecting markers on the silicon detectors) and photographed. The pictures were analyzed with the software program *V-Stars* [66] to calculate the distances, planes and angles in order to connect them with each other and create a 3D-model of the setup with the visualization of the whole setup (see figure 3.5 a) (here, without silicon tracker). The full surfaces of the nine TOF detectors on each arm and the SBT detectors are reconstructed. For the surfaces of the BDC and the PID detector array it was sufficient to partly model the planes. Figure 3.5 b) focuses on the target chamber: Six green planes in the two arms represent the silicon detector units. The target holding structure is placed in the middle of the red circle, symbolizing the bottom of the chamber.

The positions of the active silicon detector parts, i.e., the silicon wafers are defined by the distances and angles with respect to the target chamber center but also by horizontal shifts along the detector PCB. While the distances and angles are in accordance with the values of the detector PCB and fully determined by

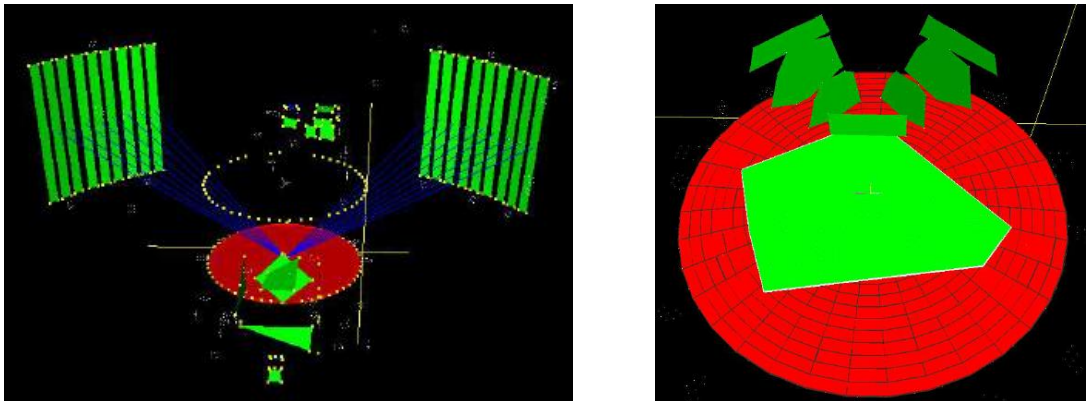

a) b)

Figure 3.5: Photogrammetry analysis of the whole setup (see a)) and of the silicon tracker (see b)). The green planes define the surface of detectors each. The red bottom part defines the target chamber.

the photogrammety system the measurement of the shifts demands additional information. Therefore we emphasized the need of precise position determination of the individual parts (see section 2.2.1) and each part was equipped with defined markers which could be then surveyed by microscope. A typical picture of the deviations is shown in figure 3.6 where the discrepancies between the markers are measured.

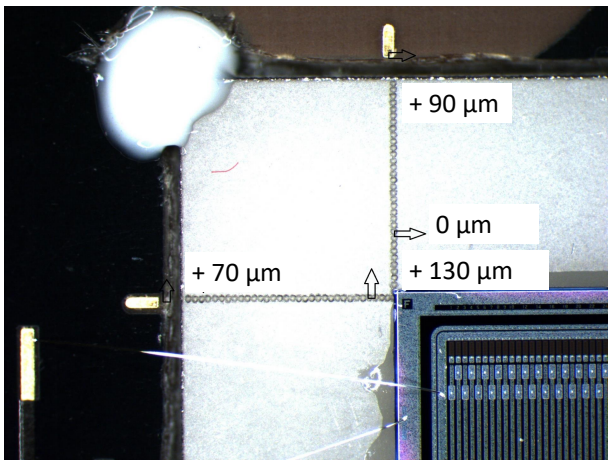

Figure 3.6: Zoom into the position markers on the silicon detector. The edge of the wafer should lie on the edge of the markers lasered in the ceramic frame. The rectangular lines on the ceramic frame itself find an equivalent on the PCB.

The silicon detector positions relative to the origin of the coordinate system are listed in table 3.1 (row "Photographic anal."). Uncertainties arise from the limited accuracies of the photogrammetry system and from the additional markers (see table 3.2). The analysis program *V-Stars* specifies the statistical uncertainty σ_{stat}^{PHG} on the basis of the large amount of pictures produced from different point of views. Furthermore, the systematic error σ_{syst}^{PHG} takes into account the uncertainty

Table 3.1: Comparison between the detector positions from the schematic drawings (used in the Geant4 simulations) and the deviations determined by the photographic analysis and the self-calibration. The deviations for *distance* and *angle* are additive to the set values, negative *shift* means a movement to the left and correspondingly a positive *shift* means a right shifted detector.

Method	Det. 1			Det. 2		
	Dist. [mm]	Shift [mm]	Angle [deg]	Dist. [mm]	Shift [mm]	Angle [deg]
Geant4 Simulation	103.30±0.02	±0.12	-42.00±0.01	103.30±0.02	±0.12	42.00±0.01
Photographic anal.	-0.01±0.10	-0.06±0.14	0.02±0.01	-0.13±0.10	0.19±0.14	-0.05±0.01
Self-calibration	-0.20±0.05	0.05±0.05	–	0.20±0.05	0.15±0.05	–
Method	Det. 3			Det. 4		
	Dist. [mm]	Shift [mm]	Angle [deg]	Dist. [mm]	Shift [mm]	Angle [deg]
Geant4 Simulation	203.30±0.02	±0.12	-42.00±0.01	203.30±0.02	±0.12	42.00±0.01
Photographic anal.	-0.14±0.10	0.16±0.14	0.05±0.01	-0.01±0.10	0.02±0.14	-0.01±0.01
Self-calibration	0.20±0.05	0.15±0.05	–	-0.20±0.05	-0.05±0.05	–

in the determination of the correct scale. The uncertainties of the planes σ_{plane}^{PHG} and of the angles σ_{ang}^{PHG} coming from the photogrammetry system are

$$\sigma_{plane}^{PHG} = 95\,\mu\text{m} \quad \text{resp.} \quad \sigma_{ang}^{PHG} = 2.6\,\text{mrad}. \tag{3.1}$$

While the error calculation of the distance and the angle includes only the uncertainty of the photogrammetry system

$$\sigma_{dist}^{PHT} = \sigma_{plane}^{PHG} \quad \text{resp.} \quad \sigma_{ang}^{PHT} = \sigma_{ang}^{PHG} \tag{3.2}$$

the horizontal shifts of the wafers along the PCB board are measured by markers on the boards with additional uncertainties σ_i (see the lower half of table 3.2) which can be seen as statistically independent, i.e.,

$$\sigma_{stat}^{PHT} = \sqrt{\sum_{i=1}^{3} \sigma_i^2} = 81\,\mu\text{m}. \tag{3.3}$$

The resolution σ_{shift}^{PHT} is obtained by the sum of the uncertainties,

$$\sigma_{shift}^{PHT} = \sqrt{(\sigma_{stat}^{PHT})^2 + (\sigma_{stat}^{PHG})^2} + \sigma_{syst}^{PHG} = 143\,\mu\text{m}. \tag{3.4}$$

While the uncertainties of the three parameters distance, angle and shifts are absolutely sufficient for the remaining detector positions they are even close to the requirements needed for the silicon tracker (see equations (5.5) and (5.7)). However, later analysis showed that the user-selected zero of the coordinate system turned out to be a drawback since any shift creates systematic offsets of the detector positions. The lack of redundant information makes it analytically impossible to set the zero at the same position as the zero of the schematic drawings. As a result, arbitrary large systematic shifts cannot be controlled. Shifts,

Table 3.2: Uncertainties of the single detector parts in order to determine the position of the wafers relative to the absolute detector position.

Component		Resolution
Photogrammetry system		
Statistical uncertainty [µm]/[mrad]	σ_{stat}^{PHG}	45/1.2
Systematic uncertainty [µm]/[mrad]	σ_{syst}^{PHG}	50/1.4
Markers on silicon board		
PCB: Drilling pattern to conductive pattern outer layers [µm] [67]	σ_1	60
Wafer: Size [µm]	σ_2	20
Accuracy of the optical correction [µm]	σ_3	50

however, have strong influence on the resolution and offsets of the opening angles. Therefore, a new method needed to be developed with a complete different approach (see section 5.4).

3.4 Target Design

The design of the target should provide information about the reconstruction power of the silicon tracker system and allows for a self-consistent calibration by using compositions of foils and fibers with thicknesses below the expected resolution of the silicon tracker.

We decided to use polyethylene and polypropylene as target materials. The plastics are available in many molds and have very high purities of CH_2 chains. The foil's thicknesses range from 100 µm to 1.8 mm. In the thin foils with 100 µm thickness, a pattern of 1.5 mm diameter holes at well defined distances are drilled. Fiber target units consist of eight columns of 150 µm thin fibers in two rows with a distance of 2 mm on both sides of the mounting frame. The two rows have a horizontal offset of 1 mm. Additionally, pure carbon foils were prepared for background evaluation. The targets were glued on identical 2.00(5) mm thick aluminum frames with precision fittings to provide an alignment uncertainty better than $\Delta xz < 20\,\mu m$.

Table 3.3 summarizes the target configurations in the experimental runs. The first two days aim to generate high statistics of $(p, 2p)$ events and thick targets were chosen. The subsequent days focused on the calibration of the silicon tracker. The 100 µm thin foils are supposed to show the intrinsic resolution of the silicon tracker, since the angular straggling becomes almost negligible. The target composition of the fourth day in the experiment is used as the reference target (see figure 3.7). It is a stack of one 50 µm thick diamond film, two 100 µm thick polyethylene foils, d=150 µm thick polypropylene fibers and 2 mm spacers in between.

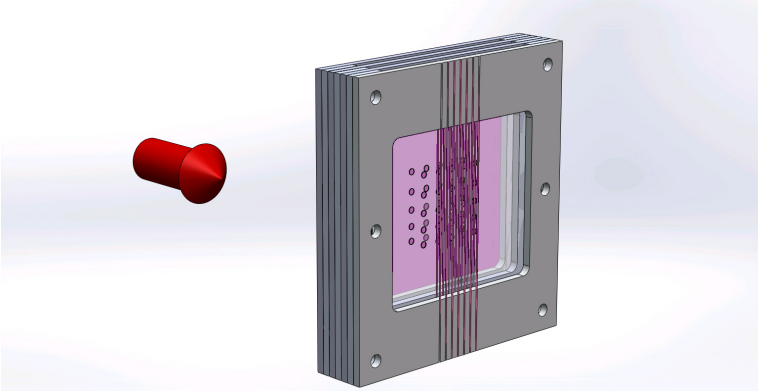

Figure 3.7: Assembly of the target for the fourth day, from upstream to downstream: 50 µm thin diamond film, 2×100 µm thin CH_2 foils with hole pattern and two layers of 150 µm fibers. The red arrow points to the beam direction.

The absolute target positions were determined using the photographic methods (see section 3.3). Reflecting markers were attached on the target holding structure to derive its position relative to the silicon tracker using the information obtained by the photogrammetry system. The individual stacks were assembled and individually measured with a caliper gauge (see table 3.4 "*Tracker*").

Table 3.3: Configuration of the target assembly in the z-positions. The values in the brackets correspond to the thicknesses of the targets in the unit [µm]. The amendment *-P* means a pattern foil and *-F* stands for a row of fibers. The CH_2 foils consist of polyethylene, the fibers are made of polypropylene. The material for the carbon background foils is diamond.

	-11 mm	-7 mm	-5 mm	-3 mm	-1 mm	1 mm	3 mm
Day 1	CH_2 (500)		CH_2 (1200)			CH_2 (500)	
Day 2		CH_2 (1200)			CH_2-P (150)		
Day 3		CH_2-P (100)		CH_2-F (150)	CH_2-F (150)		
Day 4	C (50)		CH_2-P (100)		CH_2-P (100)	CH_2-F (150)	CH_2-F (150)
Day 5	CH_2 (1200)		C (50)	CH_2-F (150)	CH_2-F (150)		

A separation of $\Delta z^{PHT}_{3\to4}$=2.00 mm and $\Delta z^{PHT}_{4\to5}$=2.01 mm is measured for the targets 3, 4 and 5 in accordance with the schematic drawings. The distance between the first foil and the second foil of $\Delta z^{PHT}_{1\to2}$=6.17 mm and between the second and third foil, namely $\Delta z^{PHT}_{2\to3}$=4.14 mm are larger than expected and are caused mainly due to the glue between the aluminum stacks and the target foils.

Due to the slightly different thicknesses both within the aluminum frames and the glue applied between frames and foils, we take into account an uncertainty of

$$\sigma^{TGT}_{stat} = 50\,\mu\text{m}. \tag{3.5}$$

The total uncertainty is the sum of the uncertainties of the position determination of the target holder structure (see table 3.2 "Photogrammetry system") and of the measurement of the single target foils, i.e.,

$$\sigma_{tgt}^{PHT} = \sqrt{(\sigma_{stat}^{TGT})^2 + (\sigma_{stat}^{PHG})^2} + \sigma_{syst}^{PHG} = 136\,\mu\text{m}. \tag{3.6}$$

Table 3.4: Positions and widths of the target assembly reconstructed by two particles in the silicon tracker arms in the Geant4 simulation (using the target and detector positions from the technical drawings) and in the experimental data with different silicon detector positions. The placements in the photographic analysis are in the fourth and fifth row with two entries for the target position. The upper row *Target* lists the positions coming directly from the photographic measurement, the reconstructed z-positions using the silicon tracker position are entered in the line *Tracker*. The results for the self-calibrated analysis are shown in the last row. The target distances among each other are the same for all types of reconstruction. However, there are deviations in the absolute positioning.

Position [mm] / Width [µm]	z_{tgt}	σ_{tgt}	z_{tgt}	σ_{tgt}	z_{tgt}	σ_{tgt}	z_{tgt}	σ_{tgt}	z_{tgt}	σ_{tgt}
Target plane	1		2		3		4		5	
Geant4 Simulation	-11.00	197	-5.00	191	-1.00	184	1.00	183	3.00	180
Photographic anal. *Target*	-10.80	—	-4.63	—	-0.49	—	1.51	—	3.51	—
Photographic anal. *Tracker*	-10.20	234	-4.03	211	0.11	197	2.11	166	4.12	184
Self-calibration	-10.05	229	-3.87	205	0.26	189	2.29	164	4.25	186

Chapter 4

Calibration

The conversion of the recorded values into physical units is conducted by the calibration of the detector channels. Special focus was placed on the time-of-flight calibration for the SBT detectors and hodoscope arms (sections 4.1 and 4.3) where each output channel was treated individually. Section 4.2 deals with the drift time to drift length calibration of the BDC. A detector-based energy calibration of the silicon tracker in section 4.4 is sufficient for later analysis instead of calibrating each individual channel. For the same reason, only the first detector was calibrated in the PID detector array in section 4.5.

The analysis routines were written in the C++ based ROOT framework, version 5.34/34 [68][69].

4.1 SBTs

The scintillator beam trigger (SBT) is a x-y large scintillator read out by two PMTs one on each vertical edges. It initiates the beam trigger and defines the start time of the DAQ. Achieving high time resolution for the SBTs is therefore essential for all other detectors. We used the TDC raw channels, set to a resolution of 35 ps per least significant bit (LSB), for the calibration of the physical time unit. The calibration was carried out by assigning pulses, generated by the time calibrator module Ortec 462 [70], using different time periods with a binning of 10 ns and a linear fit function (see figure A.11 and table A.3).

For background reduction and walk correction, in addition the signal amplitudes QDC are measured. This was necessary since particles with equal mass over charge A/Z ratio are difficult to separate from the actual beam and are also accelerated during the beam transport. Furthermore, our setup did not determine the beam energy and hence a second source of background are correct beam projectiles but with varied kinetic energies than tuned in the accelerator. This can happen if, e.g., a part of the beam crosses the edges of a pinhole aperture inside the accelerating process. Both background signals are distinguishable from the

primary beam in the SBT detectors either by different signal amplitudes QDC or different particle velocities.

From the flight time between the two scintillators and the signal amplitude it is possible to choose the nominal ^{16}O beam particles. Figure 4.1 a) shows the associated spectrum with the deposit mean charge [71] collected by the left and right PMTs

$$QDC_{SBT2} = \sqrt{QDC_{SBT2L} \cdot QDC_{SBT2R}} \tag{4.1}$$

in the SBT2 detector with respect to the time difference Δt between the mean times t_{SBT1} and t_{SBT2} of the two scintillators SBT1 and SBT2, i.e.,

$$\Delta t = t_{SBT1} - t_{SBT2} = \frac{1}{2}(t_{SBT1L} + t_{SBT1R}) - \frac{1}{2}(t_{SBT2L} + t_{SBT2R}). \tag{4.2}$$

The mean value of Δt has an offset of t_{const}=355 ps which corresponds to the TOF of the beam nuclei between the two scintillator plains at a distance of 7 cm (see figure 4.1 b)).

Three maxima exist around QDC_{SBT2}=750, 1250 and 1850 with the same Δt. Allocating the highest maximum to the primary beam, ^{16}O is identified at the QDC_{SBT2} value around 1250. In order to select exactly one particle in each event and to avoid pile up effects we only accept those with QDC_{SBT2} signals measured inside the two black borders[1].

Deposit charge dependent time corrections such as those required for the hodoscopes in section 4.3 are not carried out here. The precisely defined and sharp energy of the primary beam in figure 4.1 a) generates the same deposit charges in the small plastic scintillators where no significant walk contribution could be identified.

The reference system of all measured times is that of the right PMT of the detector SBT2. Its time signal is always set to zero and since it provides the start signal for the DAQ the other times refer to that value, i.e., they include its time resolution and its dependency on the hit position in the spatial expanded plastic scintillator. The timing fluctuations are balanced by redefining the start time to the time difference Δt with the offset t_{const} such that the mean value becomes zero, i.e., the transformation between the start time of the DAQ t_{SBT2R} into the zero point is

$$t_{zero} = \Delta t - t_{const}. \tag{4.3}$$

In respect to a physical meaningful time information we place the zero point t_{zero} in the target center and refer all particle flight times to that origin.

[1] This corresponds to 5σ of the normal distributed time distribution in figure 4.1 b).

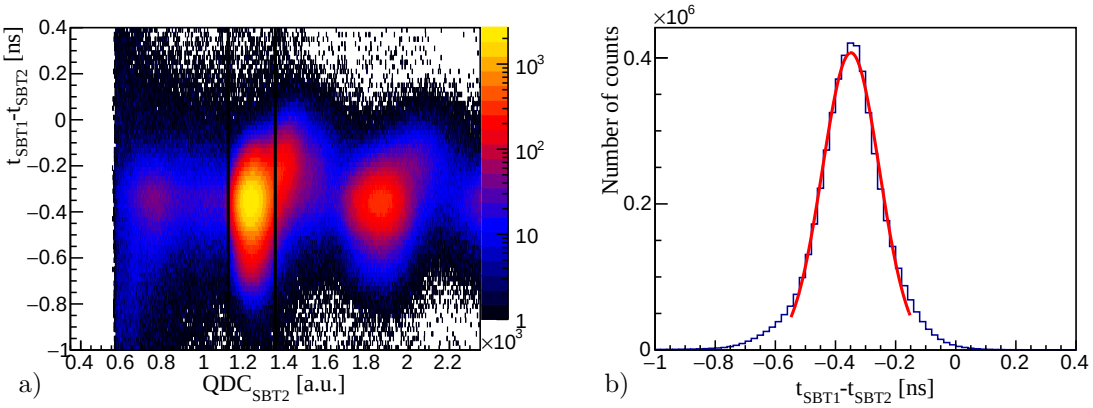

Figure 4.1: The left spectrum a) shows the time difference between the SBTs plotted with respect to the mean charge of SBT2. Three circular maximum at QDC_{SBT2}=750, 1250 and 1850 with the same mean value for the time difference Δt indicate different elements stemming from the beam accelerator. The highest number of events is in the middle maximum which contains the events of the primary ^{16}O beam. The fit on the y-projection of this region (see b)) gives the time resolution of the beam trigger.

The preliminary time resolution σ^{SBT} of the beam trigger is obtained from figure 4.1 b) where the y-projection of the events inside the black marked gate in a) forms a Gaussian shape in the central part with a width of $\sigma^{SBT} = 95\,\text{ps}$.

The uncertainties of the two detectors enter into the resolution independently. Assuming the TOF resolution being determined by the rising edge of the photon signal and its corresponding signal to noise, the resolution of each SBT detector becomes better by $\sqrt{2}$ to

$$\sigma^{SBT} = 67\,\text{ps}. \tag{4.4}$$

Hence, the resolution is within the requirements (see equation (2.10)).

4.2 Beam Drift Chamber

The beam particle position on the target in horizontal (x-axis) and vertical (y-axis) direction is determined by the beam drift chamber (BDC) upstream. When the beam particles pass the chamber volume, the gas ionizes and a tray of electron avalanches are formed. The electro-static forces ensure an almost uniform velocity of the electrons to the anode wires where their signals are recorded.

The BDC works in common-stop-mode, i.e., the beam trigger stops the time period started with the wire signal for each channel [72]. Thus, small absolute drift times correspond to larger distances from the wire. During the calibration runs, a defocused beam with 17 kpps covered the full active area of the central detector cell. The spectrum in figure 4.2 a) shows the distribution of all events for the raw drift times in the horizontal wire planes. The vertical markers define

the borders of the drift chamber cell where the left line marks the half of the drift length, in our case 9 mm and the largest drift times correspond to hits on the anodes. Due to a slightly varying electric field inside the cells the drift time is position dependent and the distribution in the histograms is not flat.

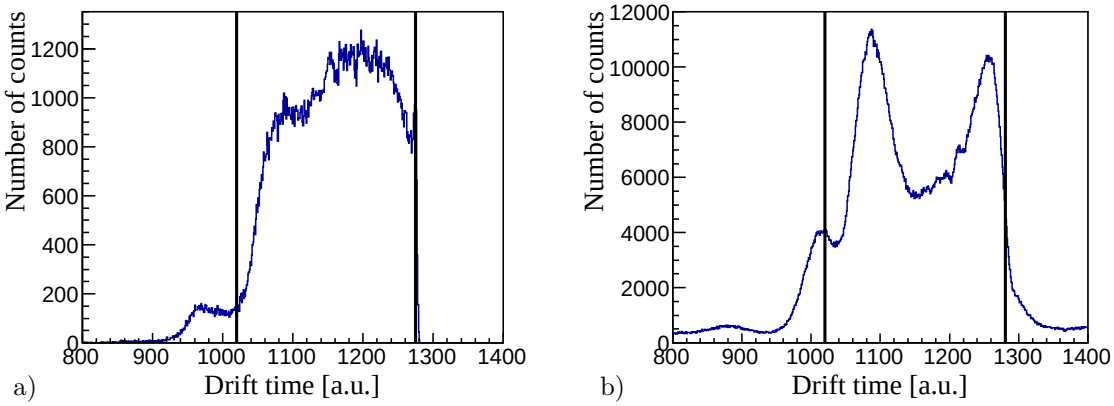

Figure 4.2: The drift time of the y-axis with the markers for the drift cell borders in the case of defocused beam spot size and low intensity (in a)) and in the case of a narrow beam spot and high intensity in the the experimental runs (in b)). In the common-stop mode small absolute values of the drift time correspond to large drift time. Events outside the borders belong to particle hits between two neighboring cells in the low field region and are rejected.

The analysis is based on the PC code *ianalys* of T. Kobayashi[2]. Underlying the conversion function from the drift time to drift length is the assumption of equally spread events over the whole cell, i.e., the number of counts in figure 4.2 a) needs to be distributed equally along the drift length. Starting from a linear fit function and successive improvements by adding higher degrees of polynomials, the drift length is varied in such a way that the events are distributed evenly over the length of the cell along the two fixed points (drift time=1275, drift length=0 mm) and (drift time=1020, drift length=±9 mm). Figure 4.3 a) illustrates the procedure in the superimposed horizontal planes in which the drift times are related to drift lengths. The resolution is obtained by tracking four planes onto the fifth plane and subtract the difference between the extrapolated track from the measured one in that plane [73]. The distribution of events along the drift length in figure 4.3 b) shows the distribution of hits along the cell after the applied conversion. Compared to the origin distribution of events according to the drift time in figure 4.2 a) the distribution is more evenly spread along the cell with raise around the anode.

Runs with beam rates of 17, 100, 200 and 400 kpps showed a continuous drop in resolution. Space-charge effects could influence the field in the cells when rates get higher [74]. The derived conversion fit function in the dedicated calibration runs with wide beam are the starting point for the self calibration.

[2]Department of Physics, Tohoku University, Aoba, Sendai 980-8578, Japan

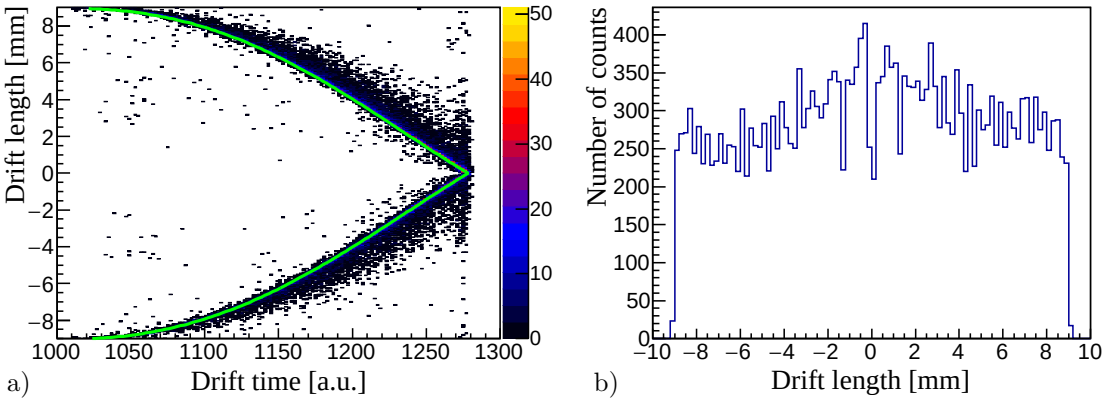

Figure 4.3: a) Principle of calibrating the drift time into the drift length using the conversion function (outlined in green). Instead of a linear correlation between drift length and TDC, it is position-dependent. The events show the assigned drift length for a measured drift time in figure 4.2 a) using the conversion function. In the integration method, the distribution is regarded as evenly spread and the time is superimposed with the matching conversion fit function. The iterative process is finished if the distribution of the events is even along the cell size of 18 mm (see b)).

The experimental runs with narrow beam spot sizes need to serve as reference. The distribution of the drift times inside the black borders is totally different since the cell is not evenly enlightened but only partly (see figure 4.2 b)). Events outside the black borders are assigned to unphysical drift lengths and cause background. The conversion function is slightly adopted such that the residual is minimal (see figures 4.4 a) and c) for the vertically and horizontally tensioned wire planes and the projections over the whole cell in b) and d)). The vertical smooth progression indicates that the arrangement of the wire positions has been well reconstructed. Fitting the center part with the Gaussian function (see figures 4.4 b) and d)), this leads to a beam tracking resolution of

$$\sigma_x^{BDC} = 242\,\mu\text{m} \qquad \text{and} \qquad \sigma_y^{BDC} = 190\,\mu\text{m} \tag{4.5}$$

at the exit window of the chamber. Geometrically extrapolated to the target position it enlarges to a tracking resolution of

$$\sigma_x^{BDCtgt} = 605\,\mu\text{m} \qquad \text{and} \qquad \sigma_y^{BDCtgt} = 475\,\mu\text{m}. \tag{4.6}$$

For a realistic resolution on the target plane scatterings of the projectiles during the flight path from the exit window to the entry window of the target chamber need to be taken into account. Hence an additional uncertainty of

$$\sigma_{Stgg}^{BDC} = 0.19\,\text{mrad} \widehat{=} 112\,\mu\text{m} \tag{4.7}$$

rises which modifies the residuals in equation (4.6) to

$$\begin{aligned} \sigma_x^{'BDCtgt} &= \sqrt{(\sigma_x^{BDCtgt})^2 + (\sigma_{Stgg}^{BDC})^2} = 615\,\mu\text{m} \\ \sigma_y^{'BDCtgt} &= \sqrt{(\sigma_x^{BDCtgt})^2 + (\sigma_{Stgg}^{BDC})^2} = 488\,\mu\text{m}, \end{aligned} \tag{4.8}$$

well below the required value of $\sigma^{'BDCtgt}$=750 µm (see table 2.1).

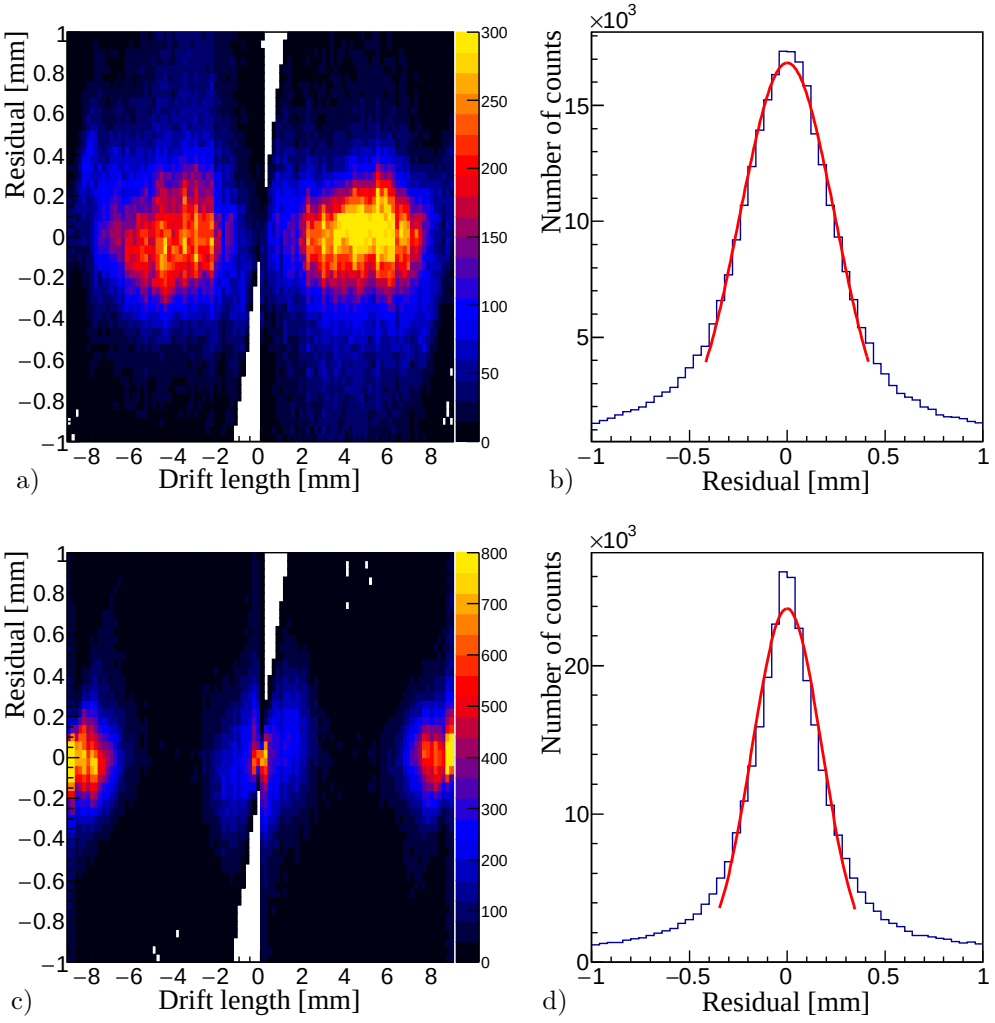

Figure 4.4: Residuals of the BDC in x- and y-direction (see a) and c)) over the 18 mm cell width using the conversion function derived from the self calibration method with the data from the experimental runs. The residual between the extrapolated value and the conversion fit function is almost uniform over the entire drift length. The y-projections in b) and d) show the residuals using Gaussian fit functions. The widths are presented in equation (4.5).

4.3 Hodoscopes

In the two arms of the hodoscope, the flight time of the protons from the reaction points to the TOF detectors are measured to calculate their kinetic energies. In

order to be able to evaluate energies from E_{kin}=80 to 210 MeV, the detectors must determine the times accurately over a length of 6 ns. The individual calibration steps are drawn in the raw spectrum of the QDC values with respect to the TDC channels of detector no. 8 (compare the nomenclature in figure 2.8) (see figure 4.5). The physical content and interpretation will be discussed in section 6.2.

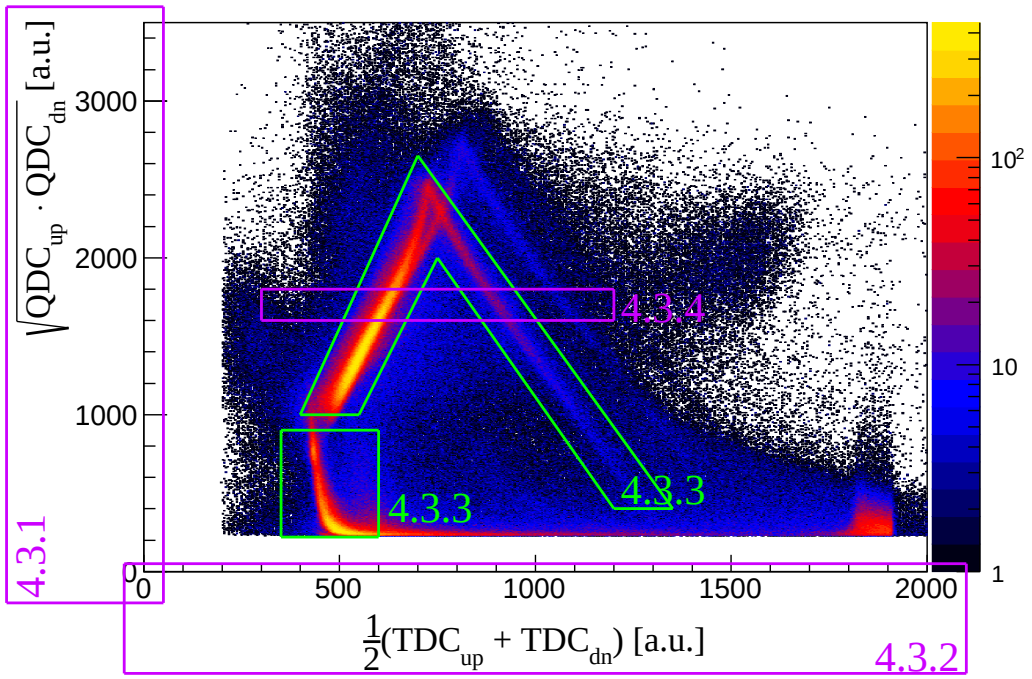

Figure 4.5: Raw spectrum of the mean QDC with respect to the mean TDC values of detector no. 8 (*up* means the upper PMT and *dn* the lower PMT on the vertical edges of the TOF detector). The areas used for the single calibration steps are highlighted by boxes with the associated section number.

The energy calibration relates the deposit charge QDC to the light output (see section 4.3.1). Like for the SBTs, the TDC to time calibration was conducted by the time calibrator (see section 4.3.2) where in this case the large spread of the particles' energies hitting the spatially expanded plastic scintillators needs more detailed studies on the light propagation in the rods depending on the hit position (violet box), discussed in section 4.3.4. Two kinds of slew corrections using different particles lead to an energy loss dependent time correction (see section 4.3.3). The walk correction exploits the constant velocity of photons (lower green box) to straighten the curve there. Quenching effects are sensitive to ions and hence, the proton arm (upper green border) was used to get consistent times for all protons independent of their energy loss.

4.3.1 Light Output Calibration

The PMTs split the signal into two branches. One output branch was directly connected to the QDC module, the second branch is used for the timing informa-

tion and will be discussed from the next subsection on. The signal output Q_{PMT} of the PMT (called light output here) is in first order proportional to the deposit charge of the particles passing through:

$$Q_{PMT} = A \cdot QDC + B. \tag{4.9}$$

The calibration of the QDC in light output of each PMT requires at least two reference points. Randomly triggering the DAQ and sending integration windows to the QDC module determines the pedestal, i.e., Q_{PMT}=0 of the electronics. To align the amplitudes of all PMTs, we used the β- emitter ^{90}Sr which was positioned in the center of each panel and assumed a constant light transport to both PMTs. To consistently read the second calibration point from the continuous energy spectrum of the β-decay particles we choose to take the maximum energy transfer of 2282 keV to the emitted electron and define this value after the plateau has dropped down to a quarter of its height (see figure 4.6).

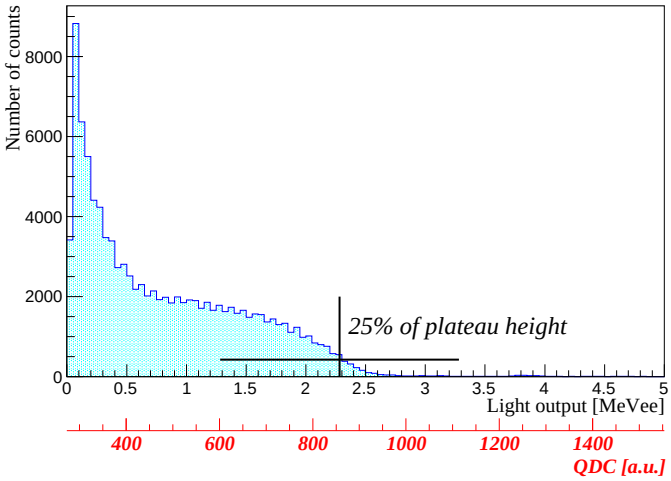

Figure 4.6: Raw QDC channels (in red) and the calibrated light output spectrum (in black) of the calibration runs with electrons from the β^--emitter ^{90}Sr in one TOF detector. The continuous energy spectrum ends at the maximum energy of 2282 keV which is defined as the drop of the plateau to 25% of its height. The source was placed in the center of each TOF detector.

The new scaling is shown in black in the same figure. The resulting light output of one plastic scintillator is given as the arithmetic mean of Q_{PMT1} and Q_{PMT2} in both PMTs [71],

$$\text{Light output} = \sqrt{Q_{PMT1} \cdot Q_{PMT2}}. \tag{4.10}$$

4.3.2 Time Calibration

The time calibration will follow the same procedure in analogy to the SBTs in section 4.1. A channel of the TDC corresponds to an average width of 35 ps.

Alignment of the channel widths is performed by laying the pattern of the time calibrator over the TDC channels and fitting a linear function over nine periods (see figure 4.7 where the x-axis labeled in red shows the TDC channels and the black axis corresponds to the calibrated time).

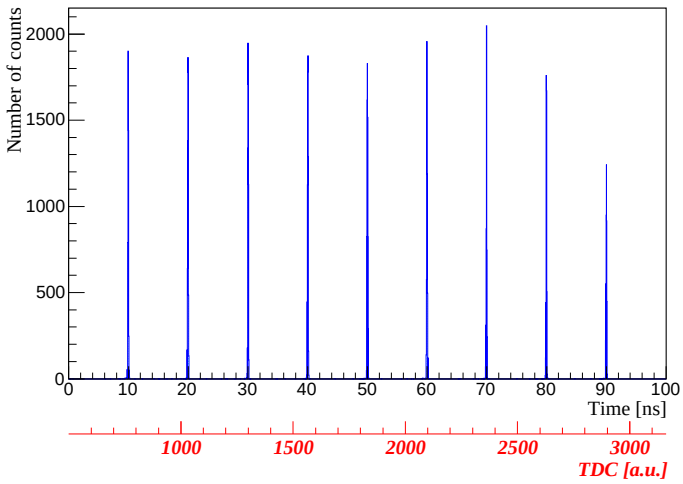

Figure 4.7: Raw TDC channels (in red) and time spectrum (in black) of signals from the time calibrator module Ortec 462. The module provides signals with a period of 10 ns.

In order to refer the times to the origin t_{zero} in the target center, the times in the TOF detectors must be adjusted. The offset is determined by precisely defined time-of-flights of events whose particles provide signals in both the SBTs and the plastic scintillators. We use the time-of-flight of the beam particles to the Fe-degrader and the time-of-flight of the emitted photons there to the scintillators. From the constant velocities of the beam and the photons, it is possible to assign the timing for each panel individually. In order to avoid charge deposit effects a small light output range from 2.0 MeV_{ee} <Light output<2.5 MeV_{ee} at relatively large photon energies was used.

Daily repetitions of the time calibration take into account deviations coming, e.g., from switching on and off the modules and detectors. In the next sections we will see that for various high charge deposits in the scintillator additional time corrections are required.

4.3.3 Walk and Slew Correction

Walk Correction

The timing branch of the PMTs forward the pulse to the leading edge CAMAC discriminator Phillips 7106 [75] where it needs to overcome a certain threshold before it is processed to a logic signal. Since the rise time of the pulse depends on its amplitude the output signal of the discriminator seems to walk for equidistant TOFs. Photons are particularly suitable as correction tool due to their equal

velocity at any energy. Figure 4.8 a) shows the raw light output to time spectrum collected during the experiment with the oxygen beam. The curved shape in the lower energy range up to 3 MeV$_{ee}$ at t ∼9 ns originates from the photons released in the Fe-degrader. Assuming a constant TOF of the beam over the distance from the SBTs to the beam dump all photons from there should appear at the same times in the TOF detectors.

The correction is carried out by drawing a line through the photon curve. The best description is achieved by the equation

$$t_{walk}(Q) = t - (c_0 + \frac{c_1}{\sqrt{Q}} + \frac{c_2}{Q}) \tag{4.11}$$

where $t_{walk}(Q)$ is the new walk corrected time and c_0, c_1 and c_2 are fitting parameters. This formula differs from the well established one like in [76] without the c_2/Q part. Including this term the line was more smooth regarding to higher light outputs where no measurement points existed. The green line in figure 4.8 a) displays the fit function applied in the adjacent spectrum (see figure 4.8 b)). Now, the photons are arranged along a vertical line. For a reasonable fit the formula (4.11) is defined with different parameters for larger and smaller signal amplitudes and connected numerically at the light output of 0.5 MeV$_{ee}$.

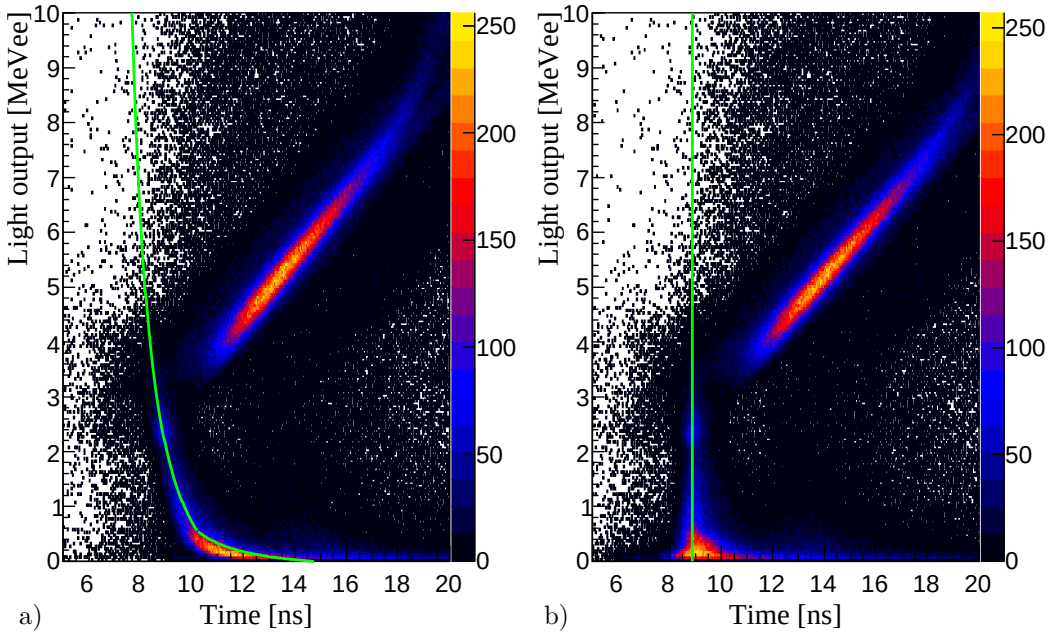

Figure 4.8: The walk correction standardizes the measured time in the PMTs for all signal strengths. The green line in a) is fitted to the photon signals. As they have the same velocity for all energies the QDC depended time was adjusted in order to straighten the green line in b) vertically. For small light outputs $<$ 0.5 MeV$_{ee}$ a steeper fit function is used. The rising correlation occurring from light output ≈4 MeV$_{ee}$ is related to signals from Z=1 isotopes.

A disadvantage of this method is the early end of the measuring points resulting in a wide extrapolation to higher light outputs with increasing uncertainties.

Slew Correction

In addition to the walk correction, which is caused by the signal processing in the back-end electronics, quenching and saturation effects in the plastic material lower the fluorescence which results in a non linear output logic pulse towards the particles' energy losses.

The initial assumption of linear proportionality between the differential energy loss dE/dx of the particles in the plastic scintillators and the released fluorescence dQ/dx (see equation (4.9)) is not fulfilled for low energy particles where the ionization density gets large. Light quenching effects due to saturation effects at high ionization density had been intensively studied in organic scintillators [77]. Semi-empirical formulas take these dependency on ionization strengths into account, e.g. in [78],

$$\frac{dQ}{dx} = \frac{A\frac{dE}{dx}}{1 + B\frac{dE}{dx} + C\left(\frac{dE}{dx}\right)^2} \tag{4.12}$$

where A, B and C are gauging parameters.

The extrapolation curve in the above subsection 4.3.3 can partially be improved by this second correction, the so called slew correction, where two times of the same event with the precise knowledge of one of the two are compared. This case occurs when a particle passes through two adjacent scintillators. They generate light outputs of different magnitudes there but their time-of-flights are mandatorily the same. If one signal is in a region of low energy transfer the implemented walk correction is valid and shifted the time already to its correct position. Signals with high light outputs tend to drift towards positive time differences, i.e., the times are smaller for higher fluorescence (see figure 4.9 a)).

We use a polynomial of second degree,

$$t_{slew}(Q) = t_{walk} - c_1 Q - c_2 Q^2, \tag{4.13}$$

as regression line for each scintillator rod and receive light outputs independent from the TOF differences (see figure 4.9 b)).

The staggered arrangement of the three bundles with three plastic scintillators in the hodoscope arms has the detrimental effect on the correction that only the detectors in each bundle are related to each other. The space gap between the bundles made it unlikely protons to hit two neighboring detectors of two different bundles. This is a matter of improvement in the setup for future experiment and we will come back on this issue in section 7.4.

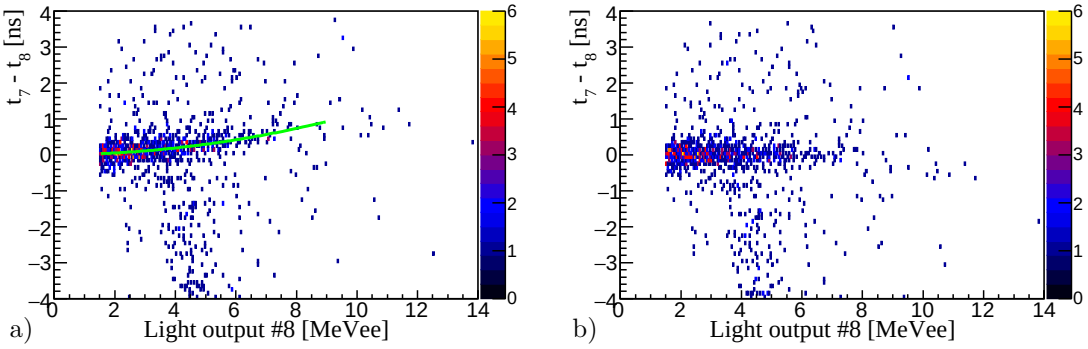

Figure 4.9: Time differences between signals in the two plastic scintillators no. 7 and no. 8 are plotted with respect to the light output of no. 8 under the constraint of signal amplitudes of the neighboring detector no. 7 between 3.0 < light output < 3.5 MeV_{ee} before (see a)) and after the slew correction (see b)). Signals with very low energy below 1 MeV_{ee} are neglected. Without slew correction in a) the time difference increases for higher light outputs in the TOF detector no. 8. The time independence is obtained by corrections with fit functions using polynomial of 2nd degree (green line).

4.3.4 Hit Position dependent Light Accumulation

So far unconsidered remained time fluctuations of signals stemming from different hit positions along the plastic scintillator rod. To visualize the situation, the left 3D-sketch in figure 4.10 illustrates the case where one particle hits the panel in the upper quarter. The emission of photons is isotropic into all directions but many reflections on the surface (specular reflector material was used) spreads the fluorescence intensity considerably and the collecting duration in the PMTs prolong [77]. The closer PMT gains higher pulse shape due to the larger direct light cone which results in a earlier logic signal assigned by the discriminator.

This can be nicely seen by plotting the time difference between the times of the two PMTs with respect to the mean time. Since the time difference, which is proportional to the hit position, also depends on the light output, we divide the light output into slices of 0.5 MeV_{ee} thickness. In order to clean the spectrum a gate is also set on the proton arm (compare the violet bar for the slices and the green upper border for the proton arm in figure 4.5).

Small time-of-flights on the left side of figure 4.10 a) correspond to fast protons which lose only a fraction of their kinetic energies whereas slow protons with large time-of-flights on the right side are stopped in the plastic. The spectrum shows the bending of the mean time by the magnitude of the time difference between the two PMTs. The larger the time difference is, i.e., the closer the hit takes places to the end of the scintillator bar, the more the mean time is deflected from the vertical line. The different shapes of the two green quadratic fit functions indicate a further, disregarded mechanism that differentiates between passing and stopped particles. In the corrected spectrum only at the outermost edges a slight correlation between the time-of-flights and the time difference remains,

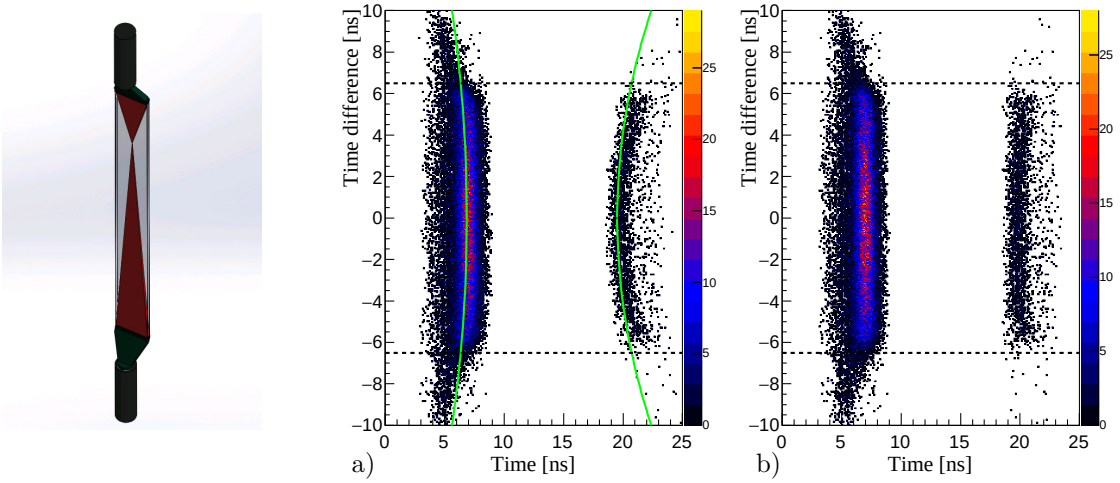

Figure 4.10: On the left side the different solid angles are sketched for a very asymmetric hit position of the particle. On the right side two 2D spectra of the time difference between the two PMTs in one plastic scintillator are shown. The dashed black lines define the borders of the plastic scintillator rod. Before the correction (see a)) the time is bent with increasing time differences. Applying the green marked fit function in the left spectrum b) the dependency vanishes.

while over the largest region a vertical line proves the independence (see figure 4.10 b)).

4.3.5 TOF Resolution

The TOF resolution is determined by the straggling of the proton TOF in two neighboring detectors where the particles punched through (see figure 4.11 which shows the y-projection of figure 4.9). Forward-directed TOF detectors (like TOF detectors no. 7 and no. 8) provide statistics in the order of > 100 events. Detectors at larger horizontal angles with respect to the beam-direction have much less events of few dozens and in the case of four TOF detectors it was not possible to specify a reasonable value. Averaged over the remaining detectors, the value for the time resolution is determined to

$$\sigma_{\Delta}^{TOF} = 246\,\text{ps}. \tag{4.14}$$

The value needs to be adapted to the resolution for one TOF detector each, i.e., the doubled included time resolutions of the two TOF detectors is taken into account by dividing σ_{Δ}^{TOF} by $\sqrt{2}$ (compare section 4.1). Since the particles loose their energies on both plastic scintillators the light output is on average split into

the two adjacent scintillator panels. At half of the light output the resolution decreases by an additional factor of $\sqrt{2}$. In total the TOF resolution is

$$\sigma^{TOF} = \frac{1}{\sqrt{2}}\frac{1}{\sqrt{2}}\sigma_{\Delta}^{TOF} = 123\,\text{ps}. \tag{4.15}$$

In the formalism of equation (2.9) the average TOF resolution for protons with $80 < E_{kin} < 210\,\text{MeV}$ is $\sigma(\frac{\sigma^{TOF}}{TOF}) \approx 1.0\,\%$.

This corresponds to a proton energy resolution of

$$\sigma(\frac{\sigma^{E_p}}{E_p}) = 2.4\,\% \tag{4.16}$$

as it was required in the goals (see equation (2.1)).

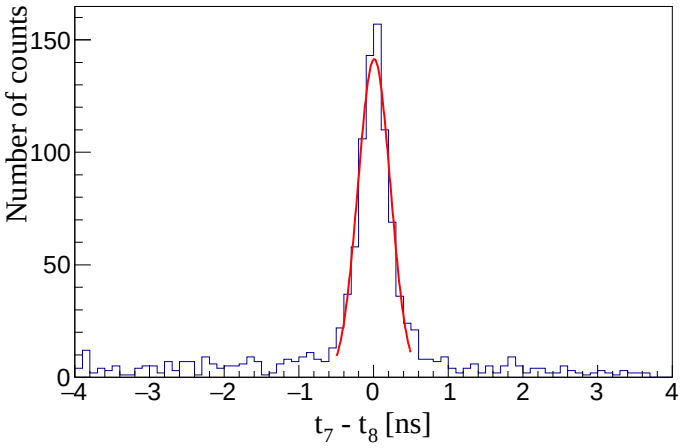

Figure 4.11: Time difference spectrum between ions penetrating both TOF detectors no. 7 and no. 8. Because of the small probability for particles to hit the border between two panels a small contamination of random background could not be avoided.

Beside partly poor statistics in the slew correction, further misalignments in terms of the correct offset and walk corrections remain. Using the physical constraints on the excitation energy spectrum in section 6.6 small local offsets in the order of few 100 ps for each TOF detector had to be added or subtracted. We could also observe an underestimated walk correction for fast protons which was partially fixed by a regression line for proton energies $E_{kin} > 145\,\text{MeV}$ globally set for all TOF detectors (see section A.1.1). Since the TOF calibration is essential for the analysis we discuss necessary changes in-depth in section 7.4.3.

4.4 Silicon Tracker

The silicon tracker with its two arms of three layers of silicon detectors is the heart of the setup. With help of the energy calibration we show that, despite the low energy losses of the protons in the wafer, the signal amplitude is sufficient

high to distinguish the smallest occurring energy losses of protons from the noise level.

For low kinetic energies there is a steep slope of the energy loss which flattens at higher energies and approaches slightly to a minimum around E_{loss}=50 keV (see the simulation in figure 4.12 a)). Due to multiple scattering and the interaction statistics the distribution in a thin layer of material discussed here is still not very narrow and follows a Landau distribution and some protons deposit significantly more charge and are found far above the average energy loss. A similar picture can be discerned in figure 4.12 b) where the experimental uncalibrated ADC channels in the exemplary silicon detector D1 are plotted with respect to the particles' kinetic energies, determined by the TOF detectors.

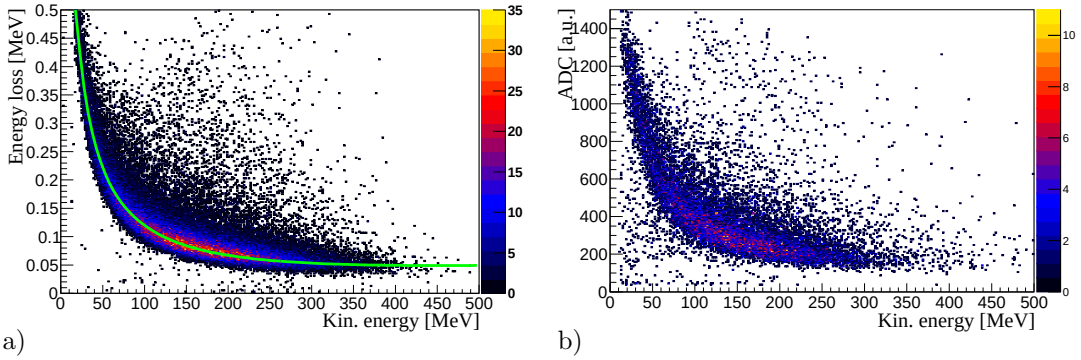

a) b)

Figure 4.12: Geant4 simulation of the energy loss of protons in 100 µm thick silicon wafer with the green fit function along the maximum (see a)). The experimental data with uncalibrated ADC values of silicon detector D1 is shown in b).

The green marked fit function in figure 4.12 a) follows the structure of the Bethe-Bloch-formula for high energies,

$$E_{loss}(E_{kin}) = c_1 + c_2 \cdot \log(c_3 \cdot E_{kin}) + \frac{c_4}{\sqrt{E_{kin}}} \tag{4.17}$$

with c_1 to c_4 as fit parameters, and assigns a certain energy loss value to each kinetic energy. This results in a linear correlation between the ADC values and the energy loss (see figure 4.13 a)) for the same kinetic energies. The ADC values in figure 4.12 b) are finally replaced by the deposit charge equivalent energy loss of protons in figure 4.13 b).

In comparison to figure 4.12 a) the deposit energies in figure 4.13 b) show a broader distribution. In the range from E_{kin}=180-220 MeV the FWHM increases from the simulated value of

$$FWHM_{sim}^{Eloss} = 30\,\text{keV} \tag{4.18}$$

to

$$FWHM_{exp}^{Eloss} = 33\,\text{keV}. \tag{4.19}$$

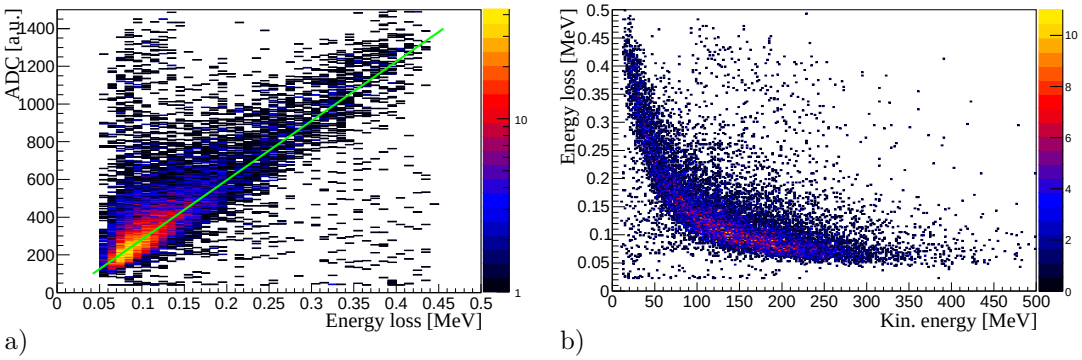

a) b)

Figure 4.13: The experimental ADC values (see figure 4.12 b)) are plotted with respect to the simulated energy losses (see figure 4.12 a)) at the same kinetic energies. The linear energy calibration function is marked in green. The left spectrum b) shows figure 4.12 b) with the calibrated y-axis.

Because of the low number of events in the single channels we refrained from individual energy calibrations and thus the summed spectrum includes the spread of the channels.

The energy loss signals are well above the noise level which was cut below $E_{loss} \approx 20\,\text{keV}$ by the software. The clear distinction from the internal noise of the wafer and ASIC-chips results also in a low multiplicity (see section A.4.3).

4.5 PID Detector Array

The purpose of the PID detector array is to identify the reaction elements by their characteristic energy losses. The stack of four plastic scintillators is calibrated by two data points using the primary ^{16}O beam at the initial energy of 284.2 MeV/u and the reduced energy, after passing a 14 mm thick Fe-degrader in front of the array. The thickness of the beam dump was reduced such that the ^{16}O beam passes it and is stopped in the first detector with a distinct energy. From a direct comparison of these two energy loss measurements and simulated energy losses of ΔE=750 MeV (no degrader) and 1400 MeV (14 mm Fe-degrader) a linear calibration is carried out.

Figure 4.14 shows the superimposed red-labeled raw-data QDC-spectrum of the first, most upstream PID detector with and without the iron plate beforehand. The two peaks are used as calibration points for a linear fit function (black axis-labelling) with the resolutions of

$$\sigma_{Eny}^{PID} = 7.5\,\text{MeV} \quad \text{(with no degrader)} \tag{4.20}$$

and

$$\sigma_{Eny}^{PID} = 9.7\,\text{MeV} \quad \text{(with 14 mm Fe-degrader)}. \tag{4.21}$$

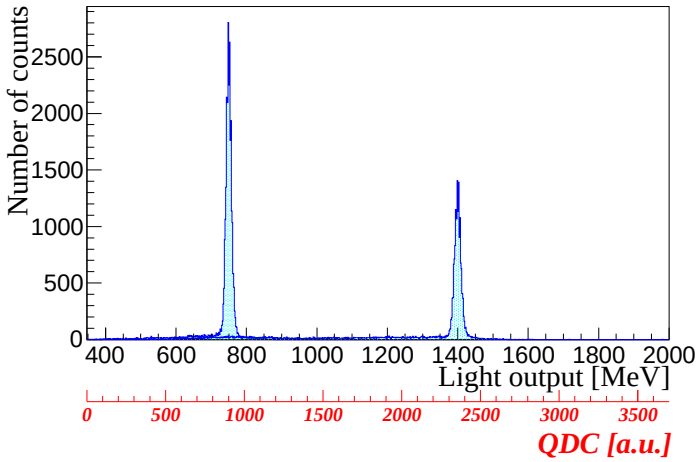

Figure 4.14: *QDC* spectrum (red axis) and calibrated light output spectrum (in black) of the first PID detector. Two runs without and with 14 mm thick Fe-degrader in front of the PID detector array are superimposed. The peaks correspond to the distinct energy losses of the primary ^{16}O beam.

The beam was completely stopped in the first PID detector in the case of the installation of the 14 mm Fe-degrader. There was no time for additional settings to also calibrate the layers 2-4 of the PID detectors. But already the correlation of layer 1 with the other detectors allow proper particle identification using the raw energy loss data (see figure 6.4).

Chapter 5

Vertex Reconstruction Analysis

This chapter will present the procedure to determine the opening angle between the two protons by the vertex reconstruction analysis. Geant4 simulations test the principle approach and specify the expected resolutions (see section 5.1). Thereby we will subdivide the single sources of the angular straggling (see section 5.2) and as a next step the effects of misaligned silicon detector positions will be calculated (see section 5.3). Finally, the experimental data will be used to determine the positions of the silicon detectors to achieve the best vertex reconstruction (see section 5.4).

5.1 Principle of the Vertex Reconstruction

The vertex reconstruction of the reaction point is carried out by the flight directions of the protons through the first two detectors in the x-z-plane while the vertical proton angles are determined from the y-position at target position (provided by the BDC) and from the hit positions in the third layers. Therefore, the local positions in the form of fired strips are converted into the global coordinate system (see the axis labeling e.g. in figure 2.2). Signals from adjacent strips are combined and the energy-weighted position is taken as the actual pass-through position. The horizontal trajectories are extrapolated until the point where they intersect, i.e., this defines the origin of the reaction (compare the first row in the flowchart in figure 5.1).

The method was tested by a Monte-Carlo simulation based on Geant4 using the *QBBC* physics list [79] [80] [81]. There a E_{beam}=290 MeV/u beam of ^{16}O ions passes a target assembly of three plastic foils and two layers of CH_2 wires similar to the arrangement used in the experiment on day 4. Only a few events undergo scattering such that the reaction point is wrongly assigned to take place outside the allowed target planes (see figure 5.2 a)). Most of the proton tracks are projected onto the target foils and fibers (marked in green) and the mean value of the Gaussian fits are located $\delta^T_{syst} \pm 15\,\mu$m within the defined target planes.

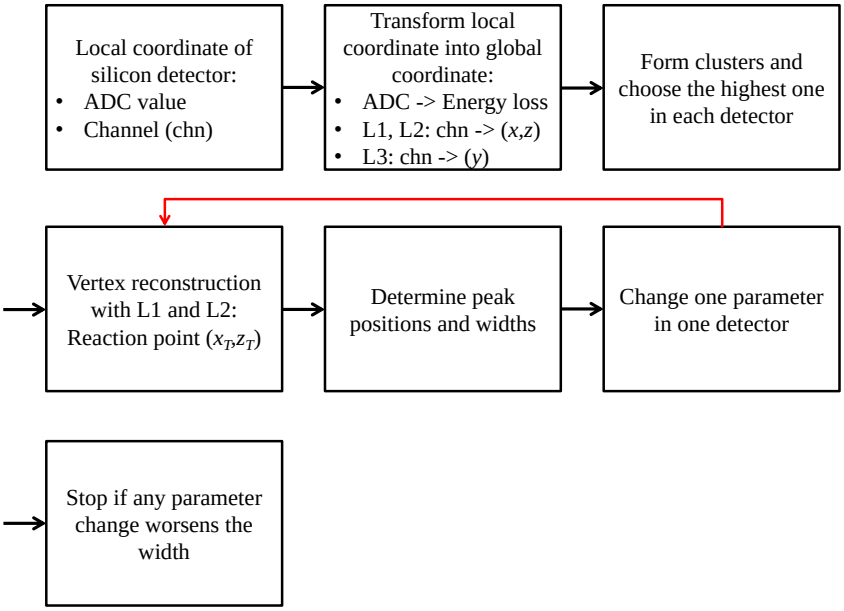

Figure 5.1: Step-by-step procedure of the vertex reconstruction analysis. The first row shows the starting point of the analysis and includes the transformation of the local coordinates of the silicon tracker to the global coordinate system. The next rows illustrate the self-calibration method with repeated detector position changes and their influences on the resolution of the vertex reconstruction.

The width of the vertex reconstruction for the spatial x- and z-directions is Gaussian-distributed (compare figure 5.2 b)) and yields

$$\sigma^{Sili}_{Sim\,min} \sim 180\,\mu\text{m}. \tag{5.1}$$

In the associated third row of table 3.4 upstream targets show a successive broadening of the peaks. This results from additional scatterings in the subsequent foils. In order to compare the resolutions with the experimental data in a convenient way we take the averaged value of the five target planes,

$$\sigma^{Sili}_{Sim\,ave} = 187\,\mu\text{m}. \tag{5.2}$$

The resolution of the vertex reconstruction depends on the angular straggling of the protons but also on the correct positions of the detectors. In the next section the components of angular straggling will be presented. They define the minimum resolution.

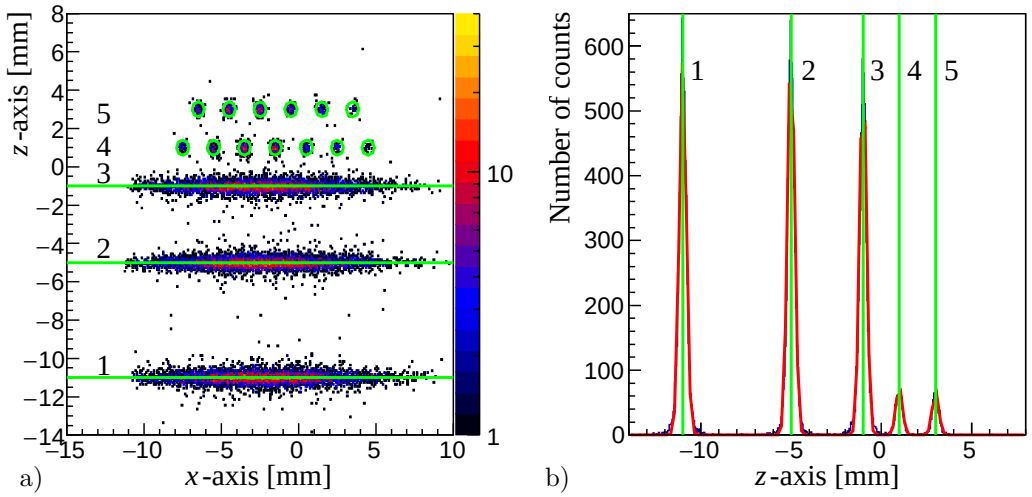

Figure 5.2: Reconstructed vertex positions in the $x-z$-plane (see a)) and along the z-direction (see b)) of $(p, 2p)$ events in the Geant4 simulation. The reconstructed vertex positions are located on the initially set target planes and fibers (green lines and circles). A more detailed examination of the widths of the single peaks in table 3.4 reveals a slight broadening for upstream targets due to additional scattering of the released protons on the subsequent target planes.

5.2 Sources of Angular Straggling

The magnitude of multiple scattering depends on the materials to be passed and on the particle energies. Furthermore, the design of the detector setup had influence on the contribution of the single components of angular straggling. Hence, the presented values must be always seen in context to the specific current $(p, 2p)$ setup.

One source of angular straggling is the target composite. Depending on the material its influence can be dominant (compare the straggling in 100 µm thick polyethylene target foil or in 9 mm thick liquid hydrogen target in table 5.1). Since the detectors are placed outside the target this angular straggling is unavoidable.

Table 5.1: Contributions of the uncertainties of the relevant devices on the opening angle $\sigma(\theta_{op})$ and on the excitation energy σ_{Exc}.

Component	$\sigma(\theta_{op})$ [mrad]	σ_{Exc} [keV]
Target 100 µm CH_2	0.69	249
Target 9 mm LH_2	2.79	846
Silicon det. pitch=100 µm	0.60	196
Silicon det. thickn.=100 µm	1.95	580

The combination of the detector properties and the distribution of the kinetic proton energies results in a lower limit of the precision of the opening angles.

Three properties define the accuracy in the silicon tracker, i.e., multiple scattering in the wafers, the pitch size and the geometrical arrangement.

The pitch size and the geometry define the spatial resolution σ_{int}. To separate the different contributions a first Geant4 simulation was performed assuming infinitely thin detector wafers. Taking into account the origin of reactions in the spatial expanded target assembly and the possible flight directions of the protons the inaccuracy of the vertex reconstruction due to the finite pitch size and the set detector distances is specified to

$$\sigma_{int} = 0.60\,\text{mrad} \tag{5.3}$$

(compare also the theoretical deviation in equation (A.14)). The contribution is small and will be superimposed by even thin targets. The pitch size of 100 µm is hence adequate since smaller pitch sizes would only marginally improve the resolution.

Supplementary scattering processes in the first wafers deflect the particles. Since the degree of deflection depends on the velocities the Geant4 simulation takes the relevant range of $80<E_{kin}<210\,\text{MeV}$ into account which corresponds to the expected proton energies within the detector acceptance. The magnitude of scattering varies from σ_p=2.53 mrad at E_{kin}=80 MeV up to σ_p=1.16 mrad at E_{kin}=210 MeV. The average total scattering over all possible proton energies E_{kin1} and E_{kin2} and their abundances τ is described by the statistical sum of the angular stragglings σ_{p1} and σ_{p2} of two protons in each arm,

$$\sigma_\theta = \int \tau\sqrt{\sigma_{p1}^2 + \sigma_{p2}^2}\,d\tau\,dE_{kin1}\,dE_{kin2} = 1.95\,\text{mrad}. \tag{5.4}$$

In addition to these intrinsic limitations the absolute positions of the silicon detectors are important for the latter analysis. The rest of the chapter therefore deals with the tuning of the silicon tracker position using the experimental data in order to achieve the same average resolution and accuracy for the targets like in the simulation (see equation (5.2)). Subdivided into four groups, they are studied individually in section 5.3.

5.3 Determination of the Silicon Detector Positions

The detector positions can differ from the schematics, e.g., due to a lack of precision in the production or installation. The influence of unidentified systematic offsets on the vertex reconstruction and on the opening angle will be discussed in this section.

The optical measurement defined the detector positions by their angle, distance and shift (see section 3.3). Additionally, twists of the wafer in the detector

plane might have happened. Correspondingly, deviations can be measured relative to these four parameters (see figure 5.3 where horizontal rotations δ_{ang} (red rotation), shifts along (δ_{shift}) and perpendicular (δ_{dist}) to the wafer plane (red arrow and purple arrow) and rotations δ_{yrot} in the detector plane (purple rotation) are illustrated).

Their influences on the resolution σ_{tgt} and position z_{tgt} of the vertex reconstruction will be studied on the basis of figure 5.4 where Geant4 simulations deviate the initial detector positions in many steps. Furthermore, the effects on the opening angle will be calculated taking realistic offset parameters into account (see table 5.2).

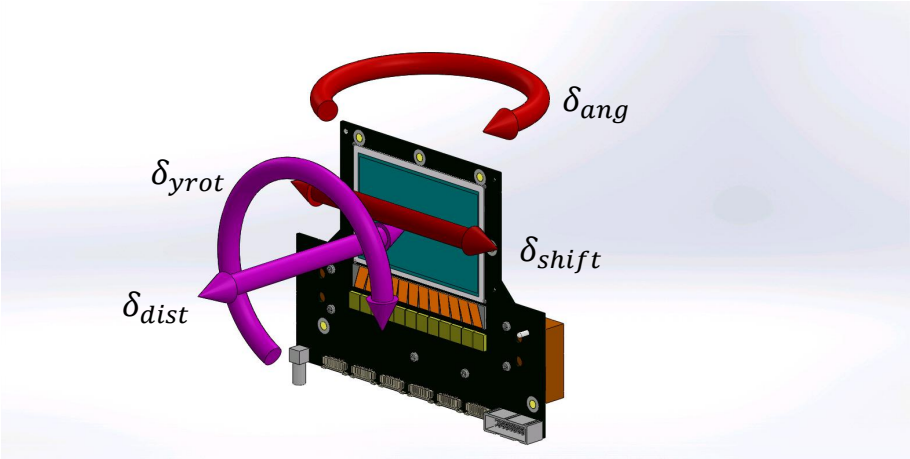

Figure 5.3: Illustration of the undertaken shifts and rotations of the detectors in the first two layers. The simulated deviations δ refer to the center of the silicon wafers.

Rotations of the detector in the x-z-plane shift the reaction points upstream independent of the shift direction δ_{ang}. Smaller angles lead to slight deteriorations of the resolution σ_{tgt} whereas the increase of the resolution is strongest of all shifts at positive δ_{ang} (see figure 5.4 a)). For small δ_{ang} the two branches follow a similar path and hence the influence on the opening angle in table 5.2 is the same.

Horizontal shifts δ_{shift} along the detector surface are hardly recognizable from increased resolutions σ_{tgt} (see figure 5.4 b)). Its effect on the absolute offset Δz_{tgt} is in contrast quite dramatic and the highest one compared to the other displacements. The same behavior is observed for the opening angle. Shifts δ_{shift} add an almost constant angle $\Delta\theta \sim const.$ to the initial angle in the order of $\Delta\theta(\delta_{shift}) \approx 1\,\text{mrad}$ (compare also the geometric deviation in equation (A.16)). The higher resolution $\sigma_\theta(\delta_{shift})$ mainly comes from non-symmetric effects due to the spatial expanded beam spot and the distribution of the simulated QFS $(p, 2p)$ reactions which is not equal around the center of the wafer.

Deviated distances δ_{dist} have the opposite effect like the shifts. While a horizontal shifted detector moves all hits in the same direction, the averaged offsets cancel out (see equation (A.17)). Since the deviation Δz_{tgt} takes place symmet-

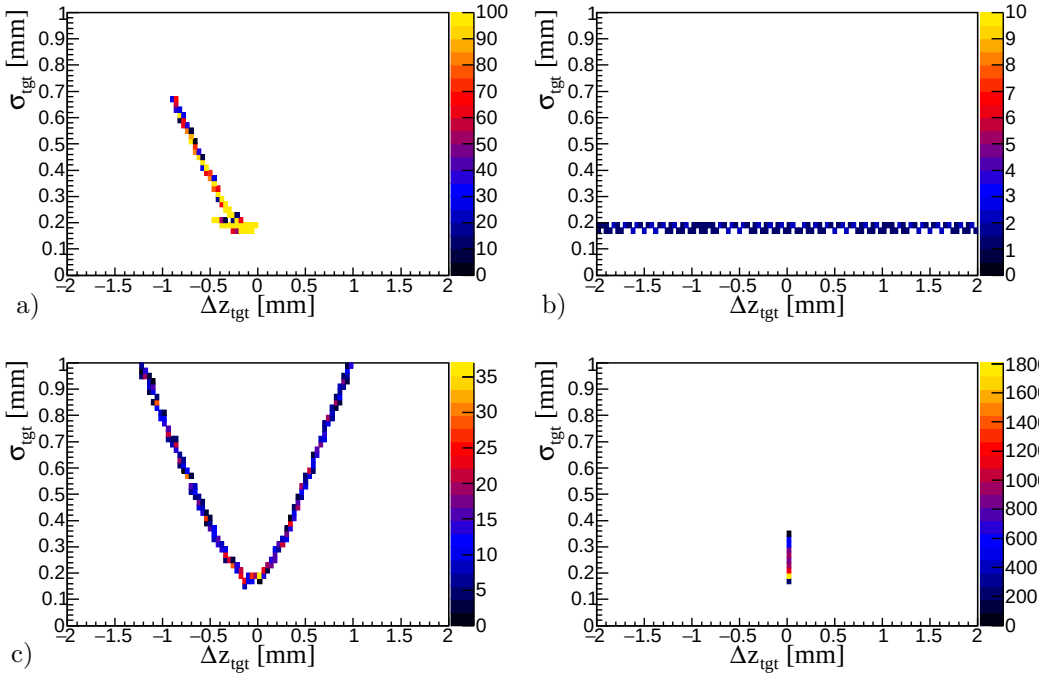

Figure 5.4: Geant4 simulations show the influence of displaced detectors on the vertex reconstruction. Each data point stands for offsets regarding the angle δ_{ang} (see a)), shift δ_{shift} (see b)), distance δ_{dist} (see c)) and the y-rotation δ_{yrot} (see d)). The offsets change the resolution σ_{tgt} of the vertex reconstruction and shift the reaction point, shown here as the difference between the real and reconstructed point in z-direction.

rically in both directions, the resolution σ_{tgt} increases rapidly (see figure 5.4 c)). It causes the largest broadening $\sigma_\theta(\delta_{dist})$ in the exemplary table 5.2.

Planar rotations δ_{yrot} around the wafer center add an horizontal shift to the hit positions. The deviation of the strip positions increases with the vertical distance to the center with changed sign for the two opposite sites above and below the center. Since the distribution of the protons of QFS $(p, 2p)$ reactions is isotropic in the azimuth angle the horizontal shifts σ_{tgt} depend only on the vertical flight directions of the particles but not on the polar angular distribution. Hence, the vertex reconstruction Δz_{tgt} is not affected (see figure 5.4 d)). The influence on the opening angle is therefore rather small (compare table 5.2).

In comparison to the acceptable resolution $\sigma(\Delta\theta_{op})$ (see equation (2.2)) the small broadenings in σ_{tgt} have minor effects and it would not be necessary to determine the silicon detector positions within several hundred µm and we set the requirements of the measurement accuracy of the distance σ_{dist} and angle σ_{ang} to

$$\sigma_{dist} = 200\,\mu\text{m} \quad \text{resp.} \quad \sigma_{ang} = 3.0\,\text{mrad}. \tag{5.5}$$

However, in terms of systematic errors especially *shifts* of the detectors add significant offsets and contribute therefore at most where displaced *angles*, *rotations* and *distances* show much smaller influence on the absolute opening angles.

Table 5.2: Effect of misalignments of the detectors in the layer 1 and 2 with respect to the angle δ_{ang}, horizontal and vertical shifts δ_{shift} and δ_{dist}, and rotations δ_{yrot} of the detectors (compare the nomenclature in figure 5.3). The uncertainties are divided into the systematic shift $\Delta\theta$ and the resolution σ_θ of the opening angle.

Resolution	Layer 1	Layer 2
$\Delta\theta(\delta_{ang} = \pm 0.1\hat{A}^\circ)$ [mrad]	0.05	0.00
$\sigma_\theta(\delta_{ang} = \pm 0.1\hat{A}^\circ)$ [mrad]	0.04	0.03
$\Delta\theta(\delta_{shift} = \pm 100\,\mu m)$ [mrad]	± 0.95	∓ 1.02
$\sigma_\theta(\delta_{shift} = \pm 100\,\mu m)$ [mrad]	0.03	0.03
$\Delta\theta(\delta_{dist} = \pm 100\,\mu m)$ [mrad]	∓ 0.06	± 0.01
$\sigma_\theta(\delta_{dist} = \pm 100\,\mu m)$ [mrad]	0.09	0.08
$\Delta\theta(\delta_{yrot} = \pm 0.1\hat{A}^\circ)$ [mrad]	∓ 0.00	± 0.00
$\sigma_\theta(\delta_{yrot} = \pm 0.1\hat{A}^\circ)$ [mrad]	0.04	0.00

Achieving a better systematic offset than ΔE_{Exc}=0.5 MeV (see equation (1.5)) the horizontal shifts of the four detectors in the first two layers must be determined more precisely than

$$\Delta\theta(\delta_{shift}) < 1.8\,\text{mrad} \quad \text{resp.} \quad \delta_{shift} < 180\,\mu m. \tag{5.6}$$

For each silicon detector this means an average precision of

$$\sigma_{shift} = 100\,\mu m. \tag{5.7}$$

The detector positioning using the optical measurement was not precise enough to achieve this goal (see equation (3.4) for one detector). It was therefore necessary to develop a new method, the so called self-calibration analysis.

5.4 Self-Calibration Analysis

Misalignments lead to systematic offsets in the determination of the opening angles which are strongly connected to the resolution and offset of the excitation energies. In this section we show a new developed method to find the correct detector positions. Section 3.4 explained the special features of the target design to verify the position of the silicon tracker where the fibers and the target foils serve as references to find the best arrangement. The detector placements are then considered correct as soon as the resolution of the vertex reconstruction reaches a minimum and the relative distances of the target stacks correspond to those from the mechanical measurements.

From the preliminary consideration about the influence of the single misalignments we can neglect the *angle* rotation around 42Â° since its effect on the opening angle is marginal within small rotations. For now, likewise ignored is the

rotational y-dependence which adds a common width. So the number of free parameters for the four detectors reduces by 6 from 14 to 8, i.e., changes in the *shift* and *distance* parameters remain.

In order to find the best detector positions any reaction can be used as long as particles are detected in the two arms of the silicon tracker. The method is hence not restricted to QFS $(p, 2p)$ reactions. The starting point are the detector positions of the schematic drawing. The next steps are illustrated in the second row in the chart flow of figure 5.1. The peak positions and widths of the reconstructed reaction points are determined (compare the Gaussian fits in figure 5.2 of the Geant4 simulation) and stored. Successively the parameters $shift$ and *distance* are varied in each detector one by one. The best vertex reconstruction is found if the spaces between the peaks correspond to the distances of the target foils (equivalent to Δz_{tgt}) and the resolution σ_{tgt} is minimum. The analysis was performed in steps of 50 µm which is also seen as the accuracy of the self calibration σ^{SC}.

Necessary movements of the detectors are listed in table 3.1. Improvements of the vertex reconstruction concerning the widths of the peaks are achieved by displacements in the *distance* of $\pm\,0.2$ mm and *shifts* of the detectors 1-3 to the right and detector 4 to the left.

In comparison to the optical measurements (see section 3.3) the detector positions differ marginal. The shifts of the second and third detector are 0.15 mm and in good agreement with the values from the photographic analysis. However, the smaller shifts of the detectors 1 and 4 are in opposite direction. The difference is 0.11 mm for the first and 0.07 mm for the fourth detector. No agreement can be found in the shifts of the *distances*. This might be due to the difficult position of the zero of the coordinate system in the photogrammetry system whereas the shifts depend only on the angles and the markers on the detectors. They are less affected by the dedicated coordinate system.

Figures 5.5 a) and b) show the associated vertex reconstruction with three planes and accumulated events at fixed intervals (i.e., the fiber targets). The averaged resolution of the peaks is obtained to

$$\sigma^{SC} = 195\,\mu\text{m} \tag{5.8}$$

which is equivalent to the resolution of the opening angle,

$$\sigma_\theta = 2.7\,\text{mrad}. \tag{5.9}$$

Some events are outside the physical possible reaction surfaces. The green lines and circles represent the target positions determined by the optical measurement (see section 3.4). The x-positions of the fibers could not be measured and the design values are used. The reconstructed vertices exhibit an offset of 0.85 mm downstream with respect to the absolute target measurement. The distances

between the single stacks (compare table 3.4, last row), however, are in perfect accordance.

The reason for the large systematic shift between the directly measured absolute target position and the reconstructed target position is unclear. The later reconstruction of the excitation energy spectrum will show that the detector positions determined by the self-calibration leads to positions of the excited states within the acceptable tolerances. An offset of Δz=0.6 mm also remains if the detector positions of the optical measurements were used instead (see table 3.4, fifth row "Tracker").

A blind spot in the photogrammetry analysis was the freely selectable coordinate system to which the detectors and the target holder structure refer. A misidentified user-selected center position would shift all devices. An unrecoverable offset could have moved the coordinate system almost one millimeter downstream.

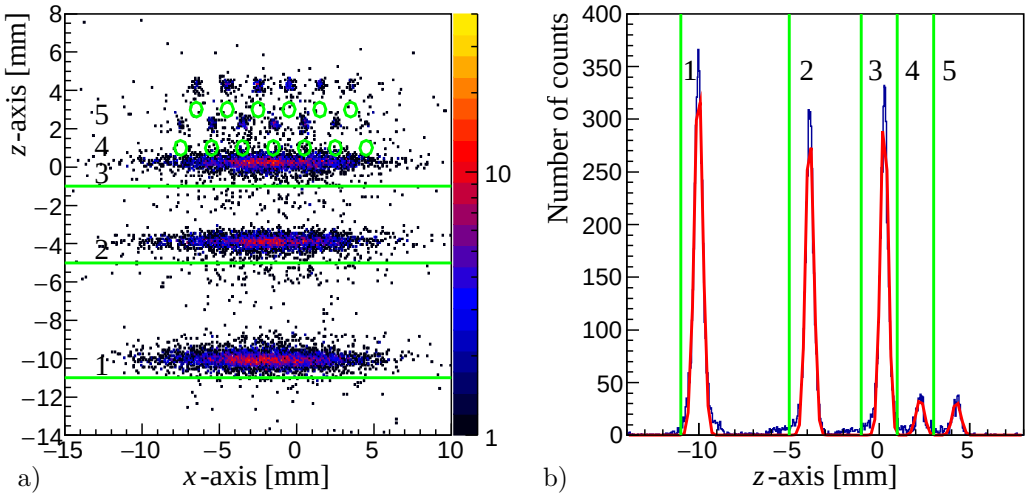

Figure 5.5: Reaction points reconstructed with two emitted particles detected each in one arm of the silicon tracker. In a) and b) the vertex reconstruction using the silicon detector positions from the self-calibration are shown in the x-z-plane and in the z-direction. The green lines and circles represent the measured absolute target positions.

With the granular target design, the silicon tracker could be tuned to the correct position and the goals of the resolution of the vertex reconstruction (see table 2.1) were reached. The experimental situation will change if a thick liquid hydrogen target will be installed instead of polyethylene foils. A workaround in order to continue using the self-calibration method is described in section 7.4 where small changes of the setup would still allow its use.

Chapter 6

Data Analysis

In this chapter we discuss the elaborated missing mass method by using the new setup in order to reconstruct the excitation spectrum of the QFS $^{16}\mathrm{O}(p,2p)^{15}\mathrm{N}$ reaction with the required resolution. After the calibration and the detector positions were determined, preparatory work is still necessary which comprises the identification of the beam particles, the extraction of $(p,2p)$ events and the massive suppression of background.

6.1 Beam Profile

The trajectories of the beam particles are provided by the BDC. From the extrapolation of the plane of the BDC to the target planes the vertical position of the reaction point is derived. Together with the vertical hit positions in the third layers of the silicon tracker the flight direction of the protons in the y-z-plane is determined.

The projected beam profile onto the target foils shows a well focused shape around (x^{Beam}, y^{Beam})=(-1.7 mm, -0.3 mm) (see figure 6.1 a)). The projections in the x- and y-direction are each Gaussian-shaped (compare figures 6.1 c) and d)) with widths determined to (σ_x^{Beam},σ_y^{Beam}) =(3.7 mm, 2.3 mm). Bands with the size of the beam spot can be explained by the correct beam position measured in one direction but wrong reconstruction in the perpendicular direction caused by pile up signals. The sharp shape in the form of a cross indicates independent occurring errors due to different drift times in the x- and y-axes.

Redundant information is a helpful tool to remove defective events. The silicon tracker determines the origin of the two emitted particles in the x- and z-direction and a comparison between the two reconstruction mechanisms in the x-direction checks the consistency of the results and is therefore a suitable tool to exclude inconsistent events. The difference $x_{BDC} - x_T$ between the two vertex reconstruction methods using the BDC and the silicon tracker reveals an almost position independent congruence (compare the horizontal distribution around $x_{BDC} - x_T$=0 in figure 6.2 a)). Small deviations around the edges of the BDC

cell at ±9 mm indicate limited accuracy of the BDC calibration (see section 4.2). Since the calibration of the BDC was sensitive and dependent on the beam intensity fluctuations during the experiment could cause the charge dependent drift time changes and pile ups. The pattern in the two perpendicular diagonals are self correlations of the BDC totally uncorrelated to the measurements with the silicon tracker.

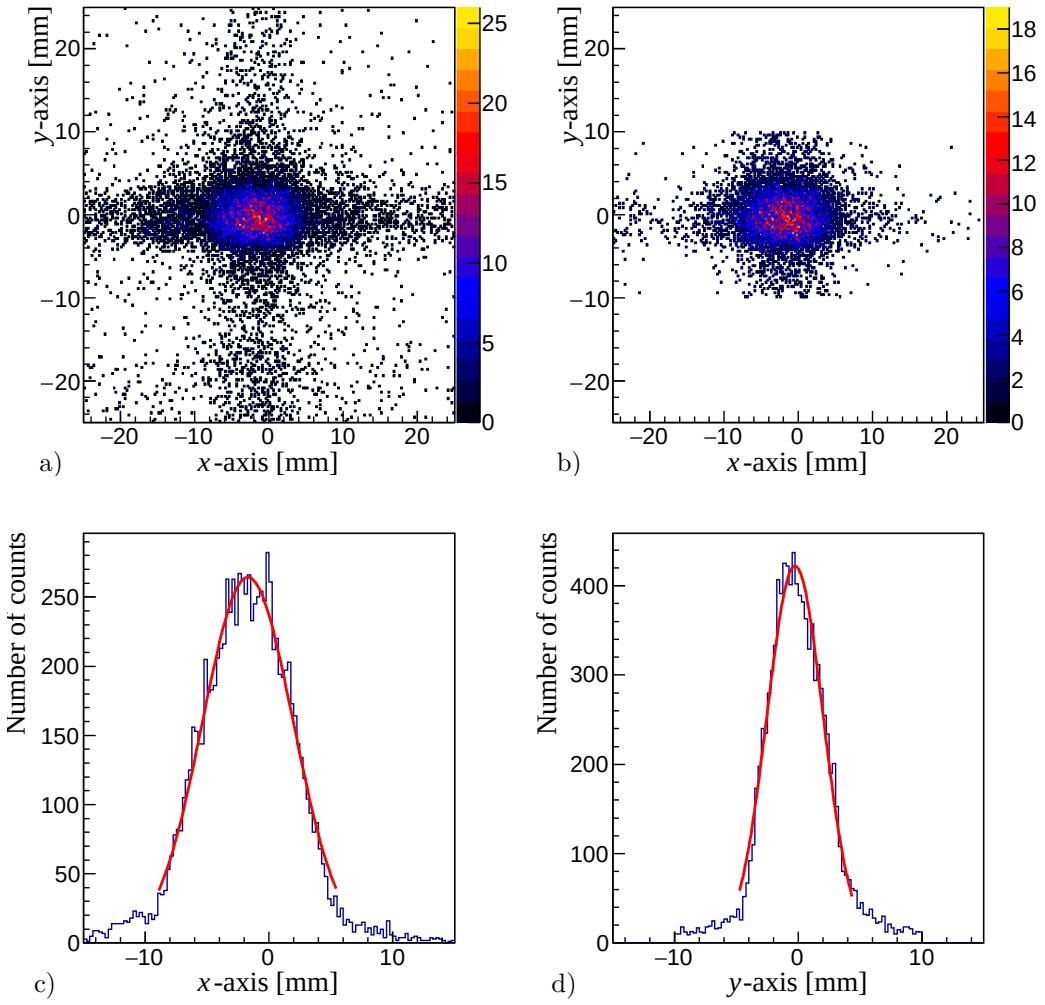

Figure 6.1: Gaussian shaped beam profile on target position reconstructed by the BDC (see a)). Unphysical horizontal and vertical bands along the beam spot size indicate rare problems in the reconstruction procedure. The horizontal line in a) vanishes if consistent target x-positions of the reconstructions by the BDC and the silicon tracker are requested (see the green gate in figure 6.2 a) with a vertex difference of $|x_{BDC} - x_{TGT}| < 5\sigma$). Here, the vertical line is cut to ±10 mm for symmetry reasons. The beam profiles in x- and y-direction show Gaussian distributions in c) and d).

The width of the distribution in the y-projection in figure 6.2 b) is

$$\sigma_{exp}^{x_{BDC}-x_T} = 697\,\mu\text{m} \tag{6.1}$$

and corresponds to the expectations (see equations (5.8) and (4.8))

$$\sigma_{theo}^{x_{BDC}-x_T} = \frac{1}{\sqrt{2}}\sqrt{(\sigma''^{BDCtgt})^2 + (\sigma^{SC})^2} = 645\,\mu\text{m}. \tag{6.2}$$

Consistent events within $|x_{BDC} - x_T| < 5\sigma$ are marked in figure 6.2 a) (see the green borders). Applying this gate on the beam profile the horizontal tails vanish in figure 6.1 b). They are not confirmed by the vertex reconstruction. Although we have no accurate opportunity to test the vertical band with redundant information we conclude that these events are corrupt, too, and cut the spectrum for events $|y_{BDC}| > 10\,\text{mm}$.

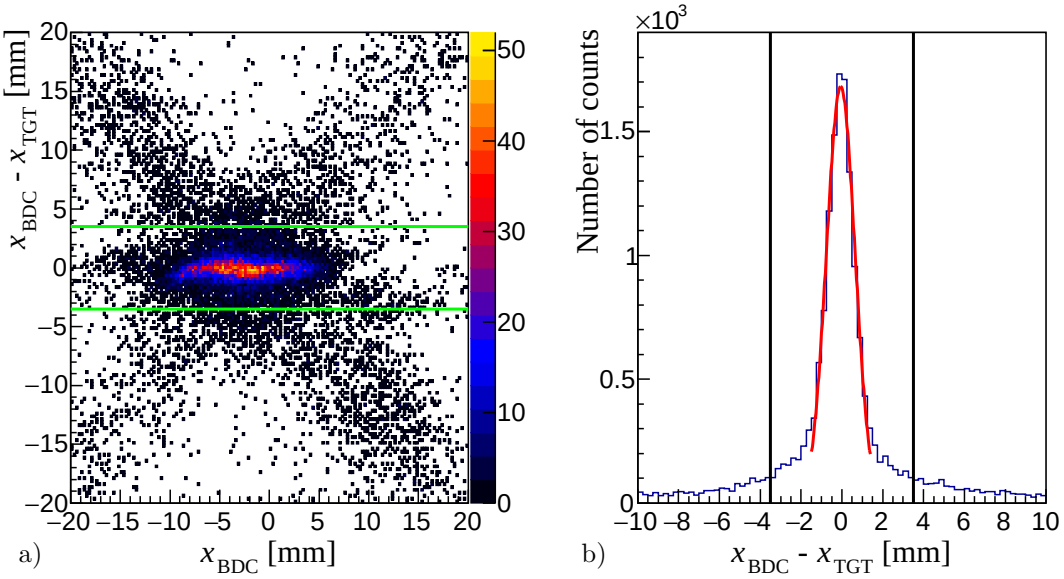

Figure 6.2: Difference of the two reconstructed x-positions of the beam by the BDC and the silicon tracker with respect to the target x-position using the BDC in a) and the y-projection in b). In order to rely on consistent reaction points we select the events inside borders in green.

In the appendix A.3.2 this kind of exclusion of events by redundant information is applied to other detectors, too. Such gates select events whose signals could be processed correctly. They are not sensitive to any reaction channel and hence in the following sections, cuts and gates are set on the characteristic properties of the QFS $(p, 2p)$ reactions to minimize the background from different physical reactions.

6.2 Identification of Protons

The identification of the protons is conducted by the hodoscope arms which provide both the TOF and the light output whereby the velocity β is defined as

$$\beta = \frac{v}{c} = \frac{s}{c \cdot TOF} \tag{6.3}$$

with c as the speed of light and s is the flight distance to the TOF detectors. The horizontal flight distance is taken as the distance between the centers of the target and the TOF detectors and the time differences between the upper and lower PMTs of the TOF detectors determines the vertical y-position.

The light output in the plastic scintillators depends on the ion charge Z and the particle velocity β. In figure 6.3 the β- vs- light output spectrum is shown for the exemplary plastic scintillator no. 8. On the left side three rising curves exist with turning points at $\beta_t = 0.19$, $\beta_d = 0.21$ and $\beta_p = 0.25$. They correspond to the particles (from left to right) triton, deuteron and proton. In that region the charged particles are fully stopped by Coulomb interactions and release their total kinetic energies.

As soon as the velocities are sufficiently high, the hydrogen isotopes punch through the material and store only a part of their energy resulting in reduced light outputs and the three subsequent falling correlations merge together and cannot be separated anymore.

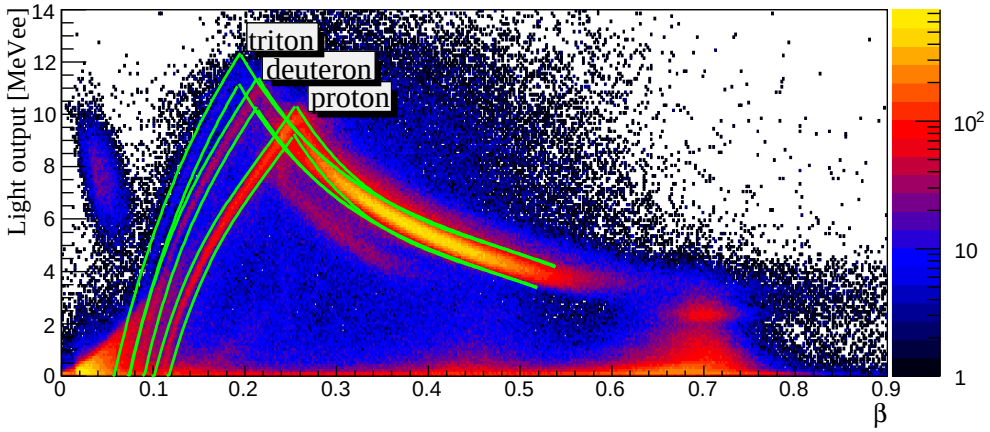

Figure 6.3: Light output with respect to the particle velocities β in the TOF detector no. 8. The green outlined areas correspond to the expected light output patterns of the three particles proton, deuteron and triton. For the further analysis the proton strand is selected.

Signals close to the threshold along the x-axis stem from free neutrons. Their scattering cross sections are typically much lower and the light output consequently decreases. The photon signals were released in the Fe-degrader 80 cm downstream and hence their distances to this plastic scintillator are closer than it was used in the calculation and the velocities are wrongly assigned to around $\beta \sim 0.7$. The falling correlation to the left of the hydrogen isotopes around ($\beta \sim 0.05$, light output $\sim 7.5\,\mathrm{MeV}_{ee}$) are artifacts in the data recording and do not have a physical meaning here.

In the analysis we set a gate on the proton arm. For high energy protons, i.e., for large $\beta > \beta_p$, contamination with deuterons and tritons cannot be inhibited. Their contribution is estimated from the ratio $\epsilon_{d\&t}$ in the increasing correlation

for low kinetic energies between the number of protons n_p, deuterons n_d and tritons n_t :

$$\epsilon_{d\&t} = \frac{n_d + n_t}{n_p + n_d + n_t} = 30.2\ (0.1)\%. \tag{6.4}$$

Their contributions on the background in the excitation energy spectrum however seems to be very low since the background will vanish almost completely (see section 6.6). The later set gates probably are more sensitive to protons than in this identification procedure.

6.3 Identification of Residue Nuclei

Using a polyethylene composite target the QFS reaction $^{16}\mathrm{O}(p, 2p)^{15}\mathrm{N}$ covers only a few percent of the total interaction cross section. Dominating reaction channels like fragmentation, spallation and inelastic scattering can also produce protons in the exit channels, recorded as strong background source in the data. A by advantage of inverse kinematics experiments is provided by the forward focusing of heavy reaction residues close to beam velocity. With the PID detectors (see section 2.2.5) we were able to select the generated elements from the different energy loss patterns and by this the data sample was cleaned up significantly.

Furthermore, the kinematics of the residues varies for the different types of scatterings and especially the additional Coulomb interaction at reactions on the carbon targets deflect the residues from the initial beam direction. This reduces the probability of detections by the PID detector array which has a narrow acceptance polar angle of 0.05Â°.

In order to mark the residue $^{15}\mathrm{N}$ we identify the individual elements in the four layers of the PID detector array by comparing the signal amplitudes to calculations (see table 2.4). All triggered events were used without limitations on proton tracks in the two arms. Most of the measured signals stem from fragmentations of the primary beam in the Fe-degrader. Their kinetic energies are continuous and we can therefore follow the element-specific energy loss patterns in each PID detector.

In figure 6.4 a) and its y-projection in b) the energy signal correlation between events in the first two PID detectors are shown. As the residual $^{15}\mathrm{N}$ is expected to be stopped within these detectors an additional energy threshold for the successive layers was used to veto lighter elements and reactions during the stopping process. The correlation bands labeled from 1 to 6 indicate different groups of isotopes separated by their stopping power. A complete stop experiences the element in the top band 1 which expires more smoothly prematurely at about QDC_{PID2}=1500. In the case of the five lower groups 2-6 the maximum signal strengths in PID detector 2 increase from the sixth to the second line with sharp edges at the end.

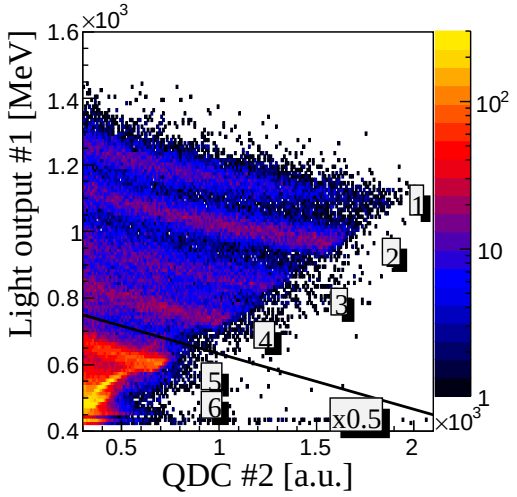

a) Energy signal correlation of the layer 1 and 2 from the PID detector for particles stopped in no. 2.

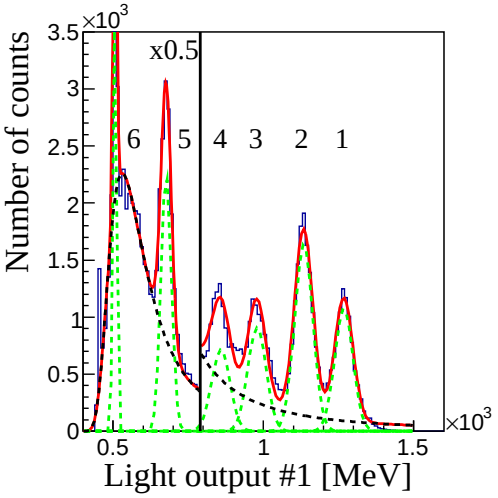

b) y-projection of a) for QDC_{PID2}<400

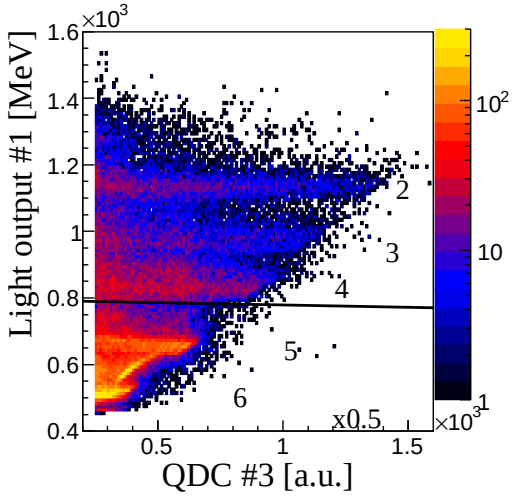

c) Energy signal correlation of the layer 1 and 3 from the PID detector for particles stopped in no. 3.

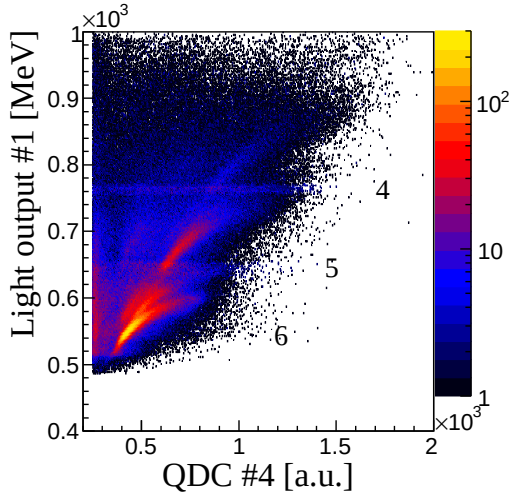

d) Energy signal correlation of the layer 1 and 4 from the PID detector for particles with events in the detector 4.

Figure 6.4: 2D and 1D light output spectra of the first PID detector with respect to the PID detectors no. 2 in a), no. 3 in c) and no. 4 in d) with cuts on the thresholds. Below the black lines the statistics is reduced by half.

The second row of figure 6.4 shows the signal outputs of PID detectors no. 3 (see c)) and no. 4 (see d)) with respect to no. 1 if the first three or all PID detectors detected reasonable signal amplitudes. As the group 1 was completely stopped in the second detector it vanishes, particles corresponding to groups 2 and 3 do not reach the PID detector no. 4. Types 4 to 6 are measurable until the last PID detector in d).

The events in group 1 are nitrogen isotopes which punch through the first PID detector and end up in the second detector (see table 6.1). While the other groups are elements with successive reduced number of protons (listed in table 6.1, last

Table 6.1: Combinations of the PID detectors and the stops of the particles. Signals above the threshold in the corresponding scintillator are indicated with "X" and their absence is marked with "O". The numbers in the second row "PID 1" represent the average energy deposit in layer 1 taken from the gaussian fits in figure 6.4 b).

	Group nr.					
ΔE [MeV]	1	2	3	4	5	6
PID 1	1268	1134	979	859	677	506
PID 2	X	X	X	X	X	X
PID 3	O	X	X	X	X	X
PID 4	O	O	O	X	X	X
Isotope	N	C	B	Be	Li	He & H

row) the band no. 6 splits into two in figure 6.4 d). It is therefore assigned to two elements, helium and hydrogen isotopes.

The composition of figure 6.4 a) changes when two complete tracks in the silicon tracker and in the hodoscope arms are required (see figure 6.5). Elements from Li to C are strongly suppressed or punch through the first two detectors without being stopped. Most of the events are below the threshold of the second PID detector indicating a full stop of these elements in PID detector no. 1. In contrast to the calculations in table 2.4 some nitrogen particles from the QFS $(p, 2p)$ reactions get an additional momentum kick in forward direction from the released internal momentum. Hence a part of the nitrogen isotopes overcome the first detector and loose their remaining energies in the second PID detector.

In order to select exclusively nitrogen the *residue gate* is set to the green marked area in the spectrum. From LISE++ calculations follow that

$$\epsilon_{res} = 77\,(1)\,\% \tag{6.5}$$

of nitrogen survives the punch through the Fe-degrader (including non-reacted ^{15}N particles and nitrogen isotopes after neutron-evaporations). The uncertainty is calculated from the probability of true events outside the chosen gate due to break ups in the first PID detector.

After the correct incoming and outgoing particles ^{16}O and ^{15}N as well as two protons in both arms have been selected, we will define requirements on the reaction participants which are typical for quasi-free scattered $(p, 2p)$ reactions.

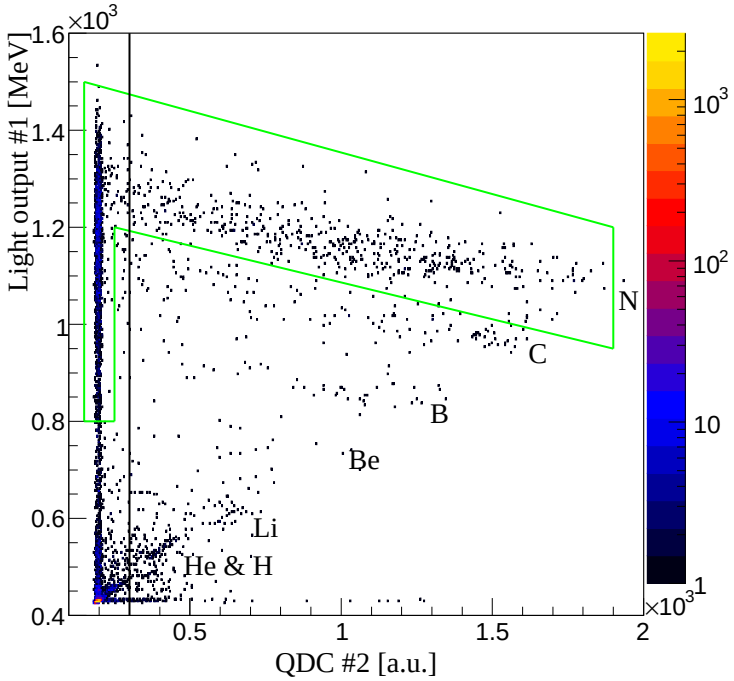

Figure 6.5: Light output spectra of the first two PID detectors under the conditions of the absence of signals in the following PID detectors and proton tracks in both arms of the $(p, 2p)$ setup. The green marked area encloses all nitrogen isotopes produced and is called *residue gate*. The black vertical line shows the set threshold used in figure 6.4 a).

6.4 Kinematic Constraints of QFS $(p, 2p)$ Reactions

The kinematics of the two released protons from QFS reactions is well-defined and restricted by the opening angle (see section 1.3.1). To select QFS $(p, 2p)$ reactions we exploit the special feature of this decay channel which is a narrow angular correlation between the two protons connected by the opening angle with

$$76\text{Â}^\circ < \theta_{op} < 84\text{Â}^\circ \tag{6.6}$$

which contains

$$\epsilon_{op} = 86\,(2)\% \tag{6.7}$$

of the $(p, 2p)$ events according to simulations (see figure 1.9 c)). This gate is valid over a wide range up to excitation energies of several dozens MeV (see the course of the opening angle at increasing nuclear excitations for beam energies E_{beam}>250 MeV/u in figure 1.10[1]).

Despite the weak kinetic energy correlation of the two protons (see figure 1.9 d)) the combination of the energy and opening angle information addition-

[1]The separation energy can be seen as equivalent to the excitation energy here

ally minimizes the phase space for other reactions in which also protons could be released. An empirical found connection between the polar angles $\theta_{1/2}$ and kinetic energies $E_{1/2}$ is shown in figure 6.6. The Geant4 simulation with exclusive $^{16}\mathrm{O}(p,2p)^{15}\mathrm{N}$ reactions shows the events dispersing around a narrow correlation (see figure 6.6 a)). In the first order approximation this second kinematic gate can be described by an exponential fit function where the green gate includes

$$\epsilon_{EWPA} = 94\,(2)\% \tag{6.8}$$

of the events uncorrelated to the gate on the opening angles in equation (6.7). In comparison, the experimental data (see figure 6.6 b)[2]) with two protons in each detector arm has plenty of events beneath and a smaller amount above the green gate. These events stem from a variety of reactions which release at least two charged particles but, due to the different kinematics of the protons from QFS $(p,2p)$ reactions, they can be sorted out.

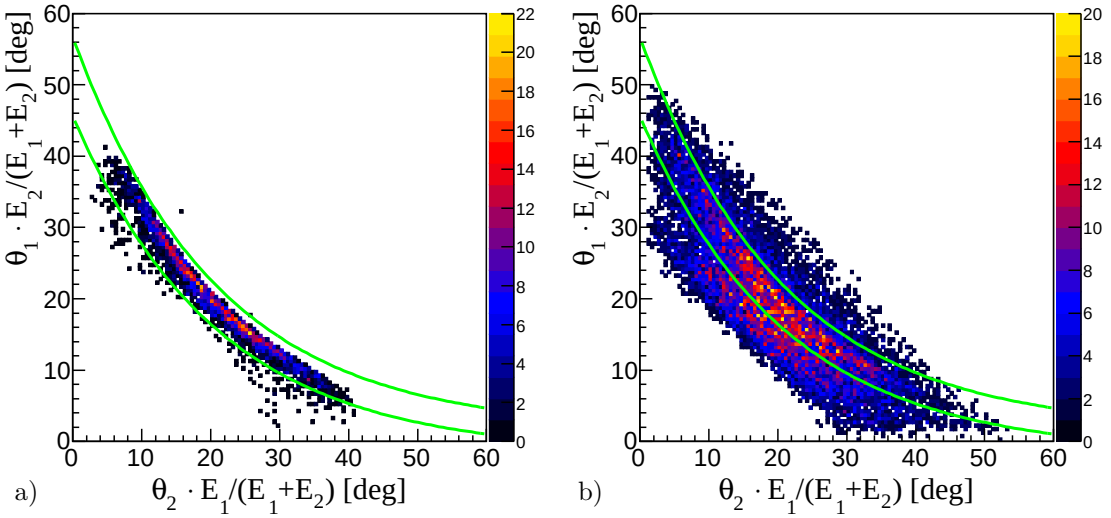

Figure 6.6: Distribution of QFS $(p,2p)$ events along the energy weighted polar angles of the two protons in the Geant4 simulation (see a)) and in the experimental data (see b)). The gate is transferred to b) in order to extract the QFS $(p,2p)$ events from the background.

The benefit of the two restrictions will be apparent in the next section where the effectiveness of background suppression is studied using the target assembly with polyethylene and pure carbon foils.

6.5 Background Suppression

The QFS $(p,2p)$ reaction channel is one of many scattering processes that can happen when two nuclei collide. There are several reaction mechanisms in which

[2]here the gate on the *residue gate* is not set, yet

protons are released and they are measured by the $(p, 2p)$ setup each. As an instrument for probing the selection of events stemming from QFS $(p, 2p)$ reactions serves the change of the event numbers in the polyethylene target and in the carbon target (compare the initial event distribution in figure 5.5 b)) after dedicated conditions were set. Since all events in the carbon target are background reactions their suppression is transferable to the events in the polyethylene target where the same reaction channels will be omitted.

The gates in sections 6.3 and 6.4 represent requirements which are tailored for the characteristic behavior of the particles (i.e., protons and residue) undergoing the QFS $(p, 2p)$ reaction. Setting the gates on the EWPA and on the opening angle constraints $\sim 1/3$ of the events in the CH_2 targets remain and in the carbon foil 10 % percentage points less events are leftover (compare table 6.2, third and forth row). The values almost keep the same if both kinetic gates are applied (compare figures 6.7 a) and c) and table 6.2, sixth row). They select the same type of scattering processes. The residue gate discards most events where less than 4 % remain in the carbon target but over four times more events are left over in the CH_2 target (compare table 6.2, fifth row). The strongest reduction of reactions in the carbon foil is achieved by setting the three gates together. Remaining events show that the gates cannot fully exclude reactions between the beam projectiles and the carbon. Some of them have attitudes of QFS $(p, 2p)$ reactions, whether the proton momenta are similar to the kinematics of the QFS or the deflection of the nitrogen residues was too small such that they could be measured in the PID detector array.

Table 6.2: Percentage of remaining counts after the gates are set with distinction between the polyethylene targets n_{CH2} and the carbon foil n_C. The column "norm." (*normalized CH_2 target*) lists the events in the polyethylene targets with proportional subtraction of remaining events in the carbon foil. The last column $\frac{n_{CH2}}{n_C}$ presents the ratio between the remaining events of the two targets.

	n_{CH2} [%]	n_C [%]	norm. [%]	$\frac{n_{CH2}}{n_C}$
All events	100.0	100.0	–	
EWPA gate	38.0	26.9	11.1 (1.4)	1.4
$76\hat{A}° < \theta_{op} < 84\hat{A}°$	31.0	18.6	12.4 (1.2)	1.7
Residue	14.7	3.7	11.1 (0.7)	4.0
EWPA gate & $76\hat{A}° < \theta_{op} < 84\hat{A}°$	28.5	16.5	12.0 (1.2)	1.7
EWPA gate & $76\hat{A}° < \theta_{op} < 84\hat{A}°$ & Residue	10.3	1.0	9.4 (0.5)	10.3

Subtracting the carbon background in the CH_2 targets yields the proportion of events associated to QFS $(p, 2p)$ reactions on hydrogen (see table 6.2, fourth column "norm."). Independent of the set gates, ≈10% of the initial number of events remain. In order to provide information concerning the significance of the single and combined gates the signal-to-background ratios n_{CH2}/n_C between the number of events in the two target types are calculated (compare table 6.2,

last column). It is an indicator of the selectivity on QFS $(p, 2p)$ reactions. In the case of the kinematic gates the ratios are slightly above 1 showing the large number of kinetically similar scattering processes on hydrogen and on carbon. The surface of the PID detector array was sufficiently small to separate nitrogen residues stemming from reactions with the carbon and thus the residue gate exhibits the highest individual selectivity of the three gates. By far the highest signal-to-background ratio of $n_{CH2}/n_C > 10$ is achieved by setting the three gates together. The ratio indicates a rather clean extraction of the desired reactions.

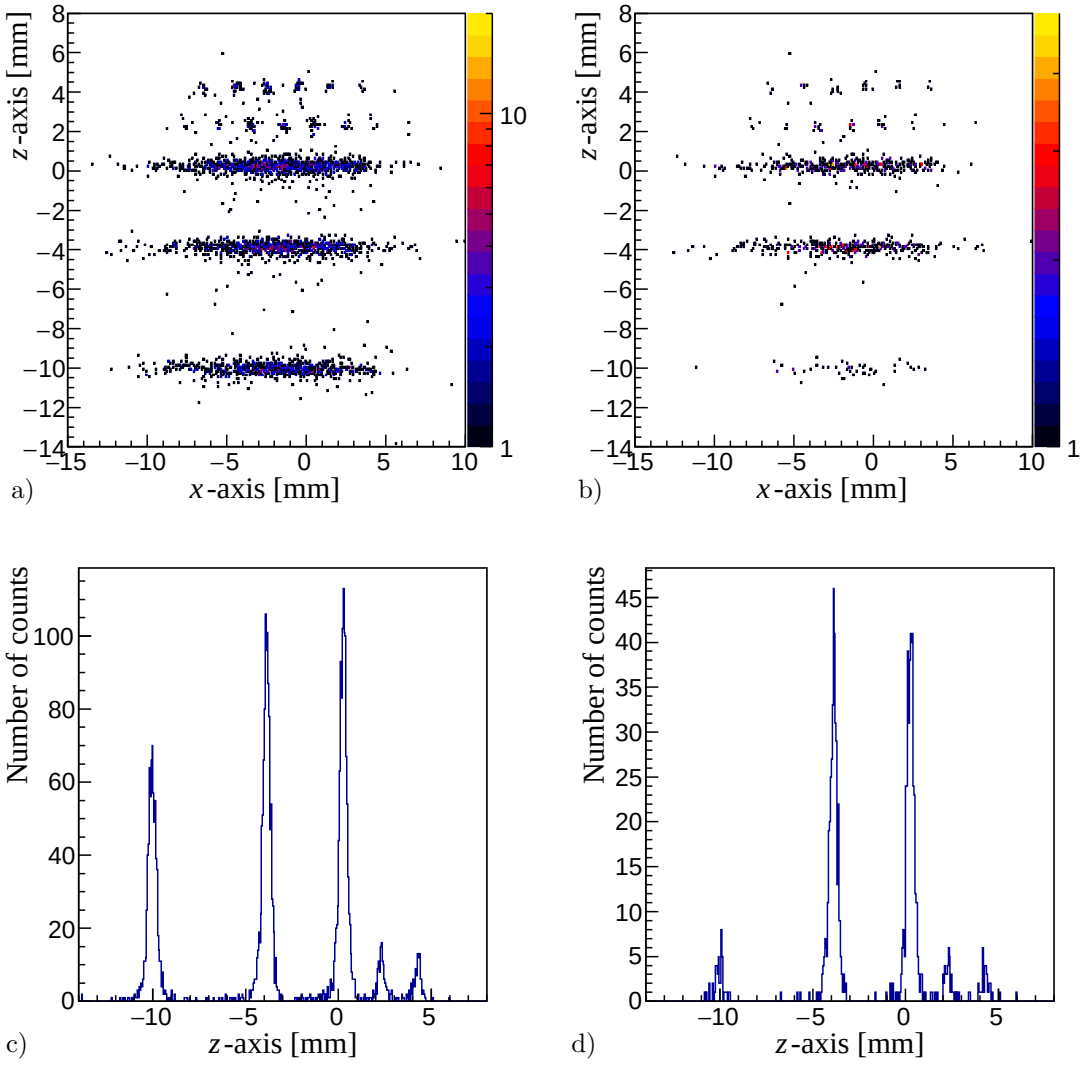

Figure 6.7: Effect of the gates on the number of entries in the vertex reconstruction onto the target in comparison to the initial figures 5.5 b) and d). Applying the gates on the EWPAs and the opening angle constraint exhibits the spectra in a) and c). If the gate on the residues is additionally set (see b) and d)) events from the carbon foil at $z_{tgt} \approx -10\,\text{mm}$ almost vanish completely.

With the current setup it is possible to select the QFS $(p, 2p)$ reaction with sufficient signal-to-background ratio. However, beside the exclusion of unwanted

reactions, also real QFS $(p, 2p)$ reactions had to be cut (see the expected reductions in the equations (6.5), (6.7) and (6.8)). Especially the residue gate lowers the efficiency but it is also most effective in cutting the background reactions with carbon. Instead of excluding these reactions by software the largest background source, i.e., carbon, can be avoided by using pure hydrogen targets like liquid hydrogen (LH_2) targets.

6.6 Excitation Energy Spectrum

The derivation of the excitation energy from the missing mass was presented in section 1.3. Here we connect the physical quantities momenta and energies with the measured parameters polar and azimuthal angles and the velocity β_i of the two protons $(i = 1, 2)$ and show the excitation energy spectrum for different constraints on the event pattern.

The proton angles are each obtained by straight lines through two hit positions in the silicon detectors relative to the incoming beam. For the horizontal angles, the hits in the first two layers are used whereas in the case of the vertical angles tracks are calculated from the y-positions of the projectile in the target (determined by the BDC) and the proton hit positions in the third layers. The relative flight direction of the protons with respect to the flight directions of incoming beam particles is equivalent to the transformation of the coordinate system by rotating it around the three dimensional matrix $\mathbf{a}(\chi_X, \chi_Y)$,

$$\begin{aligned}\mathbf{a}(\chi_X, \chi_Y) &= \begin{pmatrix} cos(\chi_Y) & sin(\chi_X)sin(\chi_Y) & cos(\chi_X)sin(\chi_Y) \\ 0 & cos(\chi_X) & -sin(\chi_X) \\ -sin(\chi_Y) & sin(\chi_X)cos(\chi_Y) & cos(\chi_X)cos(\chi_Y) \end{pmatrix} \\ &\overset{\chi_Y=0}{=} \begin{pmatrix} 1 & 0 & 0 \\ 0 & cos(\chi_X) & -sin(\chi_X) \\ 0 & sin(\chi_X) & cos(\chi_X) \end{pmatrix}\end{aligned} \tag{6.9}$$

with χ_X and χ_Y as the horizontal and vertical angles of the beam projectile relative to the z-direction (provided by the BDC). The influence of the vertical beam direction will be negligible in the later analysis and therefore set to χ_Y=0.

The flight direction $\vec{\alpha_i}$ of the protons is defined as the normalized vector directed through the origin of reactions T and the hits in the first silicon layers D_i of each arm,

$$\vec{\alpha_i} = \frac{\mathbf{a}(\chi_X, 0)}{\sqrt{(x_T - x_{Di})^2 + (y_T - y_{Di})^2 + (z_T - z_{Di})^2}} \begin{pmatrix} x_T - x_{Di} \\ y_T - y_{Di} \\ z_T - z_{Di} \end{pmatrix}. \tag{6.10}$$

The momentum $\vec{p_i}$ of the protons are obtained by the normalized flight direction $\vec{\alpha_i}$ and the absolute momenta $|\vec{p_i}|$,

$$\vec{p_i} = \vec{\alpha_i}|\vec{p_i}| = \vec{\alpha_i}\sqrt{E_i^2 - (m_p c^2)^2} \tag{6.11}$$

where $|\vec{p_i}|$ is expressed by the total proton energy E_i and the rest mass $m_p c^2$.

Since the protons decelerate by passing through materials before hitting the TOF detectors, a kinetic energy dependent additional term $\Delta E_i(\beta_i)$[3] is used to balance these energy losses, i.e.,

$$E_i = \frac{m_p c^2}{\sqrt{1-\beta_i^2}} + \Delta E_i(\beta_i). \tag{6.12}$$

Further values to calculate the excitation energy in equations (1.10) and (1.11) are the nuclear masses[4] of the proton m_p, the beam nucleus $m_A = m_{^{16}O}$, the residue $m_{A-1} = m_{^{15}N}$ and the total energy $E_A = E_{^{16}O}$ (kinetic energy plus rest mass).

First we show the results of the Geant4 simulation. It includes the detector resolutions of the silicon tracker, the hodoscope arms and the BDC. The missing data of the left third layer of the silicon tracker were replaced by the y-positions of the particles in the left-armed TOF detectors to determine the vertical flight directions (see section A.4.3 where the additional uncertainty is considered).

Table 6.3: Spectroscopic factors of ^{15}N of the ground state and the fragmented first excited state, *from* [82]. The corresponding proportion in the decays are listed in the third row such that the sum is 100%. Taking these ratios as input data the last row shows the output ratios between the ground state, the strong and the cumulated weak excited states of the Geant4 simulation.

	$p_{1/2}$	$p_{3/2}$ at E_{Exc}=6.32 MeV	$p_{3/2}$ at E_{Exc}=9.93 MeV	$p_{3/2}$ at E_{Exc}=10.70 MeV
Spectr. Factor	1.26	2.35	0.13	0.225
Literature [%]	31.8	59.3	3.3	5.6
Geant4 Sim. [%]	34.2 (22)	55.6 (28)	10.2 (12)	

The ratios between the transition probabilities of the two p-shells in ^{15}N are taken from measured spectroscopic factors [82] (see table 6.3, second and third row). The excited state was split into the strong and two weak transitions with $E_{p3/2}^{str} = 6.32\,\text{MeV}$, $E_{p3/2}^{weak1} = 9.93\,\text{MeV}$ and $E_{p3/2}^{weak2} = 10.70\,\text{MeV}$.

The resulting excitation energy spectrum consists of the two dominant peaks of the ground state $p_{1/2}$ and the splitted excited state $p_{3/2}$ (see figure 6.8 a)) which

[3] calculated by ATIMA

[4] from http://t2.lanl.gov/data/astro/molnix96/massd.html: $m_p = 938.27\,\text{MeV}/c^2$, $m_{^{16}O} = 14895.080\,\text{MeV}/c^2$, $m_{^{15}N} = 13968.935\,\text{MeV}/c^2$ and $E_{^{16}O} = m_{^{16}O}c^2 + 16 \cdot E_{beam} = 19468.52\,\text{MeV}$ with E_{beam}=285.84 MeV/u at the target position

appears as one peak with a right shoulder. Since the two weak transitions are not separated due to the detector resolutions they are considered as one peak with fixed position set on the weighted average of both states. The spectrum is described by three Gaussian fit functions with the same width. A fourth peak would just increase the degrees of freedom but dilute the significance of the result. The standard deviation of the peaks was assumed to be

$$\sigma_{Exc}^{Sim} = 1.1 \text{ (stat.)} \pm 0.2 \text{ (syst.) MeV} \tag{6.13}$$

and hence slightly higher than the set goals in equation (1.5). This is due to the less precise method to determine the vertical flight direction of the protons in the left arm by using the TOF detectors. Furthermore, we included non-coherent hit positions in the left third layer and the hodoscope arm according to empirical observations (see figure A.1) causing strongly smeared events, e.g., visible between the peaks of the ground state and excited states.

The different ratios between the three fitted peaks and the input distribution (compare table 6.3 where the third row was used as input and the fourth row presents the output ratio) follow from the superimposition of the geometric acceptance of the opening angle where the optimum detection coverage was designed for opening angles $\theta_{op} = 84\hat{A}^\circ$. The decrease of the (average) opening angle at higher excitation energies leads to a lower effective spatial coverage of the two protons. In our experiment with $\Delta\theta_{op} > 1\hat{A}^\circ$ between the ground state and the first excited state (see the y-projection of figure 6.8 b)) this effect can be already observed. Thus, we use the changed ratio between the ground state and the summed first excited state as correction factor and list the corrected peak content in table 6.4. Different from that the discrepant ratio between the peaks of the strong and weak $p_{3/2}$ transitions can be explained by uncertainties in fitting the small shoulder but also by considering the two weak transitions $E_{p3/2}^{weak1}$ and $E_{p3/2}^{weak2}$ as one peak.

Figure 6.8 b) shows the opening angles with respect the excited states. The y-projection of each excitation energy provides the spread of the opening angles. It corresponds to the theoretical distribution (compare figure 1.9 c)) and follows the trend towards smaller values for higher excitation energies. The opening angles are in particular uncorrelated to fixed excitation energy each.

The same kind of plot is shown for the experimental data in figure 6.9 a)[5]. In contrast to the simulated spectrum an inner structure appears with a slight left-tilted correlation. This unphysical behavior is corrected by projecting the excitation energies onto the vertical violet line. Above the solid green line the shift of the events seems to be stronger than in the lower part indicated with the dashed green lines for the ground state events. Assuming correct opening angles the events were shifted horizontally and as a result the excitation energy

[5]In this spectrum the *residue gate* was set to clean the spectrum of background

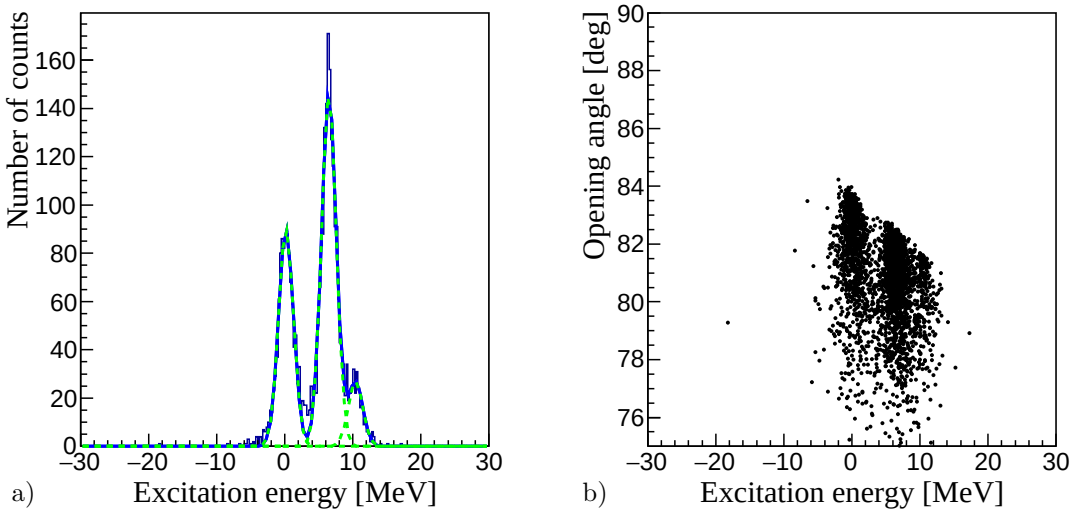

Figure 6.8: Geant4 simulation of the excitation energy of the first three excitations of ^{15}N derived from the missing-mass spectroscopy using the reaction $^{16}\mathrm{O}(p, 2p)^{15}\mathrm{N}$. In a) the peaks are fitted with Gaussian fit functions with the same width for the three peaks. The correlation between the opening angle and the excitation energy is shown in b).

is independent of the spread of the opening angle (see figure 6.9 b)). As a belated correction of the calibration it is justified to use the modifications in the further analysis.

Figure 6.10 d) shows the excitation energy spectrum which can be directly compared to the simulation (see figure 6.8 a)). There the three gates were set such that the very low contribution from reactions with carbon is insignificant (illustrated as red events). The resolution of the excitation energy is best described by Gaussian fit functions including left tails (see equation (A.2)), indicated by the green dashed lines, and exhibits

$$\sigma_{Exc} = 1.2\ (\text{stat.}) \pm 0.3\ (\text{syst.})\,\text{MeV}, \tag{6.14}$$

using the width of the Gaussian part of the fit function. Detailed studies showed that the occurring left tails stem from underestimated walk-corrections for small light outputs. Higher lying states at $E_{Exc} \approx 14\,\text{MeV}$ might stem from two narrow peaks at $12 < E_{Exc} < 14\,\text{MeV}$ (compare figure 3.4 b)) in front of the continuous excitation energy distribution of the s-hole states. However, they were not taken into account in this analysis.

The resolution is in accordance with the value of the simulation (see equation (6.13)). Also, other key parameters (see table 6.4, last column) correspond to the results of the Geant4 simulation.

In figure 6.10 the single steps of event selection and background subtraction are repeated on the excitation energies to understand the different impacts of the gates. The raw experimental spectrum includes all events in which the beam

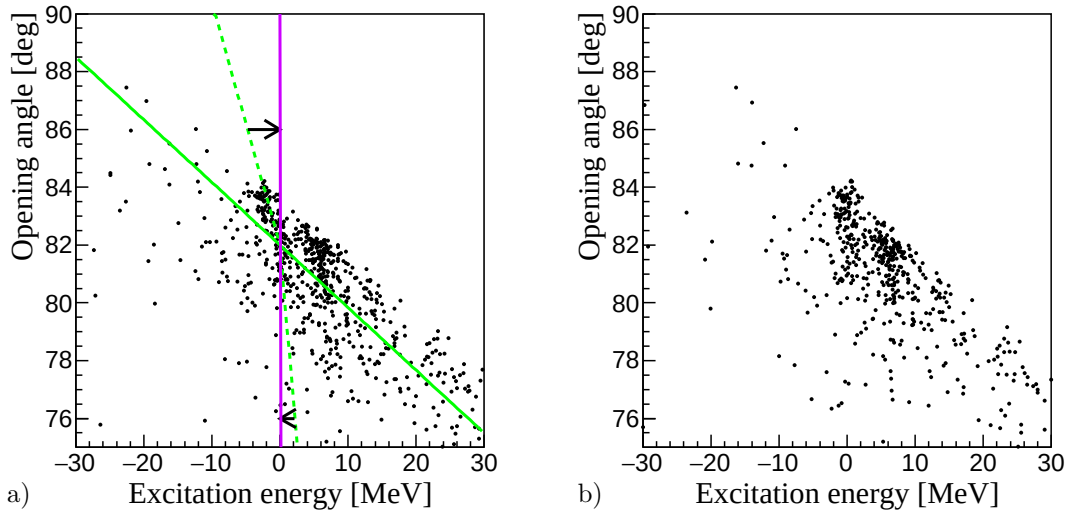

Figure 6.9: The opening angles are plotted with respect to the excitation energy spectrum with gate on the residue. In the initial spectrum in a) the two dominant peaks at E_{Exc}=0 and 6.3 MeV walk with the opening angle (indicated by the dashed green line). In the corrected spectrum in b) each excitation energy peak is independent of the different opening angles.

Table 6.4: Attitudes of the simulated and experimental determined transition. The associated spectra and fits are shown in figure 6.8 a) (see the second column), figures 6.10 c) and d) (see the third and fourth column). The resolution $\sigma(E)$ is divided into the width of the Gaussian shaped peaks (in sigma) and the maximum shift between the peak positions of the fit and from literature. The row labeled with "peak" includes the peak positions of the three peaks of the ground state $p_{1/2}$ and the strong and weak transitions of the first excited state $p_{3/2}$. Rows with "Share" provide the (geometrical corrected) percentage of content in each peak with respect to the total number of events in the three peaks.

	Geant4 Sim.	EWPA & $76\hat{A}° < \theta_{op} < 84\hat{A}°$	EWPA & $76\hat{A}° < \theta_{op} < 84\hat{A}°$ & Residue
$\sigma(E_{Exc}) \pm \Delta E_{Exc}$ [MeV]	1.1 ± 0.2	1.3 ± 0.6	1.2 ± 0.3
$\sqrt{\frac{\chi^2}{Ndf}}$	1.16	1.30	1.11
peak of $p_{1/2}$ [MeV]	0.17	0.12	0.29
share of $p_{1/2}$ [%]	31.8 (20)	32.2 (42)	34.3 (29)
peak of strong $p_{3/2}$ [MeV]	6.49	6.22	6.28
share of strong $p_{3/2}$ [%]	57.6 (29)	50.6 (57)	51.6 (37)
peak of weak $p_{3/2}$ [MeV]	10.4 (fix)	10.00 (fix)	10.00 (fix)
share of weak $p_{3/2}$ [%]	10.6 (12)	17.2 (42)	13.8 (19)

particles and the two emitted protons are well defined with respect to flight directions and energies (see figure 6.10 a)). The events are divided according to the origins of the reactions (in blue: polyethylene films and in red: carbon target). The blue spectrum already shows structures of two peaks at around $E_{Exc} \approx 0$ MeV and $E_{Exc} \approx 6$ MeV sitting on background described by the rather

mound shaped red marked distribution with a maximum at $E_{Exc} \approx 3\,\mathrm{MeV}$. Since the derivation of the excitation energy is dedicated to QFS $(p, 2p)$ reactions on unbound protons as target (see equations (1.10) and (1.11)) events of different decay channels are assigned to random excitation energy values along the whole spectrum without physical meaning.

Compared to the typical total cross sections in the order of $\sigma_{CS} \sim 1\,\mathrm{barn}$ for reactions between two medium heavy nuclei at $E_{beam} \sim 300\,\mathrm{MeV/u}$ [83] the dedicated design of the $(p, 2p)$ setup reduces the red carbon background significantly to an integrated cross section of $\sigma_{CS} \approx 65\,\mathrm{mbarn}$ (using equation (6.16)) even without setting any gates. On the other hand the two dominant peaks peeling out in the blue spectrum show the high selectivity to QFS $(p, 2p)$ reactions.

The use of the gates on EWPAs and opening angle constraints cuts events with low and high excitation energies ($E_{Exc} < -50\,\mathrm{MeV}$ and $E_{Exc} > 40\,\mathrm{MeV}$) but has minor influence on the background in the relevant energy range $0 < E_{Exc} < 10\,\mathrm{MeV}$ (see figure 6.10 b)). Subtracting the re-scaled carbon spectrum the shapes of the two peaks become more clear and the background at negative excitation energies almost vanished (see figure 6.10 c)). The fits on the three peaks show similar attitudes like the final excitation energy spectrum (see figure 6.10 d) and for comparison table 6.4). Even without the gate on the nitrogen residue it is possible to reconstruct the excitation energy spectrum although the key parameters resolution and offset were scarcely amiss.

In this section we showed that the new setup is able to exploit the missing mass spectroscopy of QFS $(p, 2p)$ reactions to reconstruct the excitation energy spectrum of ^{15}N with the necessary resolutions. In order to ensure a consistent picture of the experimental data with previous studies the last part of the chapter studies the momentum distribution and the exclusive cross section of the QFS $^{16}\mathrm{O}(p, 2p)^{15}\mathrm{N}$ reaction.

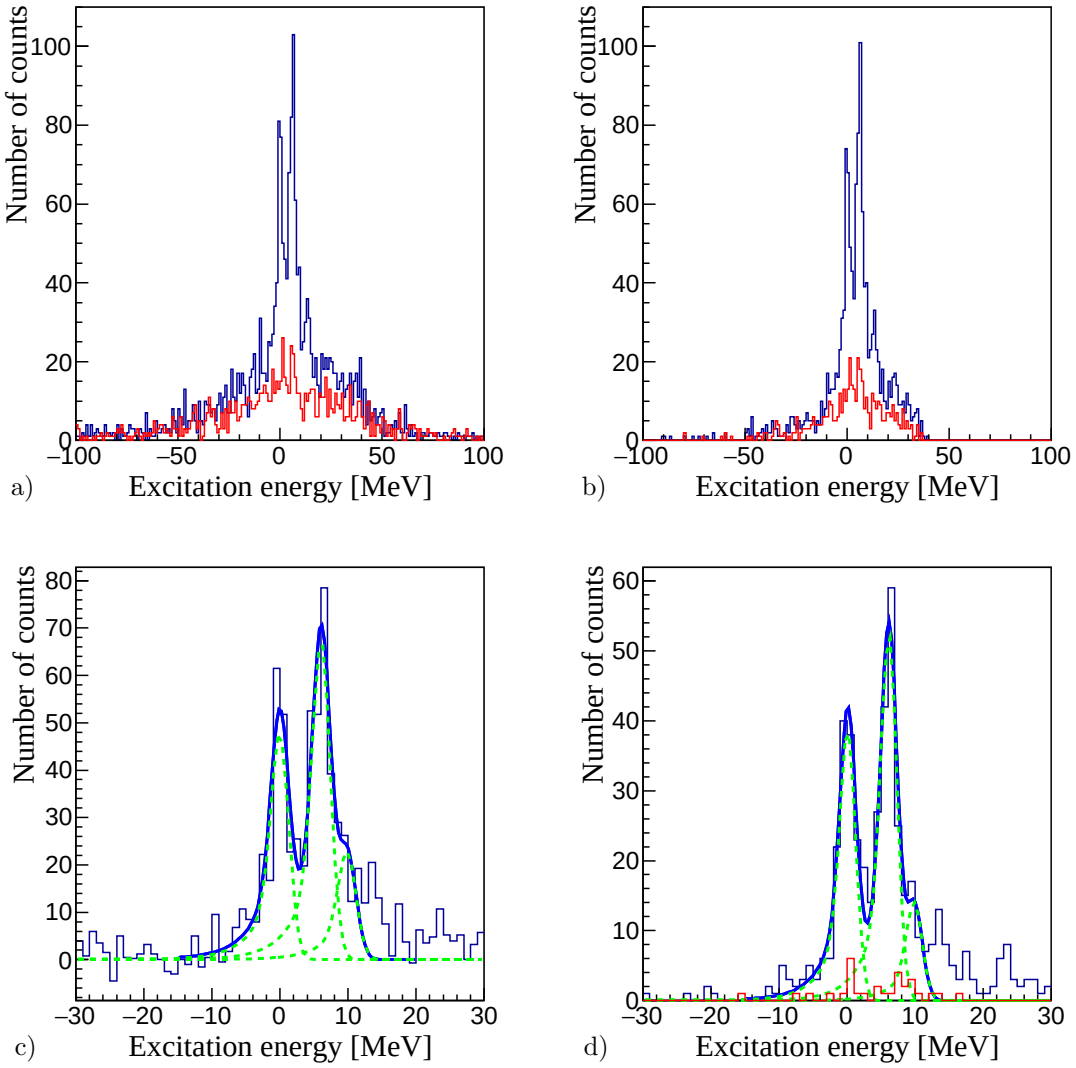

Figure 6.10: Experimental excitation energy spectrum under different cut conditions. The blue spectra in a), b) and d) correspond to the reactions in the polyethylene target foils, the red spectra contain the entries from the carbon foil. The raw excitation energy spectrum is shown in a). The kinematic constraints (see equations (6.6) and the gate in figure 6.6 b) are applied in b). The ranges of the two spectra are enlarged from $-100 < E_{Exc} < 100$ MeV to illustrate the effect of the gates on the events with large excitation energies. The subtraction of the re-sized number of events stemming from the C foil from the events in the CH_2 foils is conducted in c). Additionally to the gates applied in b) the residue gate (see figure 6.5) is set in d). The three peaks of the ground and excited state of ^{15}N are fitted with Gaussian fit functions and left tails. The peak of the weak transitions of the excited state $p_{3/2}$ is visible only as a shoulder of the main peak of the strong $p_{3/2}$ transition.

6.7 Momentum Distribution

The momentum measurements of the two emitted protons allow to determine the orbital angular momentum of the sub-shells l where the bound protons were knocked-out (see equation (1.12)). We will show on the example of the two dominant peaks $1p_{1/2}$ and $1p_{3/2}$ that our setup is able to reproduce the simulated momentum distributions and serves therefore as powerful tool to look into the nuclear structure.

The shapes of the internal momenta of the p-orbitals are approximated as normal distributed with the widths of $\sigma_{p1/2}$=95 MeV/c and $\sigma_{p3/2}$=102 MeV/c using the simulated momentum distribution of the QFS ^{16}O$(p,2p)^{15}$N reaction at E_{beam}=451 MeV/u [27]. Weighted with the theoretical proportions of the two peaks the momenta are added and folded with the spatial coverage of the $(p,2p)$ setup. In the case of the longitudinal momentum distribution the shape is approximated as Gaussian distribution and the transverse and total momenta are well described by Landau fit functions.

In the reference frame of the incident beam projectile, the longitudinal momentum is shifted to the left of zero due to the negative Q value which reduces the available kinetic energy [84] (see figure 6.11 a)). The measured distribution shows furthermore a more asymmetric shape counting a tail on the high momentum side. This might be a consequence of the conservation of energy and momentum, guaranteed by the phase volume effect which strengthens for decreasing beam energies [84].

The transverse momentum is more sensitive on the different orbits since the peak positions of the sub-shells differ more clearly than in the longitudinal case due to the add of influences like the Coulomb potentials [31] (compare the momentum distributions of the s- and p-shells in figures 1.11 a) and b)). The agreement of the experimental data with the simulated curve (see figure 6.11 b)) indicates that the two dominant peaks in the excitation energy spectrum of ^{15}N stem from the knock-out reactions of protons in the p-shells.

Information about the wave functions of the nucleons in the sub-shells is provided by the total momentum (see figure 6.11 c)). The measured momentum distribution follows the simulated curve with an excess of events at small momenta ($|\vec{p}_3| \approx 70$ MeV/c).

Despite its simplified structure the simulated orbital angular momentum classifies the first two peaks in the excitation spectrum as associated to the p-orbitals. Small deviations occurred from neglected effects like the asymmetric distribution of the longitudinal momentum which become relevant at our beam energy. Advanced simulations, e.g., by the THREEDEE code [85], using the experimental beam energies would clarify if this asymmetry is reproducible.

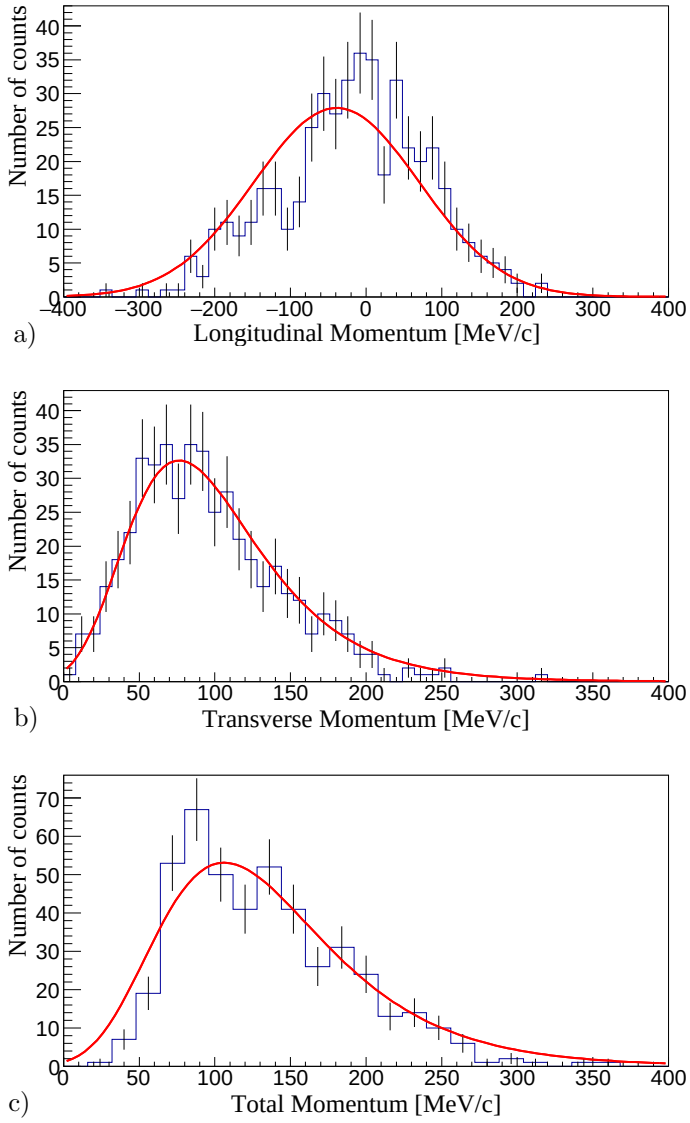

Figure 6.11: Measured experimental longitudinal (see a)), transverse (see b)) and total momentum distribution of the two dominant peaks $p_{1/2}$ and $p_{3/2}$, transformed to the reference frame of the incident beam projectile. The simulated distributions $p_{1/2} + p_{3/2}$ are illustrated by the red curves.

The small amount of detected high excited events (see figure 6.10 d)) stems from the s-shell but due to the low statistics its characteristic momentum distribution cannot be figured out and we refrained from the analysis.

6.8 Cross Section

The accurate determination of the cross section is helpful for theorists as input parameters in large-scale shell model calculations [33]. Especially, the assumed break-down of the magic shells close to the dripline (see section 1.3.3) is relevant for the nucleosynthesis in the r-process and hence, the determination of cross

sections will be an essential part in proposed experiments with neutron-rich heavy nuclei. The exclusive cross section indicates the probability P of QFS $(p, 2p)$ reactions of the beam nuclei with the target, i.e., the ratio between the number of reactions $Y(p, 2p)$ and the number of incoming beam nuclei N_b [65],

$$P = \frac{Y(p, 2p)}{N_b}. \tag{6.15}$$

In order to make a general statement about the reaction probability, we divide the value by the number of hydrogen particles N_t in the target, the run time t_s and the total setup efficiency ϵ_{P2P} (see equation (A.7)). The gates in section 6.5 and in the appendix A.3 additionally reduce the number of QFS $(p, 2p)$ events (compare the equations (6.5), (6.7), (6.8), (A.8), (A.9)). Taking them into account the exclusive cross section of the QFS $^{16}\mathrm{O}(p, 2p)^{15}\mathrm{N}$ reaction is obtained by

$$\frac{d\sigma}{dE_x} = \frac{1}{\epsilon_{res}\epsilon_{op}\epsilon_{EWPA}\epsilon_T\epsilon_Y} \frac{P}{N_t t_s \epsilon_{P2P}} = \begin{cases} 9.8\,(8)\,\mathrm{mbarn} & \text{for } p_{1/2} \text{ state} \\ 18.7\,(11)\,\mathrm{mbarn} & \text{for } p_{3/2} \text{ state.} \end{cases} \tag{6.16}$$

Calculations with the eikonal theory [32] amount to $\sigma_{gs} = 13.2\,\mathrm{mbarn}$ and $\sigma_{es} = 25.1\,\mathrm{mbarn}$ for the ground state and first excited state transitions at E_{beam}=451 MeV/u [28]. The experimental cross sections are lower than the theoretical calculations which is expressed by the reduction factor $R = 0.75\,(5)$. This is in agreement with previous measurements of $(p, 2p)$ and $(e, e'p)$ data [28] [86]. There the inclusive $(p, 2p)$ cross section was determined whereas we pinged to the exclusive QFS reaction channel. However, we showed that in the region of our beam energy most of the scatterings are quasi-elastic (see section 1.3.3) and we can therefore equate the exclusive QFS part with the total $(p, 2p)$ cross section.

The last three sections showed that the newly developed $(p, 2p)$ setup for experiments in inverse kinematics reproduces the results carried out in normal kinematics. In the next chapter we will give a brief conclusion of the presented experiment and will then focus on changes of the experimental conditions for experiments with heavy radio-isotope (RI) beams.

Chapter 7

Conclusion and Outlook

7.1 Résumé

In the region of exotic nuclei with their unknown and complex decay pattern (see section 1.1), the currently available experimental techniques came to their limits. With the new $(p, 2p)$ setup we aim for a conceptually new approach to open new experimental opportunities.

This dissertation presented a new method for determining the excitation energy of nuclei by means of the missing mass spectroscopy using the QFS $(p, 2p)$ reaction in inverse kinematics. For this purpose, a two-arm setup with three layers of silicon detectors and one hodoscope stack each was developed to measure the opening angle and time-of-flights of the emitted protons with high resolution.

In table 7.1 we summarize the relevant key parameters together with the defined goals. The resolutions of the vertex reconstruction in the three spatial directions are in good agreement with the specifications. The proton energy resolution also complied with the requirements, however, small left tails in the excitation energy spectrum indicated the high sensitivity to the TOF calibration. In the current setup the accuracy in calibration was limited by the lack of information. To avoid this in future modifications will be discussed in section 7.4.

Table 7.1: Comparison between the required and achieved resolutions of each detector and of the two relevant magnitudes energy and opening angle of the setup in sigma.

Component	Requ. res.	Achieved res.
x- and z-target [µm]	190	195
y-target [µm]	750	488
TOF [ps]	120	123
$\sigma(\frac{\Delta E_p}{E_p})$ [%]	2.4	2.4
$\sigma(\theta_{op})$ [mrad]	2.5	2.7
$\sigma(E_{Exc})$ [MeV]	1.0 ± 0.5	1.2 ± 0.3

Yet a resolution of the excitation energy σ_{Exc}=1.2 ± 0.3 MeV could be achieved in the demonstrator experiment using the QFS ^{16}O$(p, 2p)^{15}$N reaction. It was also possible to draw the shape of the momentum which will be needed to determine the orbital shell of the struck proton. The $(p, 2p)$ cross section agreed with previous ^{16}O$(p, 2p)^{15}$N experiments. This is an important feature since from the trend towards exotic nuclei, conclusions of the nuclear structure can be derived.

7.2 Outlook

The successful test of the $(p, 2p)$ setup with the achievement of the required resolution in the excitation energy was a major step towards the experimental campaign for the determination of fission barrier heights (see section 1.2). In this work it was demonstrated that the accomplished resolution will be sufficient to determine the slope and final value of the fission barrier heights under discussion (compare figure 1.4). To further prepare on realistic environments a part of the experimental campaign was dedicated to study the influence of heavier projectiles on the setup.

The last day of the campaign was used to change the beam from the light projectiles ^{16}O to a significantly heavier beam ^{132}Xe and the same beam velocity to study the differences of the signal distributions in the silicon tracker. Using the identical target and detector setup the main focus here is less on the QFS $(p, 2p)$ reaction than on the description of additional background, and the effects of high charged particle multiplicities.

Characteristic for heavy ion beams through materials is the precipitous increase of δ-electrons whose yield is in first order proportional to the energy loss of the beam particles [87] [88]. In the case of fission even several 100 δ-rays are expected for each beam particle [77]. The energy spectrum of these electrons depends on the polar angle relative to the beam direction [89],

$$E_\delta \propto \frac{1}{cos^2\theta} \tag{7.1}$$

and can reach up to a few hundred keV. This energy is sufficient that many electrons leave the target and reach the silicon detectors where they will induce significant signal amplitudes.

Since the silicon tracker is designed for events with low multiplicity the current setup and especially the analysis software have to be optimized for these conditions. A protective film of a d=10 µm thick aluminized mylar foil was therefore mounted 1 cm in front of the first right-arm detector D2 to decelerate the δ-electrons. For comparison, the left arm was left blank. Figures 7.1 a) and b) show the cluster multiplicities in the first and second layer and in the corresponding hodoscope for the left and right arm. The first layers have clearly higher absolute values (M_{D1}=10 and M_{D2}=9) than the second layers (M_{D3}=M_{D4}=3).

Especially compared to the multiplicities of mostly 1 in the hodoscope arms[1] the heavy nuclei lead to a strong increase of background in the first layers and to a lesser extent in the second layers.

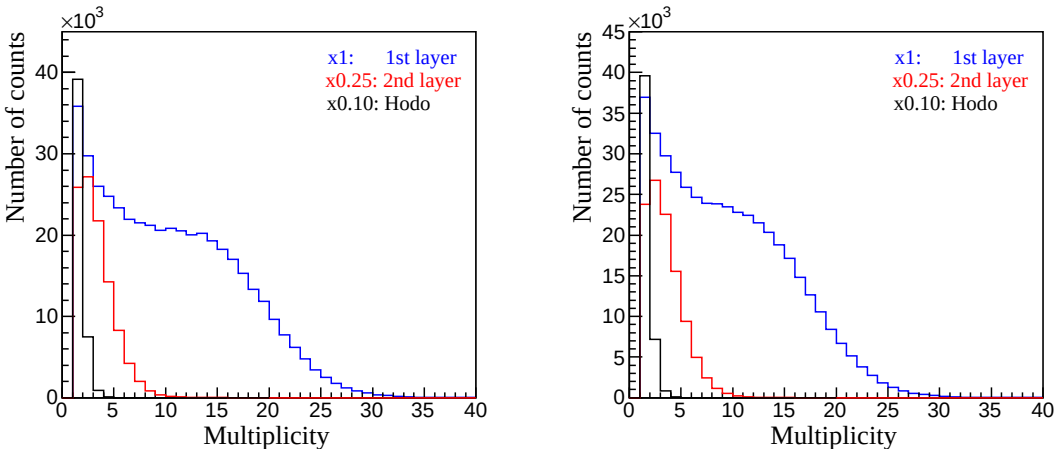

a) Multiplicity in the unshielded first silicon detector D_1

b) Multiplicity in the protected first silicon detector D_2

Figure 7.1: Multiplicity of the first two layers and of the hodoscope arms (in blue: 1st layer, in red: 2nd layer, in black: Hodoscope arm). The events of the second layer (respective hodoscope arm) were multiplied by a factor of 0.25 (respective 0.10) to compare the distribution in one histogram.

The correlations of the highest clusters between the two layers provide information about the signal-to-background ratio (see figures 7.2 a) and b)). The track of protons from nuclear reactions in the target are on a diagonal with the same horizontal angles in the two detectors due to their alignment around the center. Since the beam and the target are spatial expanded the green borders include the acceptable signals which can be traced back to the target areas.

Background means the random correlation of two highest clusters which do not correspond to a straight proton track. Both spectra have a large amount of uncorrelated events increasing with smaller horizontal angles in the first layers. This is probably a consequence of the higher probability of the emission of high-energetic δ-electrons at small polar angles (see equation (7.1)). In contrast the events in the second layers are isotropically distributed along the whole surface (see the y-distribution in figures 7.2 a) and b)).

The explicit energy distributions in the first layers at small and large horizontal angles are studied on the basis of figures 7.3 a) and b) where the events inside the rectangular green and black marked areas of figures 7.2 a) and b) are superimposed. Except the different number of events the spectral shapes are almost identical. The blue spectra only differ in a small excess of low energy signals in the range from 50-90 keV.

[1] Gates on the proton signatures in the TOF detectors are set (compare figure 6.3)

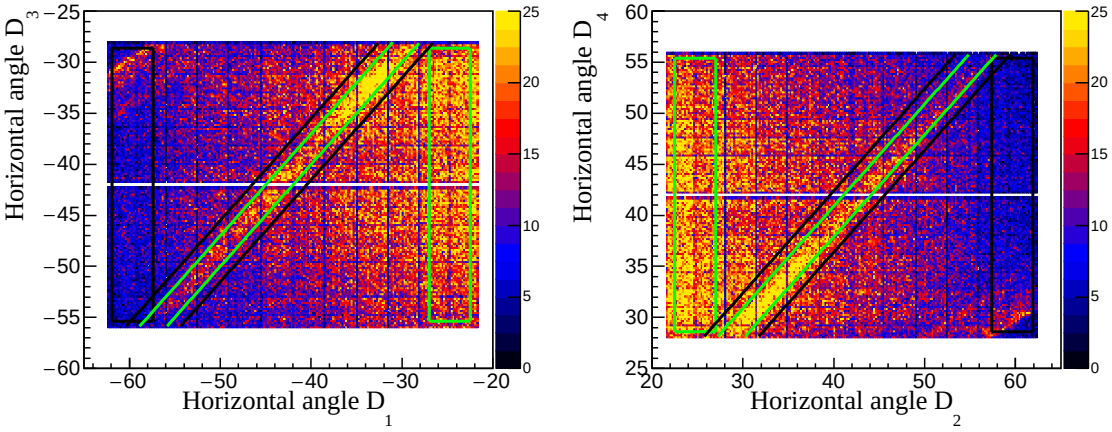

a) Correlation between the highest clusters in the two layers of the left arm

b) Correlation between the highest clusters in the two layers of the right arm

Figure 7.2: Comparison of the highest cluster distribution between the two layers in each arm. The green marked areas are gates on the δ-electron area (rectangular) and on the proton tracks from the target area (diagonal). The associated black areas refer as background. The separation of two areas in the y-axis stem from the distance between the two wafers in the second layers.

Same energy spectra were also plotted for the green and black marked diagonal areas in figures 7.2 a) and b) which mark the regions of possible tracks from the target and background respectively (compare the associated figures 7.3 c) and d)). The similarity of the two spectra, presented in the form of the signal-to-background ratio S/N of

$$S/N = \frac{\text{Number of counts in green area}}{\text{Number of counts in black area}} = 1.3, \tag{7.2}$$

is due to a similar energy deposit of δ-rays and protons in the silicon detectors.

All spectra reveal no difference between the left and right arm. The mounted mylar foil in the right arm does not shield the first silicon detector significantly. The drop of multiplicities between the two first layers, however, indicate that the 100 µm thick silicon wafers in the first layers sufficiently protects the detector behind from background.

A sheet of 100 µm thick silicon in front of the silicon detectors should therefore shield the silicon tracker from δ-electrons. The thickness must be seen as an upper limit and tests in advance are needed to find the lowest acceptable sheet thickness since the foils act like additional obstacles. They deflect the flight directions of the protons in the first and second silicon layers (in contrast to the effects of scatterings in the first layers which shift the hit positions in the second layers only). Implementing the additional silicon sheet in the Geant4 simulation the increase of the excitation energy resolution exceeds even that caused by the first layers (see table 7.2). The optimum shielding material should hence fulfill

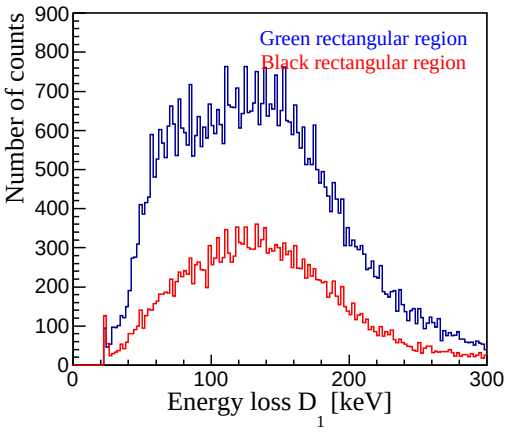

a) Energy loss of the events in D_1 inside the rectangular areas in figure 7.2 a)

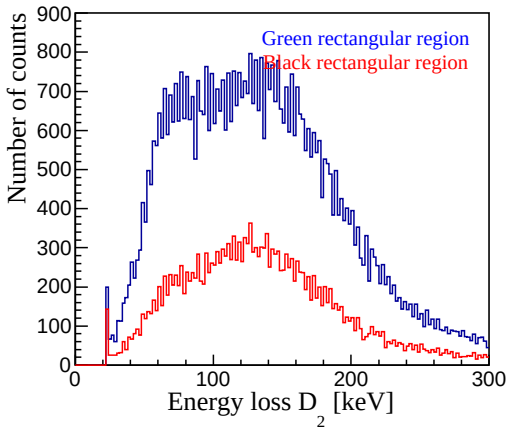

b) Energy loss of the events in D_2 inside the rectangular areas in figure 7.2 b)

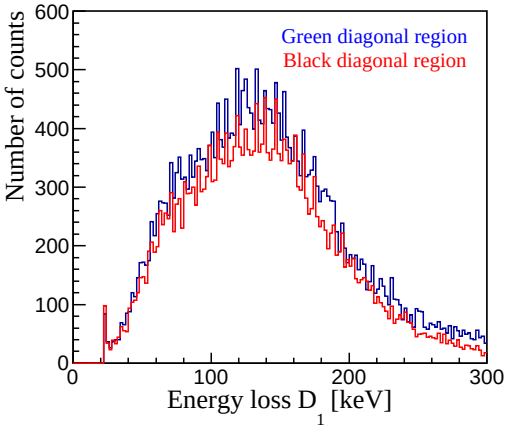

c) Energy loss of the events in D_1 inside the diagonal areas in figure 7.2 a)

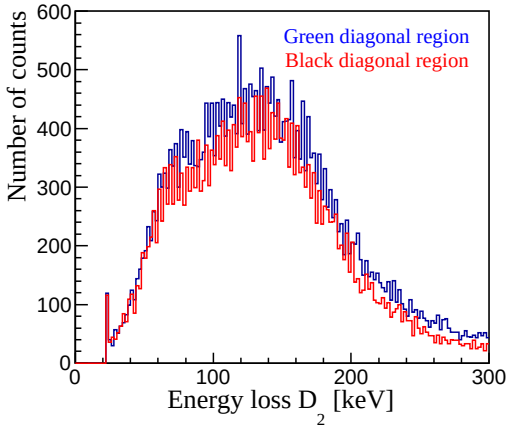

d) Energy loss of the events in D_2 inside the diagonal areas in figure 7.2 b)

Figure 7.3: Energy loss of the events in the two green areas (blue spectrum) and the black area (red curves) of figure 7.2 divided in the left and right arm. The regions cover the equal area size each.

the requirement to stop the δ-electrons efficiently, i.e., it exhibits high stopping power[2] and to cause small angular straggling of the protons.

Table 7.2 compares three exemplary materials as protective films with the same surface densities as the silicon sheet. Shielding materials with high densities, like gold, can be thinner to reach the same stopping effects. However, the relative lower stopping power must be compensated. They also induce higher angular straggling of the protons and hence they are less suitable for our purpose. The usage of lighter materials like carbon have the advantages of higher stopping power and lower angular straggling. Furthermore, thinner foils might be sufficient due to the increased stopping power. Carbon foils with different thicknesses are available and it is therefore a suitable alternative to silicon foils.

[2]Stopping power means the average loss per unit path length

Table 7.2: Comparison of different shielding materials. The stopping power refers to the complete energy loss of electrons with the kinetic energy of 100 keV, calculated by estar [90]. The material thicknesses correspond to the surface density of 100 µm silicon. The additional angular straggling $\sigma(\theta_{op})$ of the opening angle and the excitation energy resolution σ_{Exc} were simulated with Geant4 simulations.

Material $0.233\,\mathrm{g/cm^2}$	Stopping power [MeV cm^2/g]	$\sigma(\theta_{op})$ [mrad]	σ_{Exc} [keV]
Carbon	3.7	1.57	452
Silicon	3.3	2.43	697
Gold	2.0	4.23	1318

Alternative approaches instead of the additional foils are optional thin plates with negative surface charge and electric field strength E. They decelerate and repel the electrons. Very thin glass plates already may do the job due to their high resistivity and a charging up by the low energy tail of the δ-electrons. Due to the large difference of kinetic energy of a factor 1000 the effect on the protons will be small. Another option would be a magnetic field perpendicular to the detector plane. Such a configuration may be used to bend the electrons while the protons with large momenta still pass nearly straight.

7.3 LH_2 Target

The usage of polyethylene targets populates a large variety of final states by reactions with the carbon nuclei in the target composite. Only in combination with additional measurements using a pure carbon target this background could be subtracted. Using liquid hydrogen (LH_2) targets instead, this kind of background reactions will not occur.

Due to the low cross sections of later fission experiments the LH_2 targets need a minimum in thickness to gather sufficient statistics in a reasonable beam time. In table 7.3 the effect on the resolutions for an exemplary 9 mm thick LH_2 target with havar®[3] windows of 19 µm thickness was simulated using a Geant4 simulation: The emitted protons from the QFS $(p, 2p)$ reactions undergo higher multiple scatterings in the material which leads to an overall broadening of the expected resolution. Also the energy loss of the beam particles in the target becomes increasingly relevant and hence the distance up to the reaction point needs to be taken into account, e.g. by energy loss calculations using ATIMA. The origin of reaction is precisely known by the vertex reconstruction through the silicon tracker.

Thicker targets do not just have the disadvantage of producing higher angular straggling but the emission of δ-electrons increases, too. In the first order the

[3]High Strength Non-Magnetic Alloy Foil

Table 7.3: Contributions of the uncertainties of relevant devices on the opening angle $\sigma(\theta_{op})$ or TOF σ_{TOF} and the excitation energy σ_{Exc}. Where the effects are below the detection limit "-" is set.

Component	$\sigma(\theta_{op})$ [mrad]	σ_{TOF} [ps]	σ_{Exc} [keV]
Target 100 µm CH_2	0.69	-	249
Target 9 mm LH_2	2.79	-	846
Silicon det. pitch=100 µm	0.60	-	196
Silicon det. thickn.=100 µm	1.95	-	580
Silicon det. thickn.=50 µm	1.30	-	395
δ-ray shield	1.57	-	452
Materials btw. target and hodoscopes	-	10	132
TOF 1.0%	-	120	676
TOF 0.7%	-	85	496

emission probability increases linearly with the energy loss in the material [77]. In the case of future experiments with heavy elements the energy loss in the LH_2 target including the entry and exit windows is even four times larger than in the used polyethylene targets. Although a part of the δ-rays will be stopped inside the thick target, the results in section 7.2 showed that even the 100 µm thick target foils (comparable to the LH_2 window foils) limited the track reconstruction.

In summary, the angular straggling in the LH_2 target and in the δ-ray shielding results in an increased resolution of the opening angle to almost $\sigma(\theta_{op}) \sim 4$ mrad (compare the geometric mean of $\sigma(\theta_{op})$ in the components in row 3, 4, 5 and 7 in table 7.3), meaning an increase of the excitation energy resolution to σ_{Exc}=1.3 MeV.

7.4 Improvements

The resolution of the $(p, 2p)$ setup reaches its limits when the change of the target and the protective films will be installed. Furthermore, the current setup showed especially weaknesses in the possibilities to calibrate the TOF. The combination of modifications on hardware site (see sections 7.4.1 and 7.4.2) and new approaches for adequate calibrations (see sections 7.4.3 and 7.4.4) will compensate the increased resolution caused by the angular stragglings, discussed in the previous two sections.

7.4.1 Silicon Tracker

Three sources determine the angular straggling of the protons: The target, the δ-ray shielding and the first layers of the silicon tracker. While the target thickness and the shielding materials are determined by the constraints of demanding

high statistics and preventing background signals, the silicon layers have no such limitations.

As discussed in section 5.2 the pitch size of the detectors has small influence on the resolution in contrast to the wafer thickness (see also table 7.3, *Silicon det. thickn.=100* µm). An advanced development of the silicon detectors took already place during this thesis where the thickness of one half of the wafer surface (Type A) could be reduced to 50 µm to lower the multiple scattering for low energetic protons at large polar angles. Protons with high kinetic energies and small polar angles still punch through the wafer at a thickness of 100 µm (see the schematic drawing of the first layers in figure 7.4).

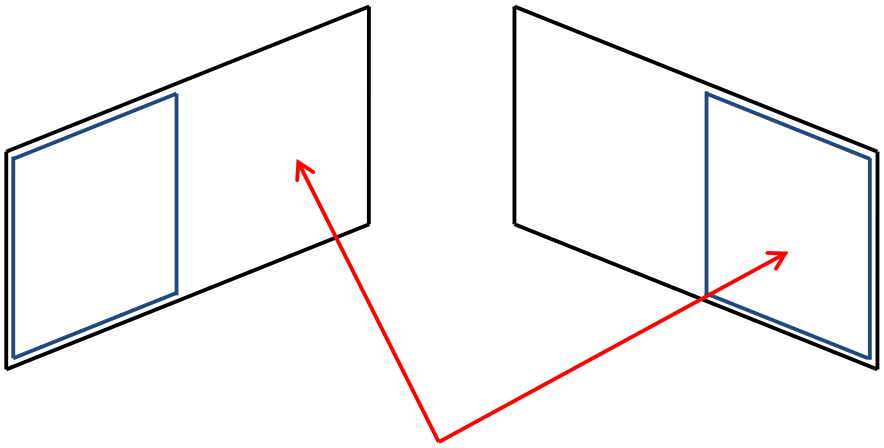

Figure 7.4: Schematic drawing of new first layers in the silicon tracker. The wafer borders are drawn in black. The blue marked area represents the silicon surface with a thickness of 50 µm at larger horizontal angles. Two protons from the $(p, 2p)$ reactions are illustrated by the red arrows. The left proton has a small polar angle with a typically low energy loss and small angular straggling in the silicon detector while the right proton with large polar angle exhibits higher energy loss and therefore higher multiple scattering, compensated by the thinner wafer material.

Compared to the current silicon detector unit L1, Geant4 simulations show a reduction of the angular straggling by $\sigma(\theta_{op}) = 0.65$ mrad (see table 7.3, *Silicon det. thickn.=50* µm). Careful studies are planned to measure the noise levels and its dependency on the two areas. The threshold for the readout electronics might be lowered and increases the amount of data. Yet, not considered is the effect of the film-like wafer and its bending on the position accuracy of the strips.

7.4.2 Hodoscope Setup

Beside the minimized angular straggling the second effort to keep the resolution of the excitation energy under control is the decrease of the TOF resolution. It will be advantageous to connect the improvement with the establishment of a new calibration procedure (see the subsequent discussion in section 7.4.3). Using the current hodoscope arms figure 7.5 shows an extended setup with the same

plastic scintillators behind the existing ones but offset by half. The twice time measurement of the protons improves the time resolution by $\sqrt{2}$. With the experimental determined resolution in section 4.3.4 (see equation (4.15)) this means a new timing resolution of $\sigma^{TOF} = 85\,\text{ps}$. Compared to the present TOF setup an improvement of the excitation energy resolution of σ_{Exc}=180 keV can be constituted (see the last two rows in table 7.3).

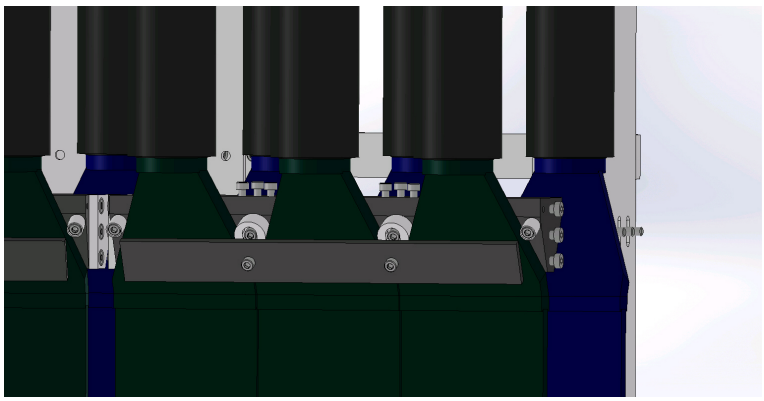

a) View from the side to one bundle of three petals of TOF detectors with the additional installation of a second row (in blue).

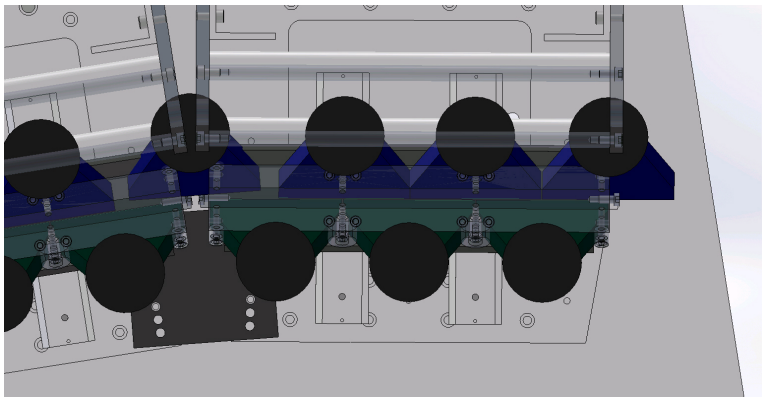

b) View from above. The second row of TOF detectors is mounted close to the origin rods with an offset by half. The gaps between the bundles of three TOF detectors are closed.

Figure 7.5: 3D sketch of a second row of TOF detectors (in blue) placed behind the present TOF petals (in green). Protons from the QFS $(p, 2p)$ reactions punch through the first petals and deposit energies in both rows.

The installation of the new silicon detector units L1 and the second row of TOF detectors will improve the overall resolution of the excitation energy to

$$\sigma_{Exc}^{new} = 1.2\,\text{MeV} \tag{7.3}$$

close to the goal value of $\sigma_{Exc} = 1.0\,\text{MeV}$ discussed in section 2.1. In comparison to the current $(p, 2p)$ setup the presented modifications balance out the

increased resolution due to the installation of the LH_2 targets and the δ-ray shielding partly.

7.4.3 New TOF Calibration

The TOF calibration suffered from several difficulties in the single steps of the calibration procedure (see the discussion at the end of section 4.3.4). Especially the high sensitivity on the fit functions on the walk and slew corrections of fast protons resulted in left tails in the peaks of the excitation energy spectrum (see figures 6.10 c) and d)). Subsequent empirical modifications were necessary which were based on the excitation energy spectrum of ^{15}N (compare figures 6.9 a) and b)).

This kind of retroactive corrections are not possible in the case of unknown excitation energy spectra. We therefore develop a new calibration procedure by exploiting the signal information in the second row of TOF detectors and proton beams, provided before the experimental physics runs. By carrying out the TOF calibration exclusively by protons we get rid of any effects coming from the different interaction mechanisms of the photons and protons. This will avoid systematic errors, fix the walk corrections and enables clearer HODO triggers. In addition the differential and integrated non-linearities should be calibrated with extreme care [54].

Pure proton beams have the advantage that the projectiles scatter with the free moveable hydrogen targets elastically. This process is conservative in energy and hence the sharp energy-angle correlation is valid (see equation (1.6)). The proton energies are determinable by the silicon trackers with an energy resolution of $\sigma_{Eny} < 1\,\%$ and can be transferred into the TOFs. Using well-defined various beam energies, this makes an absolute TOF calibration possible over a wide energy range under the same angles. The method replaces the determination of the time offset and the walk correction by the photons. Since the TOFs of the protons are determined independently by the silicon tracker the slew corrections at high energy deposits in the TOF detectors can be omitted.

The time resolution can be refined by a variation of the current method of the slew correction (see section 4.3.3) where all protons in the two TOF detectors in a row can be used instead of restricting the selection to protons punching through two neighboring TOF detectors. Each proton with the velocity β>0.25 (compare figure 6.3) will be measured twice in the two rows and, due to the offset by half, all scintillators will be related to each other as the gaps between the bundles of three detectors are covered.

Finally, the second row can act as clean HODO trigger since it is shielded from low energetic charged particles which are stopped in the first row.

7.4.4 Alignment of the Silicon Tracker

A sophisticated system of foils and fibers made it feasible to determine the positions of the silicon detectors with the required precision. Using the LH_2 target this possibility of self-calibration is omitted. The photographic analysis as the second option is extremely sensitive to systematic errors. However, we calculated that even small misaligned silicon detectors can lead to significant offsets of the excitation energy spectrum (see table 5.2).

To continue the established position alignment procedure (see section 5.4) attached fiber targets in vertical direction on both ends of the LH_2 target frame would provide the required number of calibration points (see figure 7.6). In addition to that one silicon detector of type L1 could be placed in front of the LH_2 target frame. In this case the determination of the positions of the silicon detectors is conducted by cosmic rays punching through the layers in each arm and through the center silicon detector (shown by the red arrows in figure 7.6 b)) without straggling effects.

The center silicon detector will also determine the x-position of the beam particles with higher accuracy than the BDC did and due to the small multiple scattering of the high velocity beam[4] a resolution of the vertex reconstruction in the order of the pitch size, i.e., 100 µm would be achievable. The vertex reconstruction of the z-position will be further on examined by the emission of the two protons.

A similar setup of in-beam silicon detectors was recently successfully tested in the NP1306-SAMURAI19 experiment with light beam particles (^{8}He with an intensity of $1 \cdot 10^5\,s^{-1}$) at the SAMURAI area in the RIKEN Nishina Center [91]. Despite the high beam intensity the silicon detectors in beamline showed only a slight increase of dark current and ran stable.

[4]For example, the angular straggling of Pb-isotopes with E_{beam}=250 MeV/u is $\sigma_{ang} <$ 0.6 mrad through the silicon detector and 9 mm LH_2 target.

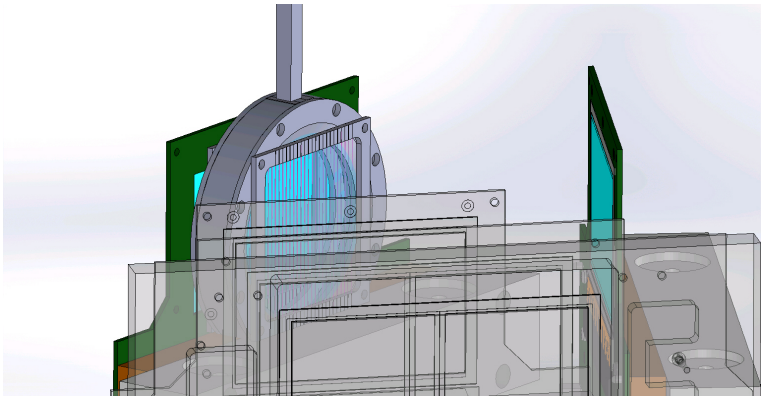

a) View to the target center with 9 mm thick LH_2 target, fiber targets and a new silicon detector.

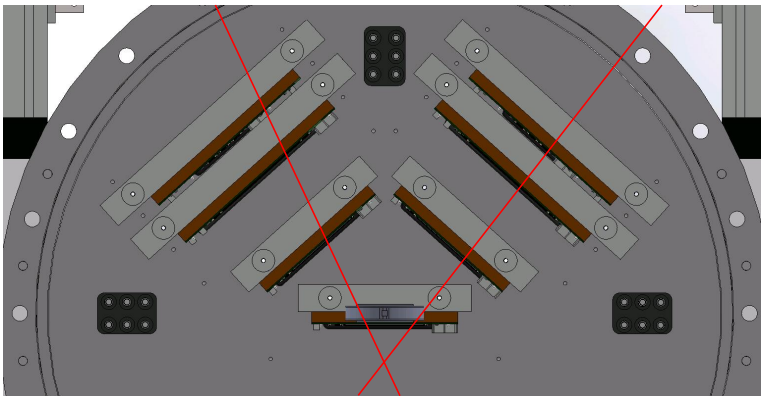

b) View from above: The red arrows illustrate cosmic rays which punch through the single arms and the center detector.

Figure 7.6: 3D drawing of the target area with the silicon tracker and the modified target area with LH_2 target, fiber targets and silicon detector in beam line.

Appendix A

Appendix

A.1 Used Formulas

A.1.1 Modified Walk Correction

The dependency of the time measurement on the light output was compensated by the walk- and slew correction (see section 4.3.3). Due to the small statistics of proton signals usable for the slew correction the time correction was conducted by photons in the low light output region. The walk corrections using the photons might not be adapted to necessary corrections for the proton since the reaction mechanisms of the particles in the plastic scintillator are different (see also the discussion in section 4.3.4).

Left tails and smeared out peaks in the excitation energy spectrum of ^{15}N could be attributed to underestimated TOFs, especially for TOF<12 ns. In this region the time depends strongly on the walk correction. Better results could be obtained by the empirical corrections of small TOFs adding an additional time,

$$TOF_{new} = TOF_{old} + \frac{1}{2}(12\,\text{ns} - TOF_{old}), \tag{A.1}$$

applied to $TOF < 12$ ns in all TOF detectors. The TOF of the fastest protons is ~ 10 ns and hence, the maximum shift is 1 ns.

A.1.2 Fit Function in the Excitation Energy Spectrum

The peak shapes of the excitation energy spectra (see figures 6.10 c) and d)) are best described by Gaussian fit functions including left tails, i.e.,

$$f(x) = a_1 \cdot e^{-\frac{(x-a_2)^2}{2\cdot a_3^2}} + \frac{a_4}{2} e^{\frac{x-a_2}{a_5 \cdot a_3}} Errfc(\frac{x-a_2}{(a_3+1)/2a_5}) + \frac{a_6}{2} Errfc(\frac{x-a_2}{a_3}) \tag{A.2}$$

where the same width a_3 is used in the three peak. The meaning of the parameters are outlined in table A.1.

Table A.1: Meaning of the parameters of the fit function (see equation (A.2))

Parameter	Meaning
a_1	Amplitude
a_2	Maximum of peak
a_3	Width of peak (in sigma)
a_4	1. Relative amplitude of left tail
a_5	Slope of left tail
a_6	2. Relative amplitude of left tail

A.2 Efficiency

This section lists the individual efficiencies of the detectors and the gates. Furthermore, the live-time of the DAQ for the actual trigger rate is necessary to calculate the total efficiency of the present setup.

A.2.1 Plastic Scintillators

The intrinsic efficiency of the plastic scintillators in the SBTs, hodoscope arms and PID detector array could not be measured. However for charged ions with energy losses far above the PMT thresholds it is justified to assume an intrinsic efficiency of

$$\epsilon_{Scint} = 100\ (2)\,\%. \tag{A.3}$$

A.2.2 BDC

The drift time spectrum in the experimental runs revealed signals in unphysical time regions (see figure 4.2 b)). Events with such signal structure cannot be used to reconstruct the particle positions of the beam. Hence, we restricted the analysis to events where the BDC provides a well defined vertex in the target area in agreement with the position from the silicon tracker. Under this condition

$$\epsilon_{BDC} = 64.5\ (43)\,\% \tag{A.4}$$

of the events remained (compare the green gate in figure 6.2).

A.2.3 Silicon Tracker

A detailed description of the determination of the silicon tracker efficiency can be found in [46] and here just the major concept is summarized for completeness. The efficiencies of the third layers D5 and D6 are obtained by the ratios of the number of tracks in the first two detectors, traced back to the target area, and the number of events in the corresponding third layer. By requesting proton tracks in one arm, signals in the opposite third layer and the nitrogen residue in the PID detector array signals in the first two layers of the second arm must theoretically always exist. The proportion of measured signals in the detectors each exhibits the efficiencies of the first two layers D1-D4 (see table A.2, second column).

The efficiencies are close to 100% for the silicon detectors in the first two layers and lower values are obtained in the case of the third layers. The drop can be explained by the coverage of the solid angles of the silicon detector units D5 and D6 which is 83.5% compared to the detectors of the second layer. Particles hitting the edges of the first two layers cannot be detected by the third layer. Taking the lower coverage as reference system in the third column the efficiency of D5 is comparable to D1-D4 whereas the efficiency of D6 drops by 1/6 since the lowest chip was broken resulting in a 1/6 less active area.

Table A.2: Silicon detector efficiencies *from* [46]. The efficiencies in the second and third column differ with respect to the taking into account the spatial coverage of the third layers.

Detector	Efficiency [%]	Corr. Efficiency [%]
D_1	99.8 (1)	99.8 (1)
D_2	97.9 (1)	97.9 (1)
D_3	99.9 (1)	99.9 (1)
D_4	99.7 (1)	99.7 (1)
D_5	83.6 (1)	∼100.0 (1)
D_6	71.5 (1)	83.3 (1)

Due to the breakage of detector D_5 during the experimental runs the vertical hit positions of protons in the left-armed TOF detectors were used instead (with the intrinsic resolution in equation (A.3)). Hence, the efficiency of the silicon tracker is the product of the single efficiencies of the first two layers D1-D4, detector D6 and the left hodoscope arm, i.e.,

$$\epsilon_{Sili} = \epsilon_{D1} \cdot \epsilon_{D2} \cdot \epsilon_{D3} \cdot \epsilon_{D4} \cdot \epsilon_{Scint} \cdot \epsilon_{D6} = 81.0\,(2)\,\%. \tag{A.5}$$

A.2.4 Total Setup Efficiency

All presented efficiencies are embedded in the live time of the DAQ-system. At the beam rate of $4 \cdot 10^5$ particles per spill during the experiment a live time of

$$\epsilon_{LT} = 60.1(0)\,\% \tag{A.6}$$

was determined by the ratio between accepted and requested trigger rates. The total efficiency of the setup is calculated from the live time ϵ_{LT}, the spatial coverage of the QFS $(p, 2p)$ kinematics (see equations (2.5) and (A.11)) and the detector efficiencies (see equations (A.3), (A.4) and (A.5)) to

$$\epsilon_{P2P} = \epsilon_{LT} \cdot \epsilon'_{Cov} \cdot \epsilon_{Scint} \cdot \epsilon_{BDC} \cdot \epsilon_{Sili} = 1.7\ (3)\%. \tag{A.7}$$

A.3 Additional Event Selection

A.3.1 Cut on TOFs

This work presented several physically motivated cuts and gates to select events of QFS $(p, 2p)$ reactions (see chapter 6). Furthermore, we showed on the example of the x-positions of the reaction point determined by the BDC and the silicon tracker the usage of redundant information to cut inconsistent events (see section 6.1). Here, we present two more constraints on the events which where mentioned but not explicitly shown in the main text.

The first cut is applied to events with two fast protons. The high sensitivity of the TOF on the walk correction makes these events particularly faulty (see the discussion in section 4.3.4) and hence events needed to be neglected where the summed TOF is smaller than 25 ns. By comparing the number of QFS $(p, 2p)$ reactions (see figure 6.10 d)) with and without the cut,

$$\epsilon_T = 82.4\,(45)\,\% \tag{A.8}$$

of the events remain. The cut affects events of the three states equally and has therefore no influence on the distribution of the ground and excited states.

A.3.2 Gate on coincident Y-Positions

The low multiplicities of the first two layers make it likely to choose the correct cluster as coming from protons (see section A.4.3). In the case of the third layers the multiplicity increased and the cluster with the highest energy loss was taken. Similar to the comparison between the reconstruction of the reaction points using the BDC and the silicon tracker (see section 6.1) this gate uses the redundant information of the hit positions in y-direction of the third layer of the silicon tracker and of the TOF detectors to cut non-consistent events. Events where the

normalized vertical flight direction from the reaction point to the third layer is largely different from the normalized vertical flight direction from the reaction point to the TOF detectors are discarded.

Most of the events are inside the linear correlation (see the green gate in figure A.1). The width corresponds to the expected multiple scatterings and detector resolutions. Events outside the marked area can also stem from QFS $(p, 2p)$ reactions but either the wrong cluster was taken in the third layers or the protons experience hard-knock scatterings in the air and are strongly deflected. In both cases either the opening angle or the TOF is deteriorated and worsens the resolution of the excitation energy. The here presented second gate in figure A.1 includes

$$\epsilon_Y = 82.5\,(45)\,\% \tag{A.9}$$

of the events. This kind of gate could not be set on the left arm since the third layer of the silicon tracker was broken shortly after the begin of the experimental runs.

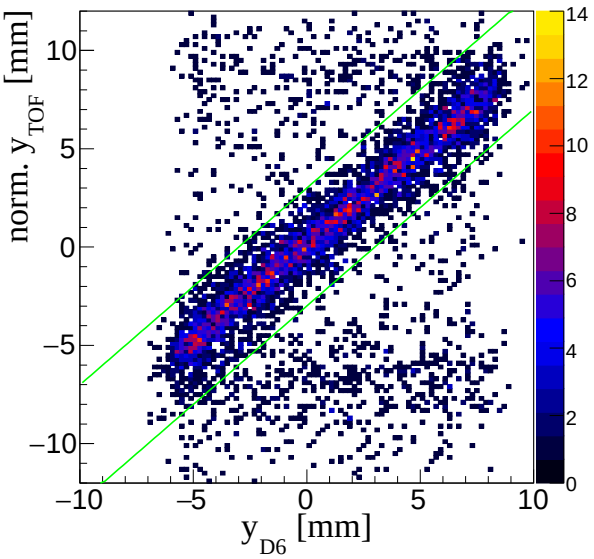

Figure A.1: Measured y-positions of the protons in the silicon detector unit D6 and the normalized y-positions of the TOF detectors. The green borders set the gate to consistent y-positions. The left empty part corresponds to the vacant events in the broken APV25-chips.

The effect of wrongly assigned proton tracks in the y-direction of one arm was also implemented in the Geant4 simulation (see figure 6.8). The randomly set y-position leads to a spread of events in the excitation energy which is responsible for the events between the two dominant peaks and the non-perfect Gaussian fit (see figure 6.8 a)).

A.3.3 New Spatial Coverage

The spatial coverage of the $(p, 2p)$ setup ϵ'_{ST} was determined by the dimensions of the third layers of the silicon detector (see equation (2.3)). In the analysis the experimental runs with broken left third silicon layer were used. The left hodoscope arm was used to determine the y-position of the emitted protons. Therefore the spatial coverage of the hodoscope arm defines the new spatial coverage of the $(p, 2p)$ setup ϵ'_{ST} to

$$\epsilon'_{ST} = 2.0\,\%. \tag{A.10}$$

Taking the changed setup configurations into account the proportion of quasi-free scattered protons within the detector coverage increases to

$$\epsilon'_{Cov} = 3.9\,\%. \tag{A.11}$$

A.4 Additional Information of the Silicon Tracker

A.4.1 Design Differences of the Silicon Detector Units

The basic design of the three different silicon detector units (see figures A.2 a)-c)) follows each the requirements of thermal shielded silicon wafers, ASIC-chips close to the silicon wafers and connectors directed downwards such that the cables are vertically connected to the feedthroughs on the bottom of the chamber (see further requirements in section 2.2.1). While the design was described in details with aid of detector unit L1, special features of the units L2 and L3 missed out.

Two wafers next to each other are mounted in the units L2 and L3 with the short side on the bottom. Along the edges the wafers are glued on ceramic frames with one bar in the middle dividing the window into two. This had the purpose to stabilize the wafer but it was also mandatory during the production of bonds connecting the two wafers in the unit L3 where a certain pressure is needed to fix the bonds on the wafer. Without a flat and stable surface the wafers would break.

Detector unit L2 has two Type B wafers with the strips along the long edge. The APV25-chips are therefore placed below the wafer and the wire and connector arrangement is the same as in detector unit L1 (see figure A.2 b)). In the case of detector unit L3, Type A wafers were used where the strips are in horizontal direction (see figure A.2 c)). Since the spatial resolution of 200 µm in y-direction was sufficient, two neighboring strips and strips between the wafers were connected. This reduced the number of channels from 1536 to 384 for each detector unit L3. In order to prevent the signals from additional noise the ASIC-chips were mounted sidewards next to the pitches. Three APV25-chips were mounted on both sides in alternate order. Since the feedthroughs need to be installed at

the bottom the connectors on the silicon detector unit L3 were put downwards like it was done for the units L1 and L2.

A.4.2 Baseline Restorement

In order to convert the analog signal to a digital value (ADC values), the charge is sampled with respect to a constant reference systems in the form of stable grounds. However, the APV25-chip suffers from floating ground in the input channels and hence, baseline corrections are necessary. The principle of restoring the baseline (executed in the ADCM modules) will be illustrated with five neighboring input channels of the APV25 chip. Three of them are connected to the detector (labeled with "O") and two of them are not bonded ("X"). Before the experimental runs start, pedestal runs set the peak of the normal distributed noise level to zero (see figure A.3 a) and figure A.4 a) and b)).

The charges of the hit strip are collected by the APV25 chips (see the center channel in figure A.3 b)). Since the grounding is sensitive to the incoming charge the zero of that channel but also of the neighboring ones arbitrarily drops down [92]. Using the initial zero as reference the signal strength would seem to be smaller than in reality (compare the red and green arrows in figure A.3 b)). In the restorement process the averaged difference of the current signal drop and the initial baseline in the two neighboring unbonded channels is added to the signal height in the bonded channel (see figure A.3 c)). The original signal height in the center channel is thus restored.

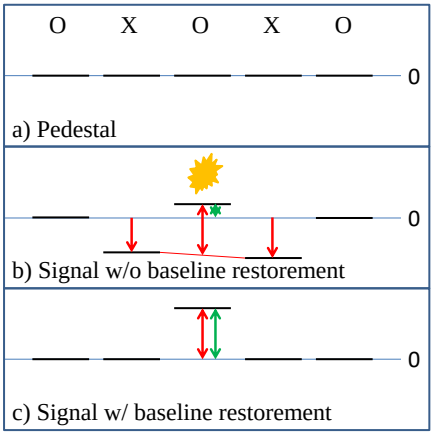

Figure A.3: a) shows five channels in the normal mode without an event. The energy here is set to 0. In b) the case is shown what happens to the neighboring channels if one (the third) channel is hit. The restorement lift the channels back to 0 and the full strength of the signal is recorded in c).

The floating ground is expressed by the drop of the baseline when charge is collected but also by a non-constant baseline at any time in all channels. Each signal is superimposed by the floating ground. If, e.g., the 128 channels of the

APV25 chip are unconnected they exhibit the same noise level of σ_{APV}=2 keV in the pedestal corrected raw mode (see the projection in figure A.4 b)). Advanced shape analysis using every second channel determines the average noise level and defines this value as the actual ground level. The subtraction of floating effects decreases the noise level to σ_{APV}=1.3 keV (see the projection in figure A.4 d)). The information of the signals in the unbonded channels is fully processed in the ADCM modules and hence it is not necessary to transfer them to the event-builder (see figure A.4 c)) which reduces the amount of sent data.

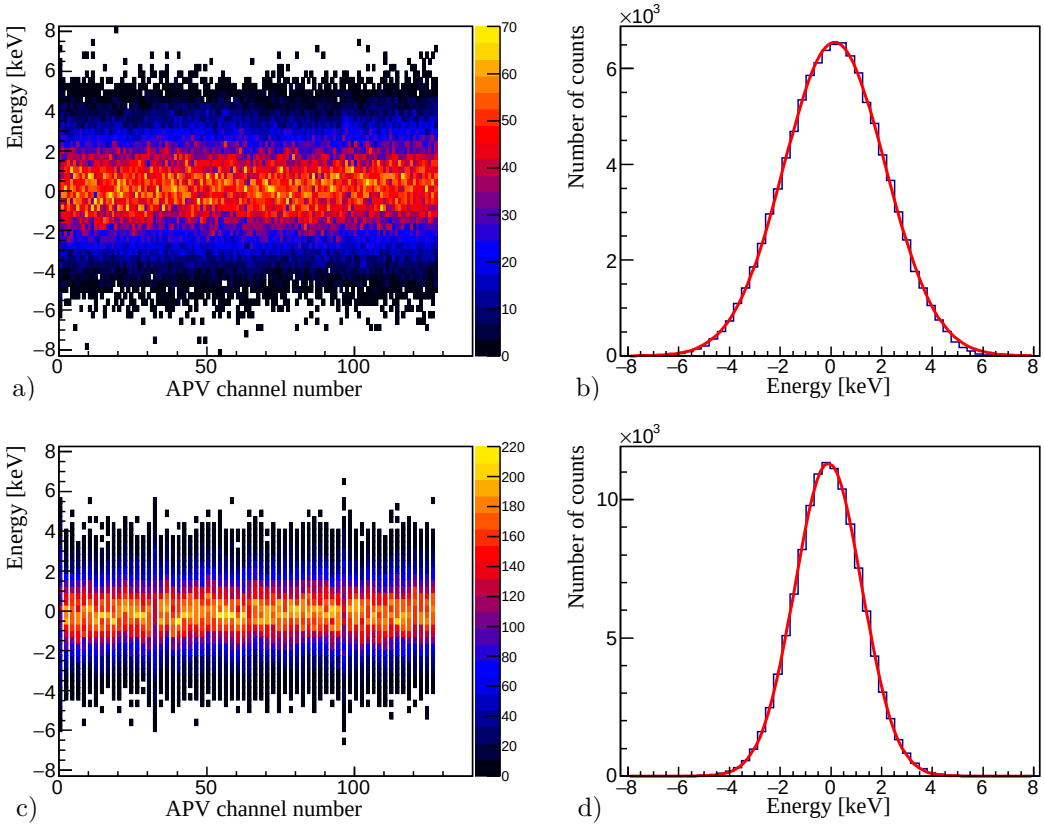

Figure A.4: The noise distribution of the APV25 chips without input signals, i.e., the channels are unbonded. The noise distribution of the 128 channels each is the same and Gaussian shaped (see a) and b)). In the normal mode each second channel is used as reference (see c) where half of the channels disappeared). The floating ground can therefore be taken into account and the noise distribution is smaller (compare b) and d)).

Further size reduction of the data packages is achieved by cutting signals located in the noise region. In the experiment signals $< 3\sigma_L$ were omitted and not transmitted to the DAQ machine. Figure A.5 shows the ADC values of signals above the threshold in the three types of detectors in experimental runs. The zero of the ADC values was set to 2^{13} due to bit-shift operations in the ADCM modules.

The additional noise σ_{WAF} coming from the silicon wafers is determined by the subtraction of σ_{APV} from the total noise σ_L,

$$\sigma_{WAF} = \sqrt{\sigma_L^2 - \sigma_{APV}^2} \tag{A.12}$$

where σ_L is one third of the distance between the two black solid lines in figures A.5 a)-c).

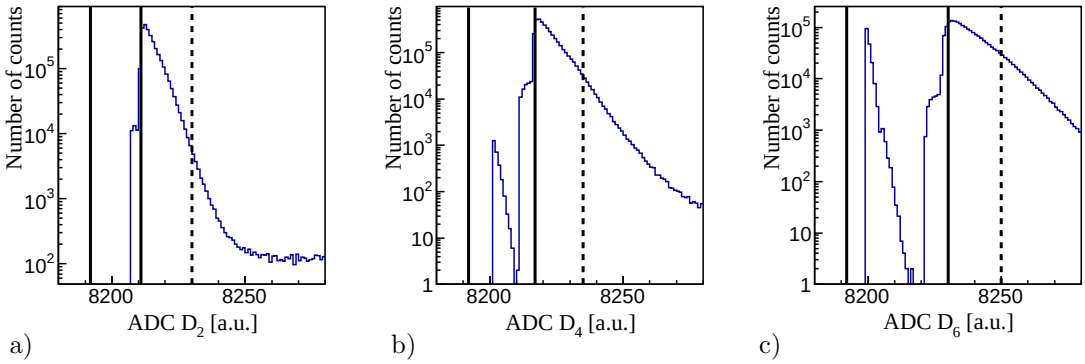

Figure A.5: Applied noise suppression using a threshold of $3\sigma_L$ in the experimental runs. Depending on the noise level of each silicon detector unit the absolute value of the threshold is different (see the different values of the right black line in the three detector units in a), b) and c)). The left black borders mark the zero of the ADC channels, shifted by 2^{13}=8192. Signals below the black marked threshold come from unbonded channels (in the silicon detector unit L2, see b)) and from a switched off APV25 chip (in the detector D6, see c)). The noise level of them corresponds to the blank APV25 chip (see figure A.4 d)) and is therefore lower.

The data traffic taken with this mode drops from 17 kByte/s to 120 Byte/s (see section 2.2.1). This is well below the maximum package size of 10 MByte/s limited by the DAQ system.

A.4.3 Cluster Multiplicities

Several signals in the silicon detectors increase the combination possibilities between the hits of the detectors. It will become very complex and, in some cases, impossible to identify the correct hit pattern of the protons. It is therefore essential to avoid background and noise signals. On the other hand thresholds must not cut the relevant proton signals.

The signals of protons are much higher than the noise region (see section 2.2.1 and the signal-to-noise discussion there) and additional cuts by software were possible to further discard unphysical low signals (see the dashed lines in figure A.5) without loosing informational content resulting in decreased multiplicities in the silicon detectors. Most of the events in the first layers leave exactly one signal cluster[1] (see A.6 a)) and the mean multiplicity is M_{L1}=1.2. The picture

[1]Clusters are defined as the combination of signals in neighboring strips. One cluster can therefore consist of one or multiple signals.

is similar in the case of the second layer (see figure A.6 b)) where the multiplicity 1 still dominates but almost 1/3 of the events show at least a second cluster and the mean value increases to M_{L2}=1.5. The multiplicity distribution of the third layers (see figure A.6 c)) follows an exponential decay where more than 50 % of the events have a multiplicity higher than one. These detectors have the highest average multiplicity of M_{L3}=2.6.

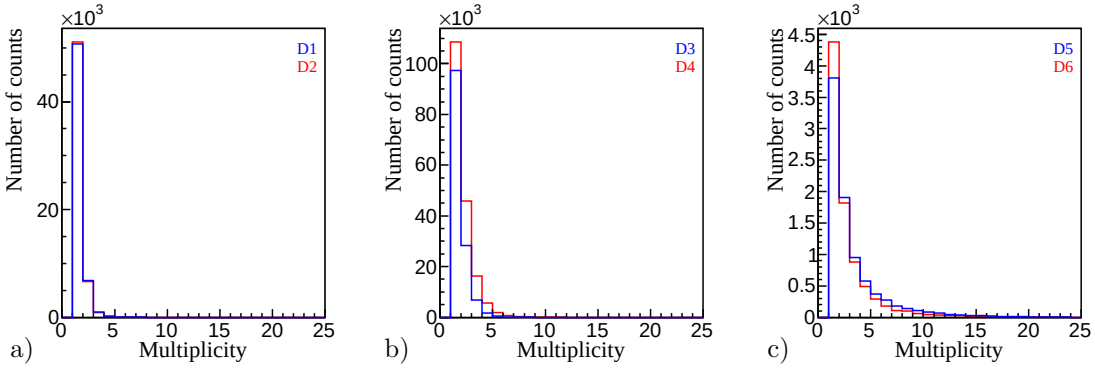

Figure A.6: Multiplicities in the two detectors of the three layers. From left to right the multiplicity of signal clusters are shown for detectors in the first, second and third layers (see a), b) and c)). At the end of the experiment the left detector in the third layer broke and was switched off.

Further redundant information of the proton hit positions in the TOF detectors are used to ensure consistent flight directions. With that cluster with a distance $\Delta s > 50$ strips are distinguishable. Considering the low multiplicities in the vertical detectors, the probability for two close clusters is $\sim 3\,\%$.

a)

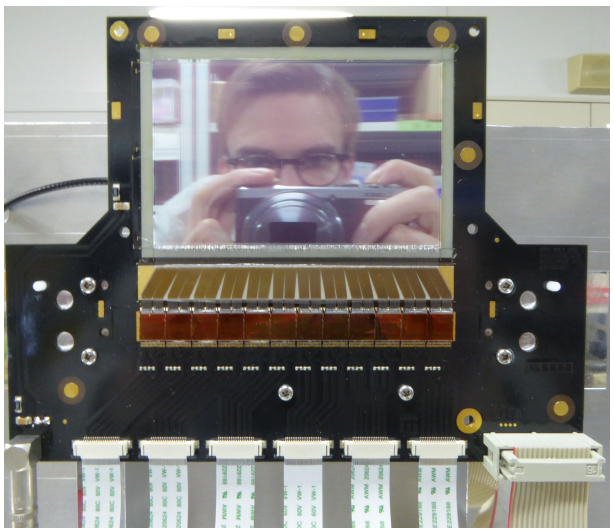

b)

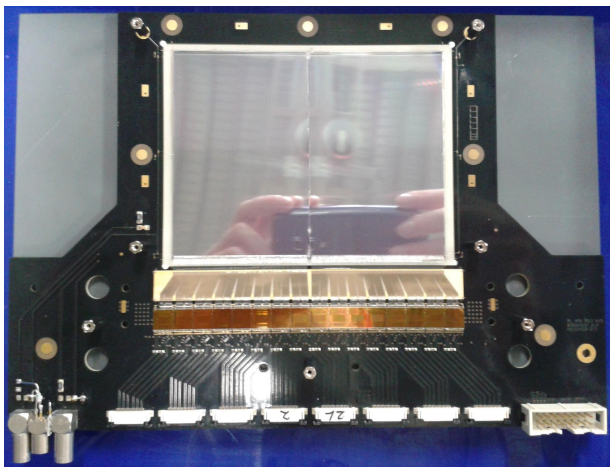

c)

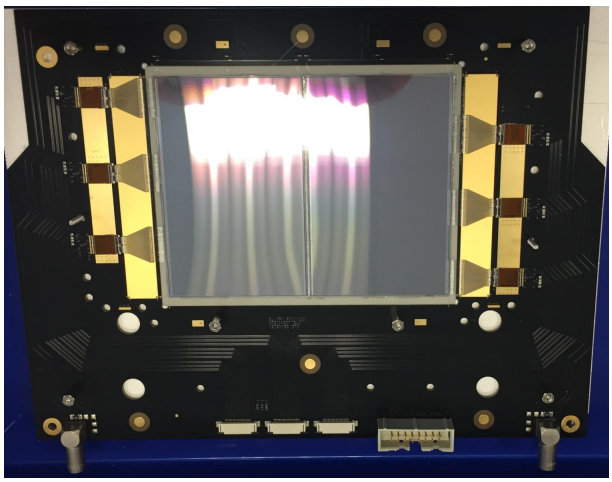

Figure A.2: Pictures of the three silicon detector units L1, L2 and L3 (see a), b) and c)). The slightly different requirements on the wafer sizes lead to different designs.

A.5 Position Measurement

A.5.1 Reflecting Markers

This section is an appendix to the optical measurement of the silicon detector positions (see section 3.3). The photogrammetry system was used to determine the position of the individual detectors with respect to each other by defining planes, distances and angles. Since the reflecting markers (in the following: grey reflecting markers, compare figure A.7) are randomly put on the devices shifts of the detector surfaces along the planes cannot be measured. However, these kind of shifts are relevant for the positions of the silicon detectors (compare table 5.2).

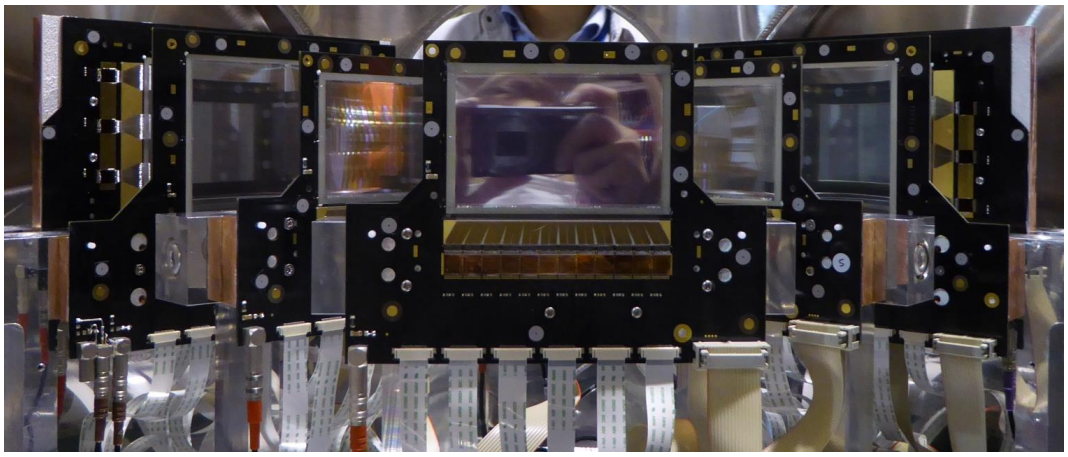

Figure A.7: Photo of the silicon tracker with an additional detector at center position from upstream. The PCBs of the silicon detector units have two types of reflecting markers. One kind of reflectors consists of chemical gold and was already implemented in the production with high position precision. The grey shimmering patterns are provided by the photogrammetry system and were placed randomly by hand.

In order to determine the absolute horizontal shifts of the detector, additional reflecting markers (consisting of chemical-gold) with high position accuracy of σ_1 (see table 3.2) were implemented on the PCB.

The photogrammetry system can recognize the gold markers under homogenous lightning, i.e., each silicon detector was photographed from top, disassembled from the setup (see the schematic top-view in figure A.8 a)). One technical aspect of the measurement is therefore the combination of the pictures of the assembled silicon tracker in the experimental room and the single shots. The positions between the grey reflecting markers and the gold markers were determined in these separate shots. Using the grey markers as reference the positions of the gold markers can be transferred into the full setup (see figure A.8 b)).

The horizontal shift along the detector surface between the center position of the plane and the position of the gold marker in the center of the detector is then associated to the absolute shift of the detector (see the red distance marker in figure A.8 b) and table 3.1, columns "shift").

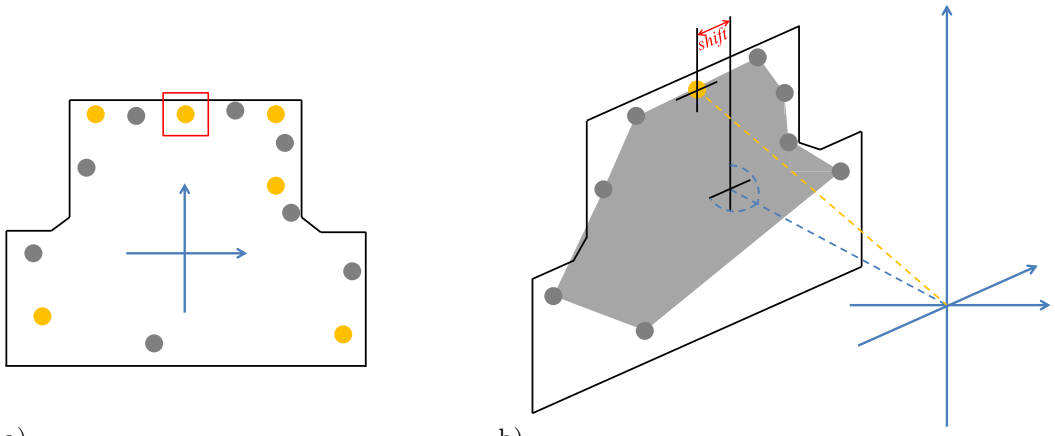

a) b)

Figure A.8: Schematic drawing of two types of reflecting markers on the silicon detectors. The yellow circles correspond to the implemented markers on the detector PCB, the grey circles are glued by hand and are provided by the photogrammetric system. In a first shot the position of the red outlined yellow circle (horizontal center of the silicon detector) was determined by the grey circles (see a)). Its position was transferred to the analysis when the silicon detector was assembled in the setup (see b)). The grey circles were used to generate a plane with which the distance and angles with respect to the zero of the coordinate system (see the blue arrows) was determined (see the dashed blue line). The difference between the yellow circle and the pass of the dashed blue line through the PCB corresponds to the shift of the detector along the PCB surface.

A.5.2 Theoretical Deviations of Limiting Effects on the Resolution

Geant4 simulations are a powerful tool to understand the effect of detector attitudes in the complex setup (see section 5.2). Theoretical deviations are nevertheless important to understand and cross-check the results of simulations. We therefore show the determination of values coming from two geometrical effects.

The influence of the pitch size on the resolution of the vertex reconstruction can be understood from the distribution of signals into the strips. Under the assumption that only one strip is hit in each event, four sharp positions in the vertex reconstruction in a distance of 100 µm each with the same probabilities are obtained (see the red bars in figure A.9).

Using the nomenclature of the parameters in figure A.9 the intrinsic resolution $\tilde{\sigma}_{int}$ in one arm is

$$\tilde{\sigma}_{int} = \frac{1}{\sqrt{12}}\text{atan}\theta = \frac{2}{\sqrt{12}}\text{atan}\frac{1/2\,\Delta r}{d_1 + 1/2\,d_2} = 0.43\,\text{mrad} \tag{A.13}$$

where the term $1/\sqrt{12}$ is the multiplier in order to convert the uniform distribution to normal distribution. Since both arms have the same limiting factor the

intrinsic resolution of the silicon tracker is the geometric mean of both arms, i.e.,

$$\sigma_{int}^{theo} = \sqrt{2} \cdot \tilde{\sigma}_{int} = 0.60\,\text{mrad} \tag{A.14}$$

in perfect accordance to the result from the Geant4 simulation (see equation (5.3)).

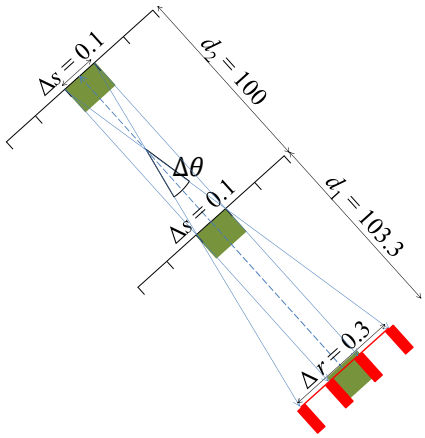

Figure A.9: Resized schematic drawing of the left arm with the relevant parameters Δs as the pitch size, $d_{1/2}$ as the distances between the target and first layer (d_1) and between first layer and second layer (d_2). The real particle track shows the dashed blue line. The red bars show the four possibilities where the vertex reconstruction locates the origin with the maximum distance of Δr. The units are in mm.

As a second example the effects of misaligned detectors are calculated. The self-calibration analysis (see section 5.4) takes into account two shifts along and perpendicular to the horizontal wafer direction. The horizontal angle θ is obtained by the arctangent from the difference s between the horizontal hit positions and the distance d between the detectors (compare figure A.10):

$$\theta = \text{atan}\frac{s}{d}. \tag{A.15}$$

Shifts δ_{shift} along the horizontal direction of the wafer contribute with a change of the horizontal angle of

$$\begin{aligned}\Delta\theta(\delta_{shift} = 100\,\mu\text{m}) = \theta - \theta' &= \frac{1}{s_{max}} \int_{-s_{max}/2}^{s_{max}/2} \text{atan}\frac{s}{d} - \text{atan}\frac{s + \delta_{shift}}{d}\, ds \\ &= -\frac{1}{s_{max}} \int_{-s_{max}/2}^{s_{max}/2} \text{atan}\left(\frac{\delta_{shift}}{\frac{1}{d}\left(s^2 + s \cdot \delta_{shift}\right) + d}\right) ds = 0.95\,\text{mrad}\end{aligned} \tag{A.16}$$

using the nomenclature in figure A.10 and s_{max}=76.8 mm as the wafer length and $d = 100$ mm as the distance between the two layers.

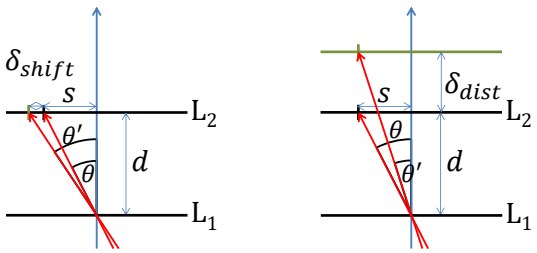

Figure A.10: Schematic top view of shifts δ_{shift} along the wafer surface (see a)) and shifts δ_{dist} in the distance between the silicon detectors in the layers L1 and L2 (see b)). The red arrows correspond to the reconstructed proton tracks from the hit positions in the two detectors. The horizontal angle with the correct silicon positions is labeled with θ. The horizontal angle θ' is obtained from the shifted detector in the layer L2.

The influence of small shifts δ_{dist} in the distance d changes the denominator in equation (A.15) marginal (see figure A.10 b)).

$$\begin{aligned}\Delta\theta(\delta_{dist} = 100\,\mu\text{m}) = \theta - \theta' &= \frac{1}{s_{max}} \int_{-s_{max}/2}^{s_{max}/2} \text{atan}\frac{s}{d} - \text{atan}\frac{s}{d + \delta_{dist}}\, ds \\ &= -\frac{1}{s_{max}} \int_{-s_{max}/2}^{s_{max}/2} \text{atan}\left(\frac{\delta_{dist}}{\frac{1}{s}\left(d^2 + d \cdot \delta_{dist}\right) + s}\right) = 0\,\text{mrad}\end{aligned} \tag{A.17}$$

The values of $\Delta\theta(\delta_{shift} = 100\,\mu\text{m})$ and $\Delta\theta(\delta_{dist} = 100\,\mu\text{m})$ are comparable to the values from the Geant4 simulations (see table 5.2). The differences with respect to the results from the Geant4 simulations stem from the non-varied reaction point. We also assumed the symmetric distributions of the protons along the center of the wafers (in horizontal direction). More advanced calculations would be necessary to take into account the beam spot size and the distribution of the protons in the QFS $(p, 2p)$ reaction at different excitation energies.

A.6 Additional Information on the Calibration of the SBT

A.6.1 Time Calibration

The time calibration of the SBT detectors was carried out by the time calibrator module Ortec 462 [70], using different time periods with a binning of 10 ns and a linear fit function. Figure A.11 shows the spectrum with the axis of the raw TDC values (in red) and the calibrated time (in black). Since the signals in the SBT detectors occur at a small range within the TDC channels it was sufficient to calibrate the first 40 ns (in comparison to the TOF detectors with a range of 90 ns).

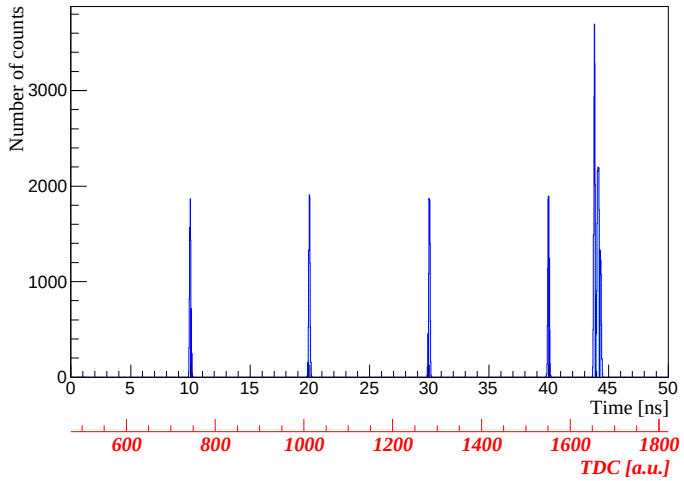

Figure A.11: Raw *TDC* values (in red) and the time spectrum (in black) in the left SBT1 using the time calibrator module Ortec 462 which provides signals with a period of 10 ns.

In table A.3 we listed the least significant bits (LSB) of the four TDC inputs used for the four PMTs of the SBT detectors. They are slightly different from the default value of 35 ps. Also they differ among each other showing the importance to calibrate each PMT independently.

Table A.3: Values of the time calibration of the TDC channels used for the SBT detectors.

	LSB [ps]
SBT 1L	37.13 (3)
SBT 1R	36.99 (2)
SBT 2L	37.68 (2)
SBT 2R	37.81 (4)

A.6.2 New Time Resolution using the Beam ^{132}Xe

The change of the beam from oxygen to xenon in the last day in the campaign made a new QDC-calibration necessary for the SBT detectors. Since the energy loss of the heavier beam ^{132}Xe is higher than that of ^{16}O the QDC values increased and the gains of the QDC modules were lowered. Similar to the previous spectrum of the light beam projectile (see figure 4.1 a)) two circular shapes occur where the left maximum contains most of the events (see figure A.12 a)). This region is identified as the primary ^{132}Xe beam. Events stemming from this gate are selected and used in the analysis (see section 7.2).

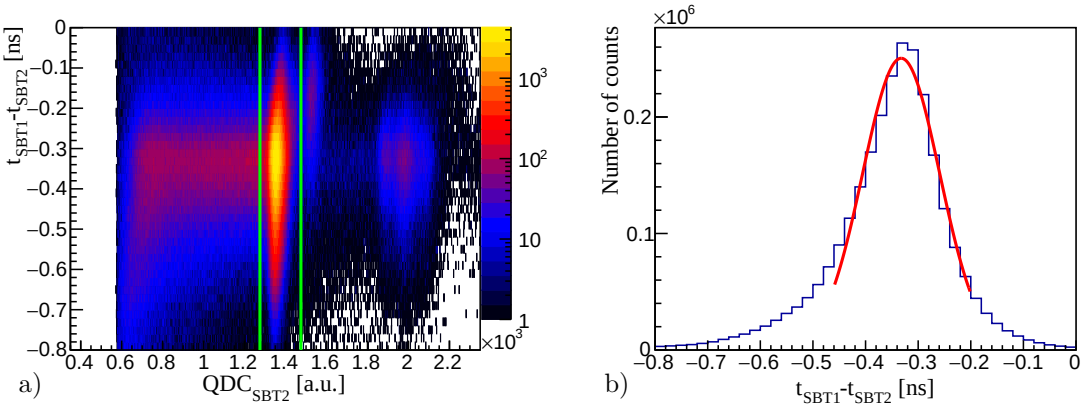

Figure A.12: The left spectrum a) shows the time difference between the SBTs plotted with respect to the mean charge of SBT2. Two circular maximum at QDC_{SBT2}= 1350 and 2000 with the same mean value for the time difference Δt appear. The highest number of events are in the left maximum which is related to the primary ^{132}Xe beam (marked with green gates). The fit on the y-projection (see b)) of this region exhibits the time resolution of the beam trigger.

Fitting the distribution in figure A.12 b) with a Gaussian fit function the time resolution changed to the new value

$$\sigma^{SBT} = 73\,\text{ps}. \tag{A.18}$$

List of Figures

List of Tables

Bibliography

[1] S. Goriely. The fundamental role of fission during r-process nucleosynthesis in neutron star mergers. *Eur. Phys.*, A(51):22, 2015.

[2] T. Murakami. Pion productions in mass asymmetric ^{28}Si+In reactions at 400, 600, 800 MeV/nucleon. `http://studylib.net/doc/9575691/why-p`. Accessed: 2017-09-29.

[3] S. Shibagaki, T. Kajino, G. J. Mathews, S. Chiba, S. Nishimura, and G. Lorusso. Relative contributions of the weak, main and fission recycling r-process. *The Astophysical Journal*, 816(2), 2015.

[4] J. Bliss, A. Arcones, F. Montes, and J. Pereira. Impact of (α, n) reactions on weak r-process in neutrino-driven winds. *J. Phys. G: Nucl. Part. Phys.*, (44):054003, 2017.

[5] H.-T. Janka. Explosion Mechanisms of Core-Collapse Supernovae. *arXiv:1206.2503*, 2012.

[6] P. Möller, A. J. Sierk, T. Ichikawa, A. Iwamoto, R. Bengtsson, H. Uhrenholt, and S. Aberg. Heavy-element fission barriers. *PHYSICAL REVIEW C*, 79(064304), 2009.

[7] O. Hahn and F. Strassman. Über den Nachweis und das Verhalten der bei der Bestrahlung des Urans mittels Neutronen entstehenden Erdalkalimetalle. *Die Naturwissenschaften*, 27:11–15, 1939.

[8] L. Meitner and O. Frisch. Disintegration of Uranium by Neutrons: a New Type of Nuclear Reaction. *Nature*, 1(143):239–240, 1939.

[9] J. E. Lynn. Fission Theory: Its Relevance to the Nuclear Cross Section Data Base. *American Nuclear Society Meeting*, 1989.

[10] W. J. Swiatecki. *Phys. Rev.*, (100):937, 1955.

[11] V. M. Strutinsky. *Nucl. Phys.*, A(95):420, 1967.

[12] V. M. Strutinsky. *Nucl. Phys.*, A(122):1, 1968.

[13] P. Möller and J. R. Nix. *Proceedings of the Third IAEA Symposium on the Physics and Chemistry of Fission*, Vol. I:103, 1974.

[14] H. Specht. Nuclear fission. *Review of Modern Physics*, 46(4), 1974.

[15] B. B. Back, J.P. Bondorf, G. A. Otroschenko, J. Pedersen, and B. Rasmussen. Fission of U, Np, Pu and Am isotopes excited in the (d, p) reaction. *Nuclear Physics A*, 165:449–474, 1971.

[16] P. Möller, J. R. Nix, W. D. Myers, and W. J. Swiatecki. *At. Data Nucl. Data Tables*, (59):185, 1995.

[17] A. N. Andreyev, J. Elseviers, M. Huyse, P. Van Duppen, S. Antalic, A. Barzakh, N. Bree, T. E. Cocolios, V. F. Comas, J. Diriken, D. Fedorov, V. Fedosseev, S. Franchoo, J. A. Heredia, O. Ivanov, U. Köster, B. A. Marsh, K. Nishio, R. D. Page, N. Patronis, M. Seliverstov, I. Tsekhanovich, P. Van den Bergh, J. Van De Walle, M. Venhart, S. Vermote, M. Veselsky, C. Wagemans, T. Ichikawa, A. Iwamoto, P. Möller, and A. J. Sierk. New Type of Asymmetric Fission in Proton-Rich Nuclei. *Phys. Rev. Lett.*, (105):252502, 2010.

[18] T. Ichikawa, A. Iwamoto, P. Möller, and A. J. Sierk. Contrasting fission potential-energy structure of actinides and mercury isotopes. *Phys. Rev.*, C(86):024610, 2012.

[19] E. M. Burbidge, G. R. Burbidge, W. A. Fowler, and F. Hoyle. Synthesis of the Elements in Stars. *Reviews of Modern Physics*, 29(4):547–650, 1957.

[20] P. Möller and J. Randrup. Calculated fission-fragment yield systematics in the region $74 \leq Z \leq 94$ and $90 \leq N \leq 150$. *PHYSICAL REVIEW C*, 91(044316), 2015.

[21] A.M. Moro. Three-body model for the analysis of quasifree scattering reactions in inverse kinematics. *Phys. Rev. C*, 92(044605), 2015.

[22] C. Scheidenberger and M. Pfützner. *The Euroschool on Exotic Beams*. Number Bd. 4 in Lecture Notes in Physics. Springer Berlin Heidelberg, 2014.

[23] V. Panin, J. T. Taylor, S. Paschalis, F. Wamers, et al. Exclusive measurements of quasi-free proton scattering reactions in inverse and complete kinematics. *Physics Letters B*, 753:204–210, 2016.

[24] L. V. Chulkov, F. Aksouh, A. Bleile, O. V. Bochkarev, D. Cortina-Gil, et al. Quasi-free scattering with ^{6,8}He beams. *Nuclear Physics*, A(759(1-2)):43–63, 2005.

[25] R. C. Johnson and P. J. R. Soper. Contribution of Deuteron Breakup Channels to Deuteron Stripping and Elastic Scattering. *Phys. Rev. C*, 1:976–990, Mar 1970.

[26] V. Panin. Fully exclusive measurements of quasi-free single-nucleon knockout reactions in inverse kinematics. *PhD Thesis, Technische Universität Darmstadt*, 2012.

[27] C. Bertulani. Private communicaton. 2018.

[28] L. Atar, S. Paschalis, and al. et. Quasifree (p, $2p$) Reactions on Oxygen Isotopes: Observation of Isospin Independence of the Reduced Single-Particle Strength. *Phys. Rev. Lett.*, 120:052501, Jan 2018.

[29] K. Ozeki. Study of proton-hole states in carbon isotopes via proton knockout reactions. *PhD Thesis*, 2007.

[30] Xiangdong Ji. A Modern Introduction to Nuclear Physics: Bulk Properties and Nuclear Matter. `https://www.physics.umd.edu/courses/Phys741/xji/chapter7.pdf`. Accessed: 2018-03-29.

[31] Kai Hencken, George Bertsch, and Henning Esbensen. Breakup reactions of the halo nuclei ^{11}Be and ^{8}B. *Phys. Rev. C*, 54:3043–3050, Dec 1996.

[32] T. Aumann, C. A. Bertulani, and J. Ryckebusch. Quasifree $(p, 2p)$ and (p, pn) reactions with unstable nuclei. *Physical Review C*, 88(064610), 2013.

[33] C. Barbieri. Role of Long-Range Correlations in the Quenching of Spectroscopic Factors. *Phys. Rev. Lett.*, 103:202502, Nov 2009.

[34] Takaharu Otsuka, Rintaro Fujimoto, Yutaka Utsuno, B. Alex Brown, Michio Honma, and Takahiro Mizusaki. Magic Numbers in Exotic Nuclei and Spin-Isospin Properties of the *NN* Interaction. *Phys. Rev. Lett.*, 87:082502, Aug 2001.

[35] J. P. Schiffer, S. J. Freeman, J. A. Caggiano, C. Deibel, A. Heinz, C.-L. Jiang, R. Lewis, A. Parikh, P. D. Parker, K. E. Rehm, S. Sinha, and J. S. Thomas. Is the nuclear spin-orbit interaction changing with neutron excess? *Phys. Rev. Lett.*, 92:162501, Apr 2004.

[36] P. G. Hansen and J. A. Tostevin. DIRECT REACTIONS WITH EXOTIC NUCLEI. *Annual Review of Nuclear and Particle Science*, 53:219–261, 2003.

[37] G. Jacob and Th. A. J. Maris. *Rev. Mod. Phys.*, 38(121), 1966.

[38] B. Van Overmeire, W. Cosyn, P. Lava, and J. Ryckebusch. Relativistic eikonal description of $a(p, pN)$ reactions. *Phys. Rev. C*, 73:064603, Jun 2006.

[39] D. Mücher, M. Sasano, M. Sako, et al. Fission Barrier Studies of Neutron-Rich Nuclei via the $(p, 2p)$ Reaction. *Proposal RIBF NP-PAC-12*, 2013.

[40] K.H. Schmidt, S. Steinhäuser, C. Böckstiegel, A. Grewe, A. Heinz, A.R. Junghans, J. Benlliure, H.G. Clerc, M. de Jong, J. Müller, M. Pfützner, and B. Voss. Relativistic radioactive beams: A new access to nuclear-fission studies. *Nuclear Physics A*, 665(3):221 – 267, 2000.

[41] N. Chiga. Private communicaton. 2018.

[42] K. Jakobs. Course: Particle Detectors WS 2015/16. `http://portal.uni-freiburg.de/jakobs/dateien/vorlesungsdateien/particledetectors/kap_06a.pdf`. Accessed: 2017-11-15.

[43] Hamamatsu Photonics K.K. FAQ: Si strip detector. `https://www.hamamatsu.com/eu/en/support/faq/products_faq/si_photodiode/si_strip_detector.html`. Accessed: 2017-11-15.

[44] M.J. French, L.L. Jones, Q. Morrissey, A. Neviani, R. Turchetta, J. Fulcher, G. Hall, E. Noah, M. Raymond, G. Cervelli, P. Moreira, and G. Marseguerra. Design and results from the APV25, a deep sub-micron CMOS front-end chip for the CMS tracker. *Nuclear Instruments and Methods in Physics Research*, A(466):359–365, 2001.

[45] H. Spieler. Signal Processing and Electronics. `http://www-physics.lbl.gov/~spieler/Valencia_2013/ENTERVISION_Signal_Processing_and_Electronics.pdf`. Accessed: 2018-03-20.

[46] L. Werner. *A silicon tracker system for (p,2p) reactions*. Master Thesis, Technische Universität München, James-Franck-Str.1, 85748 Garching/Germany, 2016.

[47] L. Jones. APV25-S1 User GuideVersion 2.2. 2001.

[48] Coefficient of thermal expansion of AlN. `http://accuratus.com/alumni.html`. Accessed: 2017-02-26.

[49] M. Böhmer. Private communicaton. 2018.

[50] Chong Wu, Yuekun Heng, Yuda Zhao, Xiaojian Zhao, Zhijia Sun, Jinjie Wu, Zhenghua An, Li Zhao, Linli Jiang, Fengmei Wang, Shengtian Xue, and Yifang Wang. The timing properties of a plastic time-of-flight scintillator from a beam test. *Nuclear Instruments and Methods in Physics Research Section A: Accelerators, Spectrometers, Detectors and Associated Equipment*, 555(1):142 – 147, 2005.

[51] H. Baba, T. Ichihara, T. Ohnishi, S. Takeuchi, K. Yoshida, Y. Watanabe, S. Ota, and S. Shimoura. *RIKEN Accel. Prog. Rep.*, 47:235, 2014.

[52] T. Kobayashi. Private communicaton, BDC memo-1. 2016.

[53] O. B Tarasov and D. Bazin. LISE++: Radioactive beam production with in-flight separators. *Nuclear Instruments and Methods in Physics Research*, B:4657–4664, 2008.

[54] Y. Kubota. Neutron-neutron correlation in Borromean ^{11}Li via the $(p, 2p)$ reaction. *PhD Thesis, CNS Tokyo University*, 2016.

[55] H. Baba et al. *Nucl. Inst. Meth. A*, 616:65, 2010.

[56] H. Baba, T. Ichihara, T. Isobe, C. Houarner, C. Maugeais, B. Raine, F. Saillant, G. Wittwer, N. Kurz, H. Schaffner, R. Gernhäuser, S. Anvar, D. Calvet, F. Chateau, and E. Pollacco. DAQ coupling in RIKEN RIBF. In *2014 19th IEEE-NPSS Real Time Conference*, pages 1–5, May 2014.

[57] J. Michel, J. Adamczewski-Musch, M. Böhmer, G. Korcyl, M. Palka, S. Yurevich, and M. Traxler. *A Users Guide to the HADES DAQ System*. 2014-05-15.

[58] G. Korcyl, L. Maier, J. Michel, A. Neiser, M. Palka, M. Penschuck, P. Strzempek, M. Traxler, and C. Ugur. *A Users Guide to the TRB3 and FPGA-TDC Based Platforms*. 2015-10-29.

[59] H. Baba. LUPO Multi TimeStamp Module Ver. 2.0. `https://ribf.riken.jp/RIBFDAQ/index.php?plugin=attach&refer=DAQ%2FDownload&openfile=lupo_multitimestamp_rev2.0e.pdf`. Accessed: 2018-04-25.

[60] HIMAC Accelerator properties. `http://www.aec.go.jp/jicst/NC/senmon/kasoku/siryo/kasoku01/s2s3.htm`. Accessed: 2017-02-20.

[61] NIRS, Department of Accelerator and Medical Physics. `http://www.nirs.go.jp/ENG/core/ace/index.html`. Accessed: 2016-06-09.

[62] K. Kobayashi et al. De-excitation gamma-rays from the s-hole state in ^{15}N associated with proton decay in ^{16}O. 2006.

[63] A. Cipollone, C. Barbieri, and P.l Navrati. Chiral three-nucleon forces and the evolution of correlations along the oxygen isotopic chain. *arXiv:1412.0491v2 [nucl-th]*, 2015.

[64] F. Ajzenberg-Selove. Energy levels of light nuclei A=13-15. *Nuclear Physics*, A(523):1–196, 1991.

[65] L. Atar. Investigation of the Single-Particle Structure of Oxygen Isotopes in Quasi-free knockout reactions at the R3B/LAND Setup. *PhD Thesis, Technische Universität Darmstadt*, 2015.

[66] V-STARS Geodetic Systems, Inc. `http://www.geodetic.com/products/systems/v-stars-s.aspx`. Accessed: 2017-03-12.

[67] Manufacturing tolerances of PCBs. `https://www.multi-circuit-boards.eu/leiterplatten-qualitaet/fertigungstoleranzen.html`. Accessed: 2017-03-09.

[68] R. Brun and F. Rademaker. ROOT - An Object Oriented Data Analysis Framework. *Nucl. Inst. and Meth. in Phys. Res. A*, 389:81–86, 1997.

[69] ROOT - An Object Oriented Data Analysis Framework. `http://root.cern.ch/`. Accessed: 2018-04-19.

[70] Description of the Ortec 462 time calibrator. `http://www.ortec-online.com/products/electronics/time-to-amplitude-converters-tac/462`. Accessed: 2018-01-25.

[71] O. Lepyoshkina. Coulomb Excitation of Proton Rich Nuclei ^{32}Ar and ^{34}Ar. *PhD Thesis, Technische Universität München*, 2013.

[72] Turchetta and Renato. *LaTeX Analog Electronics for Radiation Detection.* CRC Press Taylor & Francis Group, 6000 Broken Sound Parkway NW, Suite 300, 1. edition edition, 2016.

[73] S. Koyama, H. Otsu, and for SAMURAI08 collaboration. Detailed analysis of tracking detectors for SAMURAI08 experiment. *RIKEN Accel. Prog. Rep.*, 48:46, 2015.

[74] T. Kobayashi. Private communicaton, BDC memo-3. 2016.

[75] Description of the CAMAC discriminator Phillips 7106. `http://www.phillipsscientific.com/pdf/7106ds.pdf`. Accessed: 2018-01-23.

[76] S. Nishimura, M. Kurata-Nishimura, K. Morimoto, Y. Nishi, A. Ozawa, T. Yamaguchi, T. Ohnishi, T. Zheng, M. Chiba, and I. Tanihata. Systematic studies of scintillation detector with timing resolution of 10 ps for heavy ion beam. *Nuclear Instruments and Methods in Physics Research Section A: Accelerators, Spectrometers, Detectors and Associated Equipment*, 510(3):377 – 388, 2003.

[77] G. F. Knoll. *Radiation Detection and Measurement.* John Wiley and Sons, Inc, New York, 3. edition edition, 2000.

[78] J. B. Birks. *The Theory and Practice of Scintillation Counting*. Pergamon Press, Oxford, 1964.

[79] S. Agostinelli, J. Allison, K. Amako, J. Apostolakis, H. Araujo, et al. Geant4âa simulation toolkit. *Nuclear Instruments and Methods in Physics Research Section A: Accelerators, Spectrometers, Detectors and Associated Equipment*, 506(3):250 – 303, 2003.

[80] J. Allison, K. Amako, J. Apostolakis, H. Araujo, et al. Geant4 developments and applications. *IEEE Transactions on Nuclear Science*, 53(1):270–278, Feb 2006.

[81] J. Allison, K. Amako, J. Apostolakis, P. Arce, M. Asai, et al. Recent developments in Geant4. *Nuclear Instruments and Methods in Physics Research Section A: Accelerators, Spectrometers, Detectors and Associated Equipment*, 835(Supplement C):186 – 225, 2016.

[82] M. Leuschner, J. R. Calarco, F. W. Hersman, E. Jans, G. J. Kramer, L. Lapikás, G. van der Steenhoven, P. K. A. de Witt Huberts, H. P. Blok, N. Kalantar-Nayestanaki, and J. Friedrich. Quasielastic proton knockout from ^{16}O. *Phys. Rev. C*, 49:955–967, Feb 1994.

[83] S. Kox, A. Gamp, C. Perrin, J. Arvieux, R. Bertholet, J. F. Bruandet, M. Buenerd, R. Cherkaoui, A. J. Cole, Y. El-Masri, N. Longequeue, J. Menet, F. Merchez, and J. B. Viano. Trends of total reaction cross sections for heavy ion collisions in the intermediate energy range. *Phys. Rev. C*, 35:1678–1691, May 1987.

[84] K. Ogata, K. Yoshida, and K. Minomo. Asymmetry of the parallel momentum distribution of (p, pn) reaction residues. *Phys. Rev. C*, 92:034616, Sep 2015.

[85] N.S. Chant and P.G. Roos. *Phys. Rev. C*, 15(57):1977.

[86] L. Lapikas. Quasi-elastic electron scattering off nuclei. *Nuclear Physics A*, 553:297 – 308, 1993.

[87] E.B. Podgorsak. *Radiation Oncology Physics: A Handbook for Teachers and Students*. International Atomic Energy Agency, Wagramer Strasse 5, A-1400 Vienna, 2005.

[88] S. Saro et al. *Nucl. Instrum. Meth.*, A(381):520, 1996.

[89] Relating Delta Ray Energy to Beam Energy. `https://www.triumf.info/wiki/pwalden/images/4/45/Delta_ray.pdf`. Accessed: 2018-02-16.

[90] EStar: Stopping-power and range table for electrons. https://physics.nist.gov/PhysRefData/Star/Text/ESTAR.html. Accessed: 2018-03-18.

[91] S. Paschalis, S. Shimoura, et al. Investigation of the $4n$ system at SAMURAI by measuring $p, p\alpha$ quasi- free scattering at large momentum transfer in complete kinematics. *NP-PAC-12*, 2013.

[92] APV HIP Dead Time, Response to issues raised during the HFT CD-1 review on Nov. 12, 2009. http://www4.rcf.bnl.gov/~nieuwhzs/CD-1_Response_APV_HIP_15Dec2009.pdf. Accessed: 2017-11-19.

Acknowledgment

At the end of my PhD thesis I'd like to thank all the persons who supported me during the course.

First of all I want to thank Prof. Dr. Walter Henning who overtook my doctor father despite the large distance between Munich, Argonne and Japan. It was a great pleasure to discuss with him and I am thankful for his support. Since he unfortunately could not finish my supervision, I also would like to thank Prof. Dr. Shawn Bishop for his uncomplicated willingness to overtake this task.

A special thank is contributed to my supervisors Roman Gernhäuser and Masaki Sasano. Without them, the experiment would not have been carried out in that smooth way. I appreciated the deep and fruitful discussions during the whole course. Their endless support and patience relating any problems was really admirable.

The preparation, construction and execution of the experiment was never a one-man show but needed a courageous team. I'd like to thank my Japanese colleague Masami Sako for his persistent work with me! Furthermore, huge contribution was provided by Michael Böhmer and Ludwig Maier who commissioned the data-acquisition. Further thanks are due to Sonja Winkler, Ralf Lang and Noboyuki Chiga for their work on the detectors and target chamber construction. Also I'd like to say thank you to my former supervisor Dennis Mücher who left to Guelph/Canada at the begin of my course. Especially his financial support for this project was the initial starting point. Great support during the experiment was provided by the team in the HIMAC experiment of M. Böhmer, R. Gernhäuser, T. Kobayashi, D. Mücher, V. Panin, M. Sako, M. Sasano, L. Stuhl and L. Werner.

I'd also like to thank my colleagues in my office room who always helped me whenever I asked. Especially the generous dedication of Christian Berner and Lukas Werner were a great help.